3D PRINTED FLUIDIC DEVICES FOR BIOMEDICAL APPLICATIONS

By

Nathan Abraham Redman

A DISSERTATION

Submitted to
Michigan State University
in partial fulfillment of the requirements
for the degree of

Biomedical Engineering—Doctor of Philosophy

2022

ABSTRACT

Antimicrobial resistance represents an imminent and growing threat to global health. It is estimated that antimicrobial resistance will cause 10 million deaths a year by 2050. The testing of clinical infections for susceptibility to antimicrobial drugs is therefore critical. However, current methods of susceptibility testing are prohibitively slow, and they require pathogen isolation and culture. This inability to rapidly screen infections causes serious problems including patient mortality by sepsis, over-prescription of broad-spectrum antibiotics, and the accelerated spread of antimicrobial resistance in human pathogens. Faster susceptibility testing is required to more effectively treat sepsis and prevent the unnecessary selection for resistant pathogenic strains more effectively. Quantifying drug susceptibility at the single-cell level on a multiphase chip platform will eliminate the need for culture and enable drug susceptibility screening within minutes. Antibiotics often alter extracellular levels of adenosine triphosphate (ATP) in susceptible microbial cells, while leaving resistant cells mostly unaffected. An individual microbial cell will contain ~1-5 attomoles of ATP, which is only detectable if confined to extremely small reaction volumes. Here we propose a multiphase (immiscible aqueous and ether) microfluidics platform combined with a microcapillary system (Chapters 2,3). This system will confine individual pathogens and challenge drugs inside droplets of nanoliter-scale volume to enable detection of drug-induced alteration of ATP release from susceptible cells. This system will enable more informed and specific prescription of drugs to both improve patient outcomes and relieve unnecessary selective pressure for the spread of antimicrobial resistance.

The same 3D printing tools that apply well to multiphase fluidic devices are also leveraged to address biomedical challenges in tangent fields. Progress in the fields of organoid modeling and regenerative tissue printing are discussed (Chapter 4).

ACKNOWLEDGEMENTS

I would like to thank my advisor, Dr. Dana Spence, for his endless encouragement and support. I would also like to thank my family, who gave me the strength and the purpose to complete this program. I am grateful for you all.

-Nathan

TABLE OF CONTENTS

LIST OF ABBREVIATIONS

3D	3 Dimensional
PDMS	Polydimethylsiloxane
LB	Luria Broth
FDM	Fused Deposition Model
LB	Luria Broth
PCR	Polymerase Chain Reaction
ATP	Adenosine Triphosphate
L/L	Luciferin/ Luciferase mixture
HUVEC	Human Umbilical Vein Endothelial Cells
GFP	Green Fluorescent Protein
PBP	Penicillin-Binding Protein
PMT	Photomultiplier Tube
DAQ	Data Acquisition
FITC	Fluorescein Isothiocyanate
CAD	Computer Aided Design
STL	Standard Tessellation Language
FPS	Frames per Second
GelMa	Gelatin Methacrylate
LAP	Photoinitiator (Lithium phenyl-2,4,6-trimethylbenzoylphosphinate

CHAPTER 1: INTRODUCTION

1.1 Microfluidics

1.1.1 Principles and Current Methods

Microfluidics deals with manipulation of fluid samples through channels on the order of microns (10^{-6} meters) and the technologies which produce channels with desired properties. Channels with various sizes, shapes, orientations, and supporting components may be combined to manipulate fluids in complex ways. Fluid samples can be mixed, separated, temperature cycled, and even precisely exposed to magnetic fields. These devised systems operate on capillaries or chips.

The technologies which lead to microfluidics were born out of a need to miniaturize silicon components for integrated circuits in the 1950s. By 1980, Terry et.al. had developed a functional gas chromatographic column by 'micromachining' features onto a silicon wafer, in the first development of a 'lab-on-chip'[1]. From these innovative origins, a field of miniaturized devices was born along with several revolutions in manufacturing techniques[2]. Manz et.al. further advanced the field by micromachining glass components which combined chromatographic and detection functions onto the same device, referred to as a 'μ-TAS' system[2]. Photolithography, or the use of light and photomasks to pattern channel and chip designs, emerged as the major technology in microfluidic device manufacture[3].

The chips up to this point had largely been manufactured from silicon and glass substrates. Unfortunately, purified silicon was relatively expensive. Additionally, these chips were opaque and unable to couple with optical microscopy. Finally, it is difficult to fabricate chips out of these materials. In a bid to address these issues, researchers turned to a silicone-based polymer known as polydimethylsiloxane or 'PDMS'.

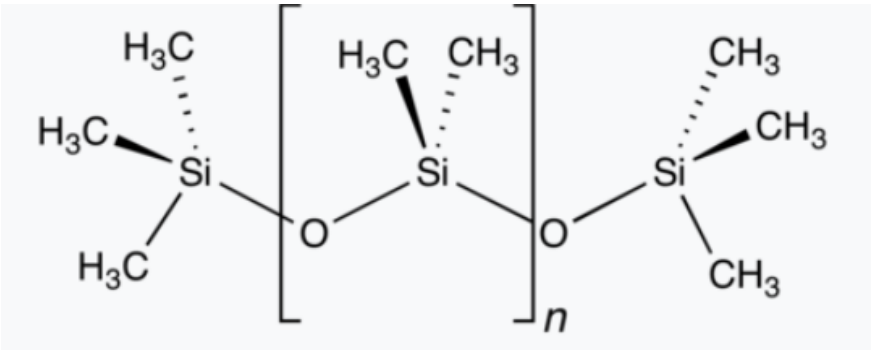

Figure 1. A The Chemical Structure of polydimethylsiloxane. The flexible, transparent, naturally hydrophobic polymer can be quickly synthesized by mixing a monomer solution and a polymerizing agent (often labeled components 'A' and 'B' respectively). The polymer is cheap, clear, and oxygen-permeable[4].

Currently, many methods are in use for device fabrication. Semiconductor methods including photolithography and 'hot embossing' are still used for certain applications. Micromachining is still used for glass chips, and a subfield of paper microfluidics has emerged, focusing on cheap and disposable single-use paper analytical devices driven by capillary action[5].

PDMS has dominated modern microfluidics because of its favorable mechanical properties and ability to make new chips from the same cast. Briefly, a photomask is manufactured specifically for the geometry desired for a given chip. The photomask is then used for photolithography to etch the desired pattern into a silicon wafer. The silicon wafer is then used as a cast over which to pour PDMS, which in turn cures in the appropriate shape. The PDMS must then be fused to a glass slide in a process known as plasma bonding. This process utilizes specialized equipment, and the manufacturing process takes place entirely within a clean room to avoid dust contamination[6].

1.1.2 Advantages for Biomedical Applications

Since their formalized application to biomedical problems starting in the 1990s, microfluidic devices have revolutionized the field of analytical chemistry because of their intrinsic advantages for analyzing biological samples. Their small channel sizes enable analysis

of extremely small volumes of liquid samples and detection of nanogram, or even picogram amounts of dissolved analytes. This is especially pertinent when a given sample is very expensive, is in short supply or is otherwise difficult to procure or replace. Mixing in microfluidic devices can be controlled to with extreme temporal accuracy and down to nanoliter or even femtoliter precision[7]. This makes enzymatic and other biological assays more controllable and reproducible. Low volumes also enable efficient, diffusion-based mixing and rapid temperature cycling (Miracles et al., 2013). Low volumes also enable the high-throughput experiments, and the same volume may be used to run multiple experimental conditions in parallel. Finally, the subfield of droplet microfluidics have provided a platform for single-cell analysis and traceable sample 'barcoding'[9]. Cell-based samples can be supplied to droplet generating platforms and signal can be detected droplet-wise to achieve single-cell resolution data. Such versatility makes microfluidics an asset when reducing reagent cost or equipment requirement is of interest to bioanalytical work.

While fluidic systems (dealing with milliliters or larger volumes) may suffer from chaotic turbulent flow, droplet microfluidics may take advantage of laminar flow to deliver precise and reproducible volumes of liquid. This makes direct comparisons between biological samples much easier and more efficient[10].

PDMS in particular has several advantages for biological applications, which make it a popular platform for molecular biologists and bioanalytical chemists. Primarily, PDMS is biocompatible with cells[11]. Cells can be grown on PDMS with minimal toxicity. This has endless applications. Growing cells on PDM substrate enables physical testing such as stretch and shear flow responses. Alternatively, combining PDMS fluidic devices and cultured human cells is also used as a platform for 'human-on-chip' designs, which try to create idealized systems modeling

in vivo tissue/fluid interactions[12]. The silicon polymer is also oxygen-permeable, avoiding potential issues involving killing compartmentalized cells from hypoxia. PDMS is also transparent and therefore compatible with on-chip analysis by optical microscopy.

1.1.3 Droplet Microfluidics

Dealing with liquid dilutions or suspensions makes unit-resolution analysis of cell or particle solutions difficult. To address this, a subfield of droplet-microfluidics was developed which utilizes immiscible liquid to partition solutions into discrete droplets for individual analysis. Most systems leverage Poissonian statistics to ensure that droplets do not contain multiple particles or cells to any significant extent. A discretized droplet approach can enable hi-throughput experiments covering a wide range of iterations. For example, Droplet Digital PCR leverages droplet microfluidics to enable single-cell analysis and isolation/detection of rare allele nucleic acids, which would be impossible in a continuous fluid-phase sample. The most common modern application of droplet microfluidics is flow cytometry, which breaks down cell solution into a stream of drops containing 1 cell at most. The droplets are then scanned with lasers and evaluated for the presence of cells and certain fluorophore markers. Droplets are imparted charge based on their fluorophore signals and separated into distinct populations. Droplet microfluidics is a rapidly developing field which allows a great deal of flexibility to tailor parameters as needed. Droplet volumes from the microliter to femtoliter range may be produced. Droplets can be produced at rates of hundreds to thousands of Hz, and then controlled with precision sufficient to split or recombine droplets of interest as they traverse the channel.

The principle behind droplet generating systems are simple: Two immiscible liquids are selected, typically an aqueous phase and a nonpolar phase. Often this nonpolar phase is a polyfluorinated ether. The aqueous phase is almost invariably a solution of the cells or

biomolecules of interest, and the nonpolar phase is used as a carrier phase to create an emulsion and push droplets through the channels. In addition to these two liquids a surfactant (typically a detergent) is used to stabilize the surface energy of newly formed droplets; This prevents the droplets from breaking up, coalescing together, or adhering to channel walls once formed. Droplets are commonly generated in 3 geometries: (1) Coaxial 'Coflow', (2) Flow Focus, or (3) T-junction (Fig. 2) designs. All these chips use some combination of drag, shear force, and surface tension to break up the continuous aqueous phase into comparatively small, uniform droplets. Depending on the chip and the desired experimental parameters, the droplet volumes can range from hundreds of nanoliters to a few femtoliters.

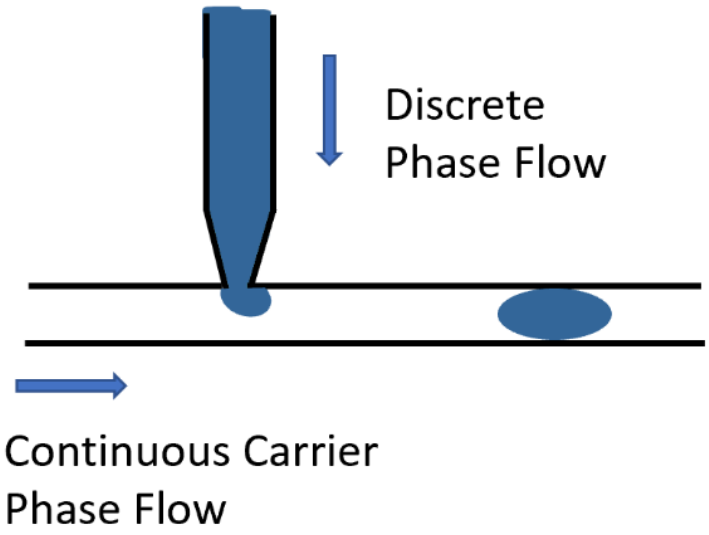

Figure 2. A T-junction droplet generator. Droplet-generating chips follow different geometries. A common feature is the use of two immiscible liquids to generate an emulsion. The inert carrier liquid is referred to as the continuous phase and the sample-containing phase to be segmented into droplets is known as the discrete phase. Stabilizing agents such as soaps, detergents, or surfactants, are commonly used to improve droplet behavior.

Despite the many advantages of droplet microfluidics, several challenges need to be addressed when developing a new droplet device, including tunability, volume, monodispersity, and stability. Droplets that are not stable can break up, coalesce, or adhere to channel surfaces,

leading to unpredictability, loss or monodispersity/ signal or loss of sample. It is therefore critical that both the carrier phase and the channel surfaces contribute to the stability. A proper surfactant must be chosen and validated. Finally, the surfaces of the channels may need to be treated to minimize their affinity for the aqueous phase.

For precision and comparison purposes, it is required that the volume profile be highly monodisperse, meaning that all droplets are equivalent in volume. This enables quantitative comparison between them.

1.1.4 Potential use of Additive Manufacturing to Improve Microfluidic Field

Most chips designed for microfluidics are produced using polydimethylsiloxane (PDMS). PDMS is a polymer that can be generated from liquid components, the subunits and a cross-inking agent. This is advantageous because the liquid components may be mixed, then cast into any desired geometry before it polymerizes into a solid. This enable chips to be designed to any desired specifications. Additionally, PDMS is naturally hydrophobic, which facilitates the stable formation of aqueous droplets within the channels. The hydrophobic PDMS prevents the droplets from ‘wetting’ the channel or adhering to the channel walls. Unfortunately, there are drawbacks to this modality. The photomasks used in producing the silicon casts are expensive and purchased from companies with highly specialized equipment. Similarly, the photolithography equipment used to etch the wafers and the devices used to plasma-bond the PDMS designs to their glass substrates require expensive equipment and a carefully controlled cleanroom environment. PDMS chips are extremely sensitive to inclusion errors from debris and may need to be manufactured multiple times to achieve their theoretical behavior. All these steps are labor intensive. In all, from concept to production of a working prototype may take days or weeks and my cost thousands of dollars. In addition, the masks for photolithography are specific to one

prototype. Any modifications or new designs would require the expensive and lengthy process to be repeated. There is an opportunity for improvement if a droplet generating chip with similar performance to a traditional PDMS chip may be produced more efficiently using a different technology.

The fabrication of PDMS chips are slow, labor intensive, costly, and inflexible to change. An improved manufacturing process would be rapid, cheap, and allow for efficient prototyping. A desirable fabrication schema would allow for a ‘fail fast and often’ approach to chip prototyping. These features directly align with the strengths of additive manufacturing, specifically 3d printing. 3D printing allows rapid design of desired structures on a Computer Aided Design (CAD) software. Additionally, 3D printing allows for cheaper manufacture out of a flexible selection of resins and enables simultaneous printing of several chips, limited only by the size of the print stage. The production requires to cleanroom as most commercial printers operate in a sealed compartment and boast resolution of a few microns. Lastly, because the structures are determined digitally instead of a photomask, changes can be made quickly by updated the CAD file rather than building a new photomask. For these reasons, 3D printing are a strong candidate for the fabrication of a droplet-generating chip.

1.2 Additive Manufacturing and PolyJet Printing

1.2.1 Principles and Current Methods

Traditional manufacturing methods such as milling are referred to as ‘subtractive manufacturing’, where the final product is produced by removing material from a pre-existing structure. Additive manufacturing, in contract, is the process of building up more complex structures from the ground up. 3D printing is the most applied additive manufacturing process. In 3D printing, objects are built by laying down successive layers of constructive material, one on

top of the other.

The shape is determined by a set of digital coordinates saved in a CAD file. The most common form of CAD file is the standard tessellation language or .stl file. STL files are created and modified in a CAD software. Typical CAD software used in academia and industry includes Autodesk and SolidWorks. Parts and Assemblies can be saved in STL format and loaded into a printer manager software for part fabrication.

There are several different 3D methods developed since the field was conceived. Hideo Kodama arguably invented modern 3D printing when he designed a layer-by-layer printer which used a photocurable resin. From there, several printing methods have matured including fused deposition modeling (FDM), Stereolithography (SLA), Selective Layer Sintering (SLS), Digital Light Processing (DLP), PolyJet printing, and Bioprinting. Each has its strengths and weaknesses, and the platform should be selected for its suitability for each individual application.

Stereolithography, also called ‘vat polymerization’, utilizes scanning UV lasers to cure a photopolymer in a liquid polymer bath. As the part is solidified, it is drawn out of the vat until every layer is complete. Time to print completion, depending on the size and complexity of the part, is on the order of hours or days. Parts are made from acrylates and are strong enough to be further machined. It is a relatively expensive modality, and parts typically cost hundreds or thousands of dollars. Additionally, dealing with such large quantities of uncured resin provides safety challenges including spills, splashes, and vapor inhalation.

Fused Deposition Modeling relies on solid plastic filaments instead of curable resins. Filaments are fed into heated printer heads, which melt then filament and extrude it onto the stage. Typical resins include polylactic acid (PLA) and polyethylene terephthalate (PET). FDM printers and consumables have the advantage of being very cheap, they lack the resolution of

PLA or resin-based printers. Nominal resolution is about 0.4mm for some models. FMD is well suited for parts where high resolution is not required or where cost concerns outweigh other considerations.

Selective Layer Sintering involves the use lasers to fuse together ceramic or metal powders into a solid piece. This technique is capable of fabricating metal and ceramic parts and has found applications in automotive and aeronautics industry. However, SLS suffers from poor resolution (roughly .7mm) and porous, rough surfaces on completed parts which require further refining steps.

PolyJet printing makes use of inkjet-style heads which deposit droplets of photocurable resin on the print stage while concurrently curing each layer with UV. The resolution of such printers can nominally reach as low as 27μm. Unlike the previously mentioned methods, this method can seamlessly incorporate different materials from different heads into the same part. Various materials are compatible printers, involving harder plastics like acetonitrile butadiene (ABS) or softer rubber-like materials. However, due to the specialized nature of the cartridges, the materials must be offered by the vendor. This lacks the flexibility of platforms like the FDM, where custom filaments can be made for ad hoc projects.

A very specialized field of 3D printing emerged. Organ-on-chip substrates may be printed to support cells and fluidics. Tissue printing, or ‘bioprinting’, prints soft, cell-laden hydrogels to build up structures that resemble natural tissue or entire organs. The purpose of these structures is to replace damaged and lost tissue or perform physiological functions. Common gels include Gelatin Methacrylate (Gel-Ma) and collagen. Bioprinting has been developed to mimic many tissues in the body, from liver lobules to self-assembling capillaries. Tissue produced in this way has been applied to health solutions ranging from bladder transplants to printing human skin for

burn victims.

These various methods of 3D printing apply most effectively to different areas of specialty, and care must be taken to employ the optimal platform for the project at hand.

1.2.2 Suitability of Different Methods to Microfluidics

Channels in microfluidics are, by definition, on the sub-millimeter scale. To successfully utilize 3D printers to correct some of the deficits of traditional microfluidic chip manufacturing, the printers must be able to print channels correctly at this scale. While micron-level resolution is not an issue for micromachining or photolithography, it presses the resolution limits of what is currently available to 3D printer. Additionally, the printer must be able to satisfy all the same properties that make PDMS amenable to microfluidics. Specifically, the printer must allow reproducible, optically clear chips that will not adhere to the droplets.

Additive manufacturing has revolutionized device fabrication in the 21st century. Most traditional manufacturing methods, such as injection-molding or dye-casting, require the manufacture of custom, ad-hoc parts and often require single-use negatives which are then discarded. Additive manufacturing, specifically 3D printing, is unique in that it requires no prefabricated cast or dye and can rapidly prototype new designs using only software.

Fused-Deposition Modeling enables cheap, rapidly produced prototypes. However, due to the nature of the filament feeding into the part, it is not possible to incorporate multiple resins into the same part. Additionally, the typical FDM platform, such as the LulzBot Taz-6® reaches resolution of 500mm. This poor resolution and material inflexibility renders FDM a poor choice for development of microfluidic devices on an FDM platform.

Selective Layer Sintering is inadequate for similar reasons. The poor resolution and difficult incorporating multiple materials make SLS unsuitable for chip manufacture. SLS has an

additional pitfall: the surfaces of structures made in SLS are porous and rough, requiring additional finishing work. This limitation makes it incompatible with making chips with precision micron-level features.

PolyJet printing is an excellent candidate for microfluidic device manufacture. It supports high optically clear resins, enables incorporation of multiple resins, and enables resolution down to 28μm.

1.2.3 Advantages over Current Fluidic Chips

As discussed previously, one of the common methods of microfluidic chip manufacture in current use is PDMS casting. This method has certain advantages for applications to biological samples. PDMS is cheap compared to silicon-fabricated devices. It is oxygen-permeable, allowed for gas diffusion for cell support. PDMS is highly hydrophobic, and therefore does not adhere to aqueous droplets.

However, traditional PDMS methods suffer from significant drawbacks. The mask, specialized equipment, and environmental controls may cost into thousands of dollars. From chip conception to finished product will take days or weeks.

PolyJet printing can produce channels on the micron scale, integrate multiple materials into a chip as required, and guarantee optical clarity for microscopy coupling. Additionally, it overcomes many of the challenges of PDMS. Chips may be rapidly design and modified at will within STL files. Print jobs require no costly photomasks and can be completed on the order of minutes to hours. Additionally, no cleanroom, silicon casts, or equipment for plasma bonding is required. PolyJet thereby massively drives down the on the cost in time and money for prototyping that is typically demanded by PDMS methods.

1.2.4 Potential Shortcomings in Microfluidic Applications

Because the silicon masters for PDMS casting are produced through photolithography, their resolution is only limited by the wavelength of light which is on the order of nanometers. This is orders of magnitude more precise than any 3D printer. Therefore, for applications requiring single micron level channels, PDMS methods would still be required. Additionally, the commercially available optically clear resins may not have adequate hydrophobicity to support stable droplet formation. If this proves to be the case, then a surface coating may be required to increase the hydrophobicity of the channels. Lastly, there may be a mismatch between the ideal CAD file design and the physical structure due to imperfections in the manufacturing process. For PolyJet printers, this usually includes clogged print heads and diffusion of the resin as it cures. At micron scales, these imperfections may have a significant effect on final channel shape.

1.3 Antibiotic Resistance

1.3.1 Properties and Mechanisms of Antibiotic Resistance

Naturally produced and synthetically manufactured molecules that are deleterious to the viability or proliferation of microbial life are referred to as ‘antimicrobials’. Antimicrobials that inhibit the viability or proliferation of bacteria specifically are referred to as ‘antibiotics’. Antibiotics come in many classes. Classes are defined by their chemical structure, and different classes often exploit different ‘mechanisms of action’, or physical methods of damaging the bacterial cell. For example, fluoroquinolones are a class of antibiotic built on a common ‘quinolone’ bicyclic core containing typically 1 fluorine atom and damage the target bacterial cell by inhibiting its topisomerase-2 enzyme, thereby preventing DNA replication. Conversely, aminoglycosides are a family of amino sugar containing molecules, which inhibit bacterial proliferation by binding to target bacterial ribosomes and prevent protein synthesis. A given

antibiotic may damage several species of antibiotics; the range of bacteria over which a given antibiotic is effective is known as its 'coverage' or 'spectrum'. Drugs that act on a wide range of bacterial types are referred to as 'broad spectrum', while those that act on only a few or even a single species is referred to as 'narrow spectrum'. Antibiotics may be broadly divided into two categories: bactericidal and bacteriostatic. These agents act on bacteria at different stages of the bacterial growth curve (Figure 3). Bacteriostatic drugs act on actively dividing 'log phase' bacteria. They function by arresting processes required for cell division such as DNA replication. In contrast, bactericidal drugs act effectively on non-dividing 'lag' or 'stationary phase' cells. These function by disrupting the integrity of the cell, such as rupturing the cell membrane. A given antibiotic's classification as bacteriostatic or bactericidal may shift depending on the target strain or the working drug concentration.

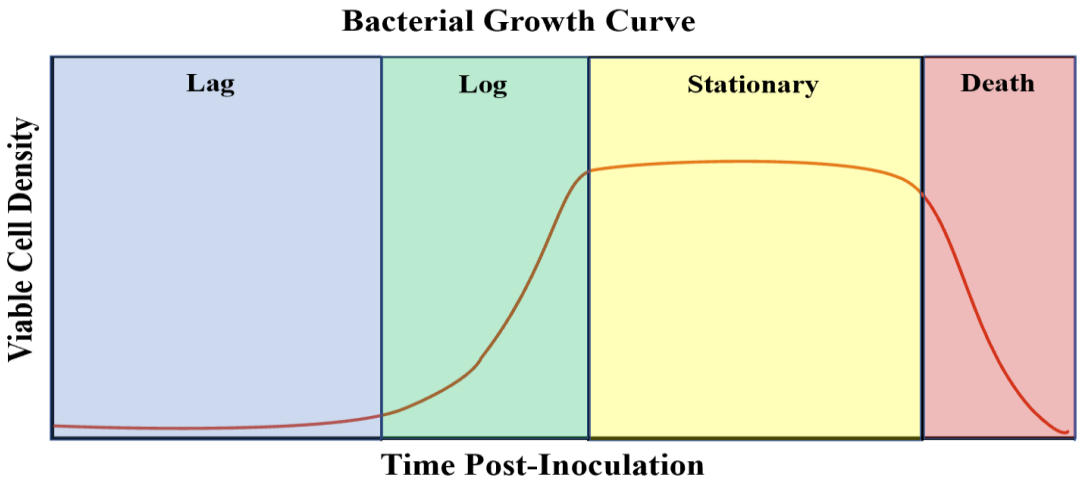

Figure 3. Bacteria follow a predictable growth pattern composed of 4 phases. Once inoculated, a low-density culture will recalibrate its metabolism to adjust to local nutrient sources. Very little growth takes place in this phase, so it is appropriately named the 'lag' phase. Following lag phase, the culture actively divides through binary fission to maximum carrying capacity. This aggressive growth follows a logarithmic pattern, hence the 'log' phase. Growth slows as the cell density reaches carrying capacity, at which point growth ceases and cell counts remain steady in the 'stationary phase'. Finally, as nutrients deplete and toxic waste products accumulate, the cells begin to die and lyse in the 'death' phase.

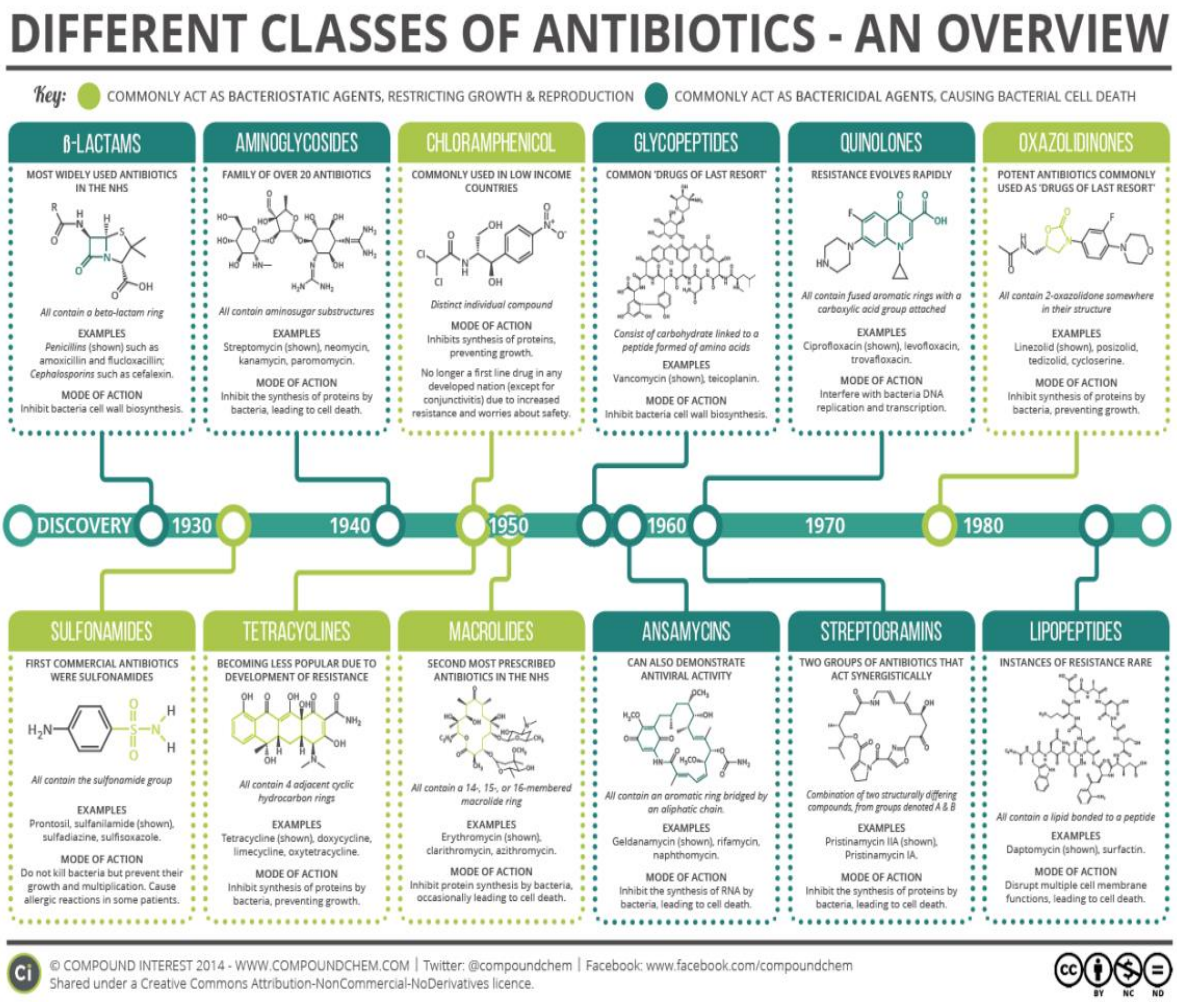

Figure 4. The table above briefly summarizes the chemical structures and modes of action of the major families of antibiotics. Table is the product of Compound Chem, 2014.

Bacteria have many methods of surviving exposure to antibiotics. Generally, bacteria undergo a genetic change to alter or otherwise protect the target of the antibiotic. For example, bacteria will frequently acquire a mutation in their penicillin-binding protein (PBP), which is both responsible for maintaining the integrity of the cell wall and the target of action for penicillin-class antibiotics. The mutation alters the shape of the PBP so that it no longer binds penicillins with significant affinity, conferring the ability of the bacteria to survive in the presence of penicillin-class antibiotics- i.e., they become ‘resistant’ to the penicillin. Bacteria

may acquire entire genetic cassettes that function to protect the strain from a given antibiotic class. Some genetic resistance cassettes code for enzymes that degrade the antibiotic or pumps that push the antibiotic out of the cell ('efflux' pumps) where it cannot take effect. Furthermore, resistance is not necessarily a mutation of the host chromosome. Often, bacteria acquire resistance in the form of plasmids, or extrachromosomal genetic elements[13]. The resistance factors, or genes which code for antibiotic resistance (degradative enzymes, efflux pumps, etc.), are often found on these modular, transmissible plasmids. Therefore, resistance can be acquired either through a novel mutation in the genome or incorporation of exogenous DNA which codes for the resistance factor.

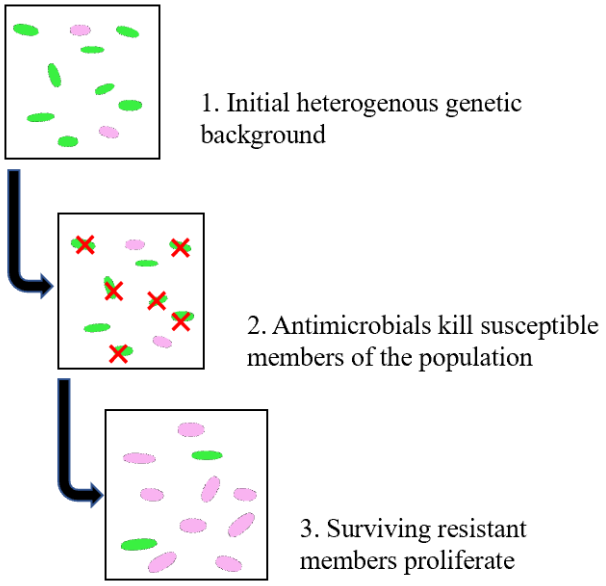

Figure 5. Bacteria can develop resistance through random mutation or acquire it from neighboring cells. Carrying genes for resistance imparts a metabolic burden, so in the absence of selective pressure the resistant strains will be maintained as a minority of the population. However, in the presence of antibiotics the susceptible fraction of the population will die, leaving a niche for the resistant strains to fill.

Resistance can be transferred between bacterial neighbors through a variety of mechanisms. In the simplest case, a resistant bacterium dies and breaks open in a process called 'lysis'. The DNA from the lysed bacteria then escapes the cell into solution. Neighboring cells which

encounter this DNA in solution can endocytose it through their cytosolic membranes into the cell in a process known as ‘naked DNA transformation’. Alternatively, neighboring cells can actively bridge their cytosolic compartments by physically linking to each other through a ‘conjugation pilus’. Resistance-coding DNA can then be shuttled across this bridge to confer resistance to the receptive neighbor. Concerningly, uptake of exogenous DNA does not require the donor and recipient bacteria to belong to the same species. Multiple species that are sufficiently similar may successfully transmit genetic material between themselves. However, the most common scenario of propagation is merely binary division of the host cell, resulting in two daughter cells carrying copies of the resistance elements.

1.3.2 Current Global State of Resistance

Antimicrobial resistance represents an imminent and growing threat to global health.[14] It is estimated that antimicrobial resistance may cause 10 million deaths a year by 2050.[15] Many factors contribute to the accelerating development and spread of resistant strains. An aging population provides a higher density of immunocompromised hosts for pathogen propagation[16]. Rapid and widespread international travel makes transmission of infectious disease much more difficult to contain. Antibiotics are used routinely in livestock feed to reduce the pathogenic burden in cattle and other commodity animals. Various abuses of antibiotics including unprescribed consumption and regimen noncompliance strongly contribute to the development of resistant strains. Additionally, antibiotics are often inappropriately used to treat viral infections. All these factors have conspired to create a highly selective global breeding ground for multi-drug resistant (MDR) and extensively drug resistant (XDR) variants.

Resistance to every known clinical antibiotic is now found across the globe. *Staphylococcus*, *E. Coli*, and *Klebsiella* showing significant resistance to fluoroquinolones,

carbapenems, and 3rd generation cephalosporins can now be found at significant rates on six continents[17]. Human deaths from resistant infections total 1.27 million per year, and the economic burden of these infections exceeds $55 billion a year in the United States alone. If the trend continues, every known antibiotic may become functionally useless in the coming decades.

Not only is resistance spreading, but the rate of spread is consistently accelerating. Penicillin, the first antibiotic to be utilized medicinally, was first purified in 1928 by Fleming. By 1942, signs of resistance had been discovered. Widespread penicillin resistance did not fully develop into a significant medical problem until the 1960s. In contrast, modern drugs of last resort (meant to be deployed only the event of an otherwise untreatable strain), are suffering a more rapid loss of efficacy. Colistin, a powerful polymyxin-class drug of last resort, was compromised when the colistin resistance plasmid MCR-1 was discovered in China in 2015. By 2017, colistin resistance had spread to 30 countries across 5 continents[17].

The problem is aggravated by a drying antibiotic pipeline. Fewer novel antibiotics are being discovered and brought to market to offset the obsolescence of older ones. Additionally, it takes an average of 15 years to bring a new drug from discovery to market, so this deficit will have persistent effects. It is critical not only to accelerate the discovery of novel antibiotics, but to exercise better stewardship over our existing antibiotic toolbox to mitigate the encroaching obsolescence of all available antibiotics.

1.3.3 Dynamics of Resistance in Hospitals

Hospitals and healthcare clinics provide a favorable environment for the proliferation of resistance. The influx of patients with infectious disease seeking treatment, admitted infirmed and immunocompromised patients, the prevalence of open wounds and sores, and the physical circulation of healthcare staff contributes to a wealth of available host opportunities for

pathogens.

Healthcare centers are also foci of intensified selective pressure, as concentrated population of admitted patients are frequently prescribed antibiotics. Use of antibiotics creates a selective pressure for the proliferation of resistant strains. This is particularly true for broad-spectrum prescriptions, which encourages growth of pan-resistance. The problem is amplified by imperfect medication compliance. Patients who do not adhere to the recommended regimen of treatment frequently stop taking antibiotics as symptoms subside and do not complete their course. This incomplete treatment often leaves the most resistant pathogens alive, which in turn re-proliferate into a more resilient relapse infection.

This synergistic interaction of a favorable host-rich environment and intense selective pressure causes the rapid generation and proliferation of MDR strains in these healthcare settings. This phenomenon is so common that a field of research and standard operating procedures have been developed around ‘healthcare-associated’ or ‘nosocomial’ infections.

Nosocomial infections have serious implications for patient outcomes. Patients who are already carrying an infectious illness or are otherwise immunocompromised will be highly likely to develop a secondary infection while admitted. These secondary infections are likely to be multi-drug resistant and extensively drug resistant directly resulting in an inability to treat them and subsequently increased fatality rate. This risk compounds the longer a patient is admitted; Each day in admission correlates to a 1.37% chance of nosocomial infection. Onset of infection increase the length of a hospital stay by an average of 9.32 days[18]. Nosocomial infections are particularly devastating to medically vulnerable populations, contributing to illness and death in geriatrics in long-term care and hospice[19].

Yet selective pressure is not only a function of hospital structure. Standard prescribing

practices by physicians are also directly contributing to resistance spread. Specifically, the practice of **escalation/de-escalation** prescription is a powerful contributor to selective pressure. Additionally, physician reliance on statistical charts known as ‘antibiograms’ (Figure 6) necessarily accepts the errors of incorrect diagnosis and rare phenotypes, and statistical arbitrage into the prescription of antibiotics. Such error adds unnecessarily to the selective pressure for resistant variants. Briefly, the physician will diagnose a patient who presents with symptoms of an infectious disease empirically on observed symptoms. This physician then often concurrently orders laboratory tests and prescribes broad-spectrum antibiotic therapy. The use for broad-spectrum antibiotics is a meant to hedge risk and ensure coverage of multiple of the most likely responsible pathogens.

Gram negative rods (a)

Percent Susceptible		PENICILLINS				CEPHEMS			LACTAMS			AMINOGLYC's			OTHERS			Urine Only	
	No. Tested (b)	Ampicillin	Piperacillin	Amp/Sulbactam	Pip/Tazobactam	Cefazolin	Cefotaxime	Cefepime	Aztreonam (c)	Imipenem	Meropenem	Gentamicin	Tobramycin	Amikacin	Ciprofloxacin	Levofloxacin	Trimeth/Sulfamethox	1ST GENERATION Ceph's [oral]	Nitrofurantoin
Achromobacter xylosoxidans	16	–	–	–	88	–	–	0	0	81	69	0	0	0	0	44	81	–	–
Acinetobacter baumannii	11	–	–	80	–	–	–	50	–	–	80	60	60	70	50	60	60	–	–
Burkholderia cepacia (d,e)	3	Ceftazidime 33%				–	Minocycline 67			–	67	–	–	–	–	–	100	–	–
Citrobacter freundii	32	0	–	0	90	0	86	100	79	100	100	97	100	100	97	97	81	–	94
Citrobacter koseri	27	0	–	0	100	100	100	100	100	100	100	100	100	100	100	96	100	–	73
Enterobacter aerogenes	39	0	–	0	70	0	65	100	85	100	100	100	100	100	95	95	97	–	5
Enterobacter cloacae	83	0	–	0	91	0	85	96	85	100	100	98	98	100	98	98	93	–	37
Escherichia coli	1022	47	–	61	90	83	89	96	89	100	100	88	87	99	74	74	67	–	94
Klebsiella oxytoca	41	7	–	85	100	66	100	100	100	100	100	100	100	100	95	95	93	–	71
Klebsiella pneumoniae	237	0	–	84	95	87	92	94	90	100	100	95	91	96	88	87	80	–	22
Morganella morganii	14	0	–	21	100	0	100	100	100	–	–	79	93	100	100	–	79	–	0
Proteus mirabilis	90	77	–	89	100	95	93	98	97	–	–	86	88	100	80	–	69	–	0
Proteus vulgaris (d)	4	0	–	75	50	0	–	100	100	100	100	100	100	100	100	100	50	–	0
Pseudomonas aeruginosa	354(f)	–	–	–	87	–	–	78	67	81	84	79	94	91	70	65	–	–	–
Ps. aeruginosa CF mucoid (e)	88(f)	–	84	Ticarcillin 81%			–	81	73	65	74	–	88	–	58	–	–	–	–
Ps. aeruginosa CF non-mucoid (e)	63(f)	–	76	Ticarcillin 61%			–	66	59	49	58	–	56	–	39	–	–	–	–
Salmonella spp. (d)	2	100	–	–	–	Ceftriaxone 100%		–	–	–	–	–	–	–	100g	–	100	–	–
Serratia marcescens	58	0	–	0	100	0	100	100	100	97	97	100	93	100	91	97	95	–	0
Stenotrophomonas maltophilia	46	–	–	Ticarcillin/Clavulanate 42%			–	–	–	–	–	–	–	–	–	82	93	–	–
Cost		$$	$$	$	$$	$	$	$	$$$	$$$	$$	$	$	$	$	$	$	$	$

(a) Until final identifications are available, reports describe gram negative rods as lactose-fermenters (LF; such as E.coli, Klebsiella, Enterobacter, Citrobacter); non-lactose fermenters (NLF, such as Proteus, Serratia, Salmonella, Shigella), or non-fermenters (NF, such as Pseudomonas, Acinetobacter, Stenotrophomonas, and others, most of which are intrinsically more resistant to many antibiotics).
(b) Not all isolates tested against every antibiotic listed.
(c) Unlike aztreonam, aminoglycosides have synergistic activity with β-lactams (ex: piperacillin, ampicillin) against aerobic gram negative rods and enterococci. Aztreonam should only be used for treating documented infections due to susceptible organisms in patients with anaphylactic reactions to β-lactams. In patients with renal insufficiency, aminoglycosides can be administered safely when doses are adjusted for patient's renal function. For information on dosing, including single daily dosing, please contact a Clinical Pharmacist (beeper # available from unit secretary).
(d) Data from isolate totals <10 may be statistically unreliable.
(e) Cystic fibrosis patient isolates tested by disk diffusion.
(f) Pseudomonas aeruginosa isolates not corrected for duplicates.
(g) Infectious Diseases consultation strongly recommended for determining treatment of Salmonella species recovered from blood.

Figure 6. An example of an antibiogram. The pathogen strains listed on the leftmost column while the available antibiotics are listed across the top. The numerical entries at the intersections indicate the probability the strain will be classified as 'sensitive' to that specific antibiotic. Lower rates of Antibiograms may be specific to regions, cities, or even specific hospitals. Physicians frequently refer to such charts to inform their prescribing decisions.

1.3.4 Shortcomings in Current State of Care

A part of the selective pressure for the spread and proliferation of antibiotic resistance may be traced back to physician prescribing behaviors. As mentioned previously, the current standard of care is a mixture of empirical deduction based on symptoms and confirmatory laboratory screens. A doctor will reach a diagnosis based on the symptoms of the disease to identify the infectious agent. They will then typically concurrently prescribe antibiotics (broad spectrum) to

cover the most likely pathogens and order laboratory tests including genetic identification by polymerase chain reaction (PCR) and screens for antibiotic tests to confirm his diagnosis. A doctor will generally not wait for the results of a laboratory test out of concern for the negative effects associated with delayed antibiotic therapy. The patient will continue the broad-spectrum antibiotics until the results of the laboratory screens. After completion of ordered tests, the laboratory will return a **sensitivity profile**, indicating which antibiotics will be efficacious in killing the pathogen. The doctor will then revert to a more appropriate narrow-spectrum antibiotic in a practice known as 'de-escalation'.

Unfortunately, the laboratory tests for antibiotic resistance are large-scale, culture-based tests which often take 3 days to return results to the prescribing physician (Figure 9). The three most common tests include the broth microdilution test, the E-test, and the Disk Diffusion Assay (otherwise known as the 'Kirby Bauer' test). The broth microdilution test involves diluting a drug along a 96 well plate and challenging a test organism in along each serial dilution. The inhibitory concentration can be directly observed by seeing the highest drug concentration in which the bacteria is able to proliferate in. The Kirby-Bauer and E-Tests are both based on a similar principle: Papers does in the drug are laid on an agar growth dish. The drug will diffuse into the agar, creating a concentration gradient which tapers off as the distance from the paper increases. Then, bacteria are permitted to grow on the agar, but are inhibited as they approach the paper as a function of their sensitivity to the drug. A wider area of growth inhibition correlates to a greater sensitivity of that bacterial strain to the test antibiotic. The Kirby-Bauer is commonly accepted as the gold standard in sensitivity testing. Unfortunately, the cell culture phase along typically takes 24 hours, and laboratory results are often not returned for 3-5 business days.

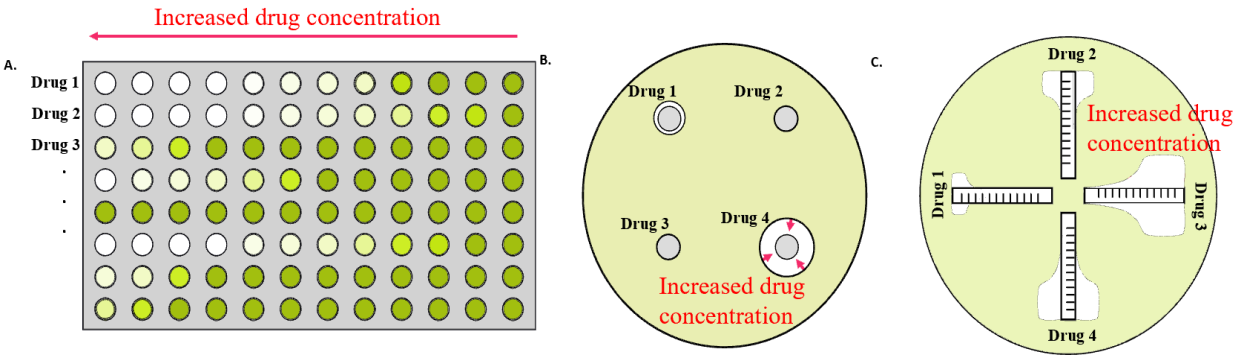

A. Broth microdilution B. Disk Diffusion Assay/ Kirby Bauer C. E-Test

Figure 7. The standard-of-care screening methods for antibiotic resistance in a typical healthcare setting. The microdilution plate features serially diluted antibiotic concentrations down the long axis to observe the growth of the queried strains across multiple orders of magnitude of drug concentration.

The escalation/de-escalation approach is a risk mitigation strategy: The physician can cover two, three or more of the most likely causative pathogens and reduce the risk of the patient not receiving an efficacious antibiotic in a timely manner. The tendency to prescribe antibiotics as quickly as possible is rooted in well-founded idea that failure to address an infection quickly correlates with rapidly deteriorating outcomes for the patient. For example, a delay in antibiotic therapy for upper respiratory infections is associated with progressively increasing likelihood of hospital admission[20]. Failure to rapidly prescribe an efficacious antibiotic for a bacterial infection may also result in **sepsis** (Figure 8).

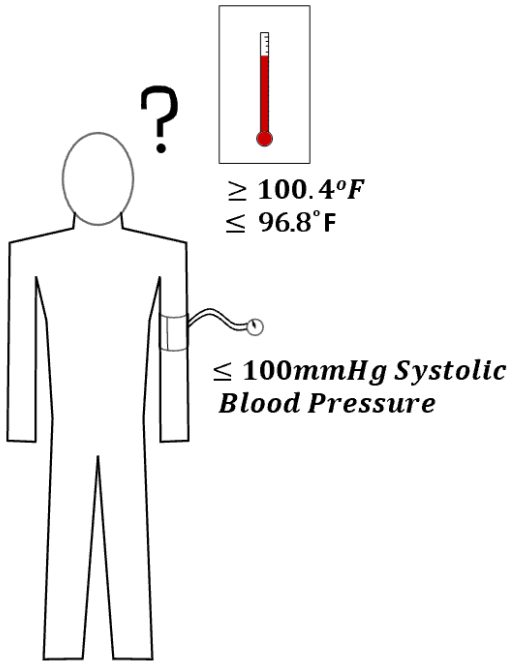

Figure 8. The signs of septic shock. As a pathogen spreads, pro-inflammatory interleukins and cytokine pour into the blood stream. These molecules cause global vasodilation and a dangerous drop in blood pressure. The effects of shock are fever, hypovolemia, loss of consciousness, disorientation and possibly death. Unless antibiotics are rapidly administers administered, sepsis may progress to septic shock, multisystem failure, and death.

Sepsis is a global, multi-system response to an infection. As the bacteria or associated toxins spreads, interleukins and inflammatory cytokines spread from local tissues directly into the bloodstream[21]. This systemic spread may result in septic shock, which is a widespread inflammation response resulting in global vasodilation, shock, disorientation, and often death. For adults with signs of onset sepsis, each hour of delay before antibiotic therapy increased the chances of shock or death by 0.42%[22]. It is therefore completely rational for a physician to err on the side of caution in initially prescribing a wide-spectrum antibiotic.

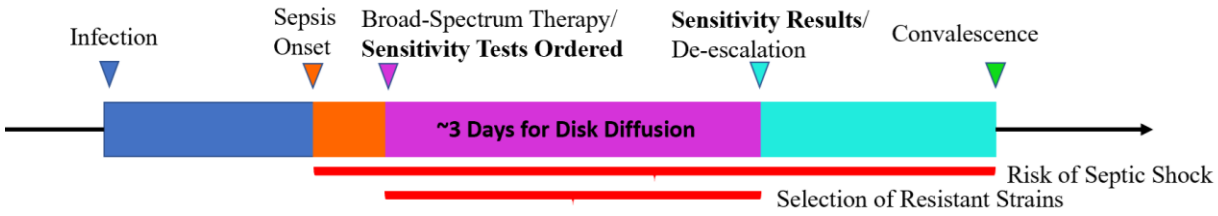

Figure 9. The timeline of an infection progressing to sepsis.

Unfortunately, the cost of hedging risk with this escalation/de-escalation approach is a widespread prophylactic and inappropriate distribution of broad-spectrum antibiotics. The selective pressure in hospitals from frequent and early prescription of broad-spectrum antibiotics creates an enormous selective pressure for the development of antibiotic resistance. This has contributed to a well-documented enrichment of broadly resistant pathogens in hospitals and other healthcare settings[23]. Unfortunately, misdiagnosis is common when patients present with infectious disease. The rates of misdiagnoses in sepsis, meningitis, spinal abscess, pneumonia, and endocarditis are 9.5%, 25.6%, 62.1%, 0.5%, and 25.5% respectively[24]. It is therefore infeasible to simply prescribe targeted narrow spectrum drugs as an initial standard of care without a screen that verifies the pathogen is sensitive to the drug.

In the light of these data, current methods of antibiotic sensitivity screening are detrimentally slow. Our inability to rapidly screen infections causes serious problems including patient mortality by sepsis, over-prescription of broad-spectrum antibiotics, and the accelerated spread of antimicrobial resistance in human pathogens.[25] Faster antibiotic susceptibility testing is required to more effectively treat sepsis and prevent the unnecessary selection for resistant pathogenic strains.[15]

1.3.5 Required Improvements to Mitigate Selective Pressure

In keeping with the guidelines of the surviving sepsis campaign, antibiotics should be prescribed within or close to 1hr of a diagnosis[26]. Kirby Bauer Tests require 18-hr for incubation alone[27]. In

hospital settings, labs using these tests often require a term of 3-5 days to return sensitivity profiles. They are therefore too slow to inform the doctor's initial prescription, and an expedited test should require

1.3.6 Adenosine Triphosphate and Turbidity as a Marker of Efficacy

Adenosine Triphosphate is a ubiquitous, universal, high liquidity transient energy transducing molecule used by every living cell on the planet to power their metabolism and nearly all life functions. It is maintained in most cells at a relatively stable concentration, consistent with the species of the cell. This concentration may raise or lower depending on the nutritional status or growth phase of the cell, but these changes are often predictable and reproducible.

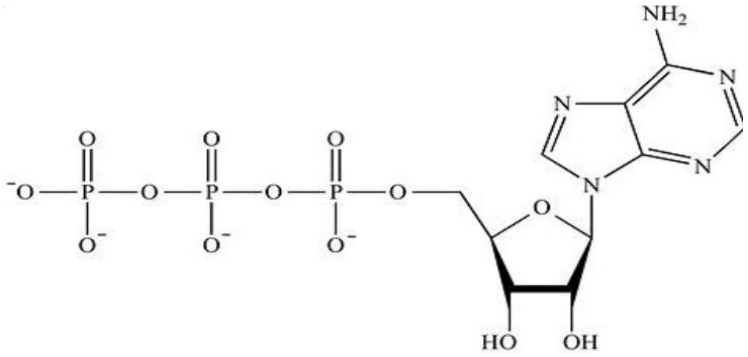

Figure 10. The chemical structure of ATP. Unstable phosphate bonds may be formed and broken to power various biochemical reactions. Every cell on Earth utilizes ATP as their primary transducer of energy to power metabolic processes.

In general, ATP may accumulate in the extracellular spaces of a bacterial culture in two different ways: lysis and purinergic signaling. Lysis is the process of a cell dying and tearing apart as it loses its membrane structural integrity. Lysis will occur for various reasons, including as the cell dies in response to stress and damage from the presence of an antibiotic. Once the cell lyses, it will spill its intracellular contents, including its enriched stores of intracellular ATP, into the extracellular spaces, increasing the extracellular concentration of ATP. Secondly, perfectly viable bacteria routinely, actively excrete ATP into the extracellular compartment in a process

known as purinergic signaling. Purinergic signaling is typically associated with communication via P2X and P2Y receptors in eukaryotic cells. However, it is increasingly recognized that bacteria make use of this communication method[28–30]. Purinergic release of ATP is regulatable by Ca2+ concentration and is shown to have effects on the growth rate, gene expression, and surface adherence behaviors of a bacterial culture[29]. This combination of dynamic purinergic signaling and cell lysis components both combine to contribute to the overall abundance of ATP in the extracellular compartment. Detection of this abundance can therefore give us information about the underlying processes taking place in the culture.

ATP is typically detected with a popular method known as the Luciferase Assay. This assay utilizes the luciferase enzyme and its luciferin cofactor to generate chemiluminescent light in the presence of ATP. Luciferin hydrolyzes ATP to power the oxidation of its cofactor in the presence of magnesium and oxygen. In the process of luciferin oxidation, the complex releases light with a peak of 550nm. This light is produced in direct proportion to the concentration of ATP. We will utilize this assay to report on the abundance of ATP in the extracellular component of the investigated bacterial cultures and make conclusions regarding the effect of antibiotic resistance-conferring genetic elements on the total ATP found in these cultures following different various antibiotic challenges. If reproducible variations correlate with the presence of antibiotic resistance, this assay will be concluded to have predictive value for resistance-associated genes.

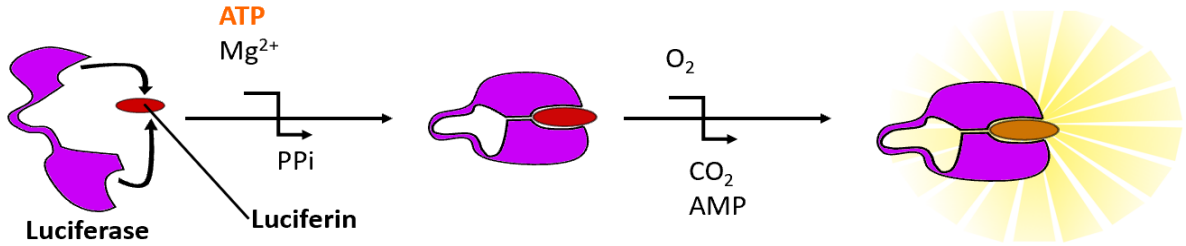

Figure 11. The luciferin and luciferase emit light at 482 nm in the presence of ATP. The intensity of the light is linearly proportional to the concentration of ATP.

Chemiluminescent assays have a distinct advantage over luminescent assays in one key respect: they require no excitation light. Thus, any light generated is due to the ATP, and the background signal will be essentially zero. Due to this distinct advantage, the luciferase assay has the potential higher sensitivity than the typical fluorescence assay. ATP can be detected down to femtogram levels.

The two common modalities of light emission detection for high-sensitivity applications are charge-coupled devices (CCD) and photomultiplier tubes (PMTs). Each method demonstrates strengths and weaknesses, and our selection here depends on fitness for purpose. Charge-coupled devices are pixel-based arrays of detectors arranged on concert with parallel arrays of capacitors. Because it is spread out in a grid pattern, CCDs may be paired grating to detect different wavelengths. PMTs, on the other hand, operate on the actions of a single-coil suspended in a vacuum tube and are typically designed to detect photons within a narrow range of wavelengths (i.e., UV or near-infrared). However, while a typical CCD performs with an amplification of 70 dB, a PMT is capable of amplifying with a performance of 140 dB, equation to a 33.1-fold improvement over CCDS. PMTs are reported to show sensitivities up to 5000 A/lm, enough to detect single photons under certain conditions. Given our emphasis on sensitivity and the predictable 550 nm luciferase emission peak, the PMT is much more appropriate for these detection experiments. Additionally, typical response times on the PMT are listed in the single nanosecond range, enabling real-time detection of changes on analyte concentration in the detection window.

Antibiotics are expected not only to influence accumulated extracellular ATP, but also on the growth and proliferation of viable bacteria. In general, we expect that in the absence of

antibiotic, the bacteria will grow the most quickly and therefore will result in the most rapid increase in cell density. Further, in the presence of antibiotic, we will expect to see a slower increase in cell density as cells die or cease proliferating, or even a drop in cell density as existing cells begin to lyse. Cell density is typically determined by its proxy: **turbidity**. Cultures with very sparse cells will have very clear media, whereas high cell-count cultures will appear cloudy and opaque (turbid). The usual metric for turbidity is the OD_{600}, or the optical transmission density measured with 600nm wavelength light as measured by a benchtop spectrophotometer. This indicates the fraction of 600 nm light that may successfully transfer through a sample of the culture without being scattered or absorbed; the more turbid the culture, the less the fraction of incident light will successfully traverse the sample.

Previous work from the Spence group by Dr. Andrew Heller have identified the ratio of ATP measurement (as reported by luciferase assay) to the turbidity (as reported by spectrophotometer OD_{600} reading) as a reliable cell-normalized measure of antibiotic-induced cell stress[31]. This metric will be included in the test results for the capillary optimization experiments.

1.4 Further Device and Tissue Applications

Beyond resistance detection, Additive Manufacturing has been used for a myriad of applied biomedical devices. These applications range from printing material that mimics human tissue with the goal tissue regeneration or organ transplant, MRI-guided reproductions of patient-specific organs to inform surgical procedures, support devices for patients or surgical staff, or the development of systems to investigate how different tissues interact *in vivo* (frequently called the ‘human on a chip’ field of study). Experiments described later may be grouped into the ‘bioprinting’ and ‘organ on a chip’ categories.

Tissue printing, or ‘bioprinting’, is a specialized field of bioprinting that replaces the use of

resins, plastics, or metals with ‘bioinks’. Bioinks are printable hydrogels or biological polymers which often contain biomolecules and suspensions of cells. Printing or curing bioinks in desired configurations allows for extremely intricate biological applications. For example, work is currently underway to bioprint macrostructures and microstructures for function human trachea and alveolar lung tissue. The fields of synthetically printed vessels and kidneys are also rapidly advancing. Importantly, bioprinting allows for the deposition of different hydrogel matrices and different cell types in complex interacting structures, more reminiscent of native *in vivo* systems. This capacity is currently being investigated to print more faithfully biomimetic organ tissue for use in modeling experiments and regenerative medicine.

Multicellular organisms are more complex than simple single-layer monocultures of cells; different cell types interact through the extracellular matrix, endocrine signaling, and physical systems such as pressure and stretch. Organ-on-a chip is the field which studies the interactions of simplified human tissues (often 3D printed) with each through direct contact, fluidic systems and 3d printed supports meant to mimic *in vivo* systems. The organ on a chip field, which has advanced the capacity to model increasingly complex systems of tissue interactions, has been advanced by the ability to print various tissue and cell geometries onto solid substrates[32].

CHAPTER 2: RAPID ANTIBIOTIC RESISTANCE DETECTION

2.1 Targeted Improvements in Current Standard of Care

2.1.1 Parameters for Improvement

There are several biological factors that may affect the concentration of ATP reached in a bacterial culture in the presence of an antibiotic. As previously discussed, the two primary contributors to the accumulation of ATP in media (the 'extracellular compartment') are purinergic signaling and release through lysis. Both contributors themselves are functions of various factors. Purinergic signaling is a function of nutritional status, growth phase, and strain type (among others). Lysis is a function of cell stress, antibiotic concentration, viral load, cell age, and other factors. The balance of these two contributors will result in the total ATP concentration for the culture at any given time.

Here, the goal is to discriminate between a bacterial strain and its drug-resistant analog. Resistance is likely to alter the rate of death and cell lysis of the culture in response to the presence of antibiotic. Resistance is also expected to maintain the viability of the cells during the antibiotic challenge, therefore increasing the number of cells participating in purinergic signaling. Further, there is often a metabolic burden for bacterial strains involved in maintaining drug-resistance conferring elements; This is partly due to the resources required to replicate copies of the plasmids or translate resistance-conferring enzymes. While it is unknown how this resource cost may alter a culture's response to a given antibiotic challenge, it is reasonable to assume that ATP release in response to antibiotic challenge or even baseline traits of a resistant strain will differ from its sensitive counterpart due to this metabolic burden. The rationale for the following experiments is to explore test conditions which maximize the differential between the resistant and sensitive strains, in a method where the signal-to-noise will be most easily detected on the

microcapillary system. The experimental conditions to be optimized include (1) The stage of growth of the culture during which the antibiotic is added (2) the concentration of the antibiotic, normalized to its accepted physiological concentration, and (3) The duration after addition of antibiotic at which measurements are made.

It is reported that purinergic signaling varies as a function of **growth phase**[28]. Specifically, most strains tend to dramatically ramp up ATP Both internal and external ATP levels vary is the culture progresses from lag phase into binary division and the decelerated growth into stationary phase. Internal ATP concentrations vary nominally due to the elevated energy requirements associated with binary division. Purinergic ATP secretion varies during the growth cycle as the culture uses extracellular ATP concentrations as a proxy for cell density.

Drug concentration is also expected to perturb the amount of extracellular ATP concentration in the culture. The effect is expected to be two-fold: Increasing levels of antibiotic will demonstrate increasing toxicity and cause progressive lysis of the culture. Lysis will release the intracellular ATP into the extracellular media. However, the increasing toxicity will also damage the growth and viability of the existing cells, dampening future growth, ATP production or purinergic signaling. It is therefore expected that varying drug concentration will have a complex, time-dependent effect on media ATP concentrations.

Finally, the **duration of exposure** of the culture to the challenge antibiotic is expected to influence the extracellular ATP concentration. Cell lysis in the presence of antibiotic is a time-dependent process. Additionally, depending on the mechanism of action, different drugs may have a different temporal effect on alterations in ATP levels. In short, some antibiotics may be more fast-acting, whereas others might have a more subtle or prolonged effect.

These factors are expected to behave differently in resistant strains and their corresponding sensitive counterparts. Our goal here is to identify the values for these parameters that cause the largest and most reproducible differential in ATP concentration between the resistant and sensitive strains. The optimization of this differential will aid in the discrimination between the strains based on differential light intensity as reported by the luciferase assay.

2.1.2 Capillary Detection System

Here, we designed a system that can detect luminescence from samples with the lowest required volume and analyte concentration (Figure 12). Analyte detection efficiency and detector sensitivity were prioritized, along with screening of ambient light to decrease environmental noise as much as feasibly possible. Finally, fine control over sample infusion rate was required for reproducibility purposes. In service of sample rate reproducibility, a syringe pump was used (Harvard Apparatus 11 Plus) to drive all fluids. Glass syringes were selected over plastic syringes for their superior loading precision and lack of flexibility. Glass syringes with a loading volume of 500 µL were selected (Hamilton Gastight Syringe 1750 Series). Couplers were comprised of Cole-Parmer luer lock – to – fingertight adapter connected female-to-male with a Cole-Parmer fingertight fitting. The tubing chosen was a Molex microcapillary tubing (Polymicro, CAT 1068150019) with a nominal internal diameter of 76 µm and outer diameter of 360 µm. Connections were secured with Cole-Parmer sleeve fittings to prevent leaks or entry of air into the system. A PMT module (Hamamatsu, H7732-1) was included at the base of the system, facing upwards. This system design was favorable for another reason: The fluidic components listed were cheap, introducing the option of disposability. To minimize the risk of exposure to potentially harmful MDR strains, system users could opt to uncouple the lines, autoclave the waste, and dispose of it safely to minimize the potential for exposure.

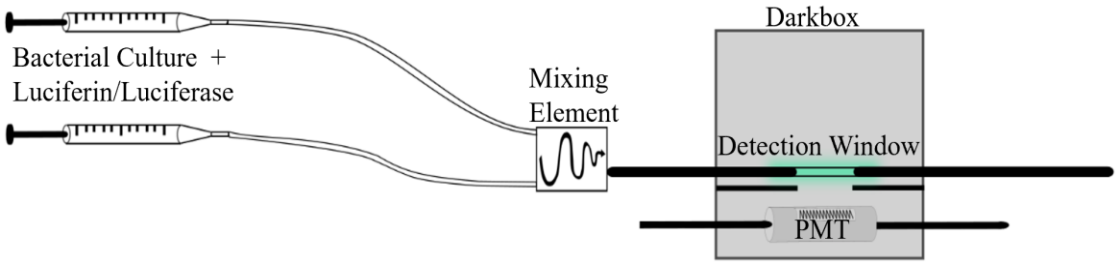

Figure 12. System of Detection utilizing microcapillaries of 72µM diameter. The bacterial culture and luciferase reporter (with luciferin cofactor) and loaded into glass syringed and fixed into a syringe pump. The syringes are pumped into a mixing element which guarantees active, homogenous mixing of the reporter and analyte. The solution is then pushed through additional tubing through a ‘detection window of transparency positioned directly above a PMT detector. The Darkbox surrounding the detection region is composed of black plexiglass, surrounded in turn by overlapping sheets of aluminum foil. Tubing and wiring inlets are sealed with black duct-tape fittings to further isolate the interior.

To extract meaningful data from the PMT, it was necessary to convert the raw signal to a digital form that can be processed and visualized. The electronic setup incorporated a PMT, voltage source (Hamamatsu module, CAT 71690, amplifier power source (Oriel Instruments Power Source, Model 7073- 60 Hz), amplifier (Oriel, Model 70710), and data logger (National Instruments, NI USB-6009) (Figure 13). The data was be fed from the data logger in digital format and processed in LabVIEW software. Initially, LabVIEW script was manually written to record voltage data as a time series. Unfortunately, these manually written scripts were unable to exceed logging rates of 30 Hz before crashing the program. The manual scripts were later replaced by a ‘Voltage- Continuous Input’ template provided open source from the company along with the NI LabVIEW 2020 distribution. This template ran seamlessly at 1,000 Hz. All future experiments described on this system were run at this collection rate. The trans-PMT voltage was supplied at 700 mV for all future experiments, and the oriel amplifier was set to 10E9 Gain. These settings were kept constant for all measurements.

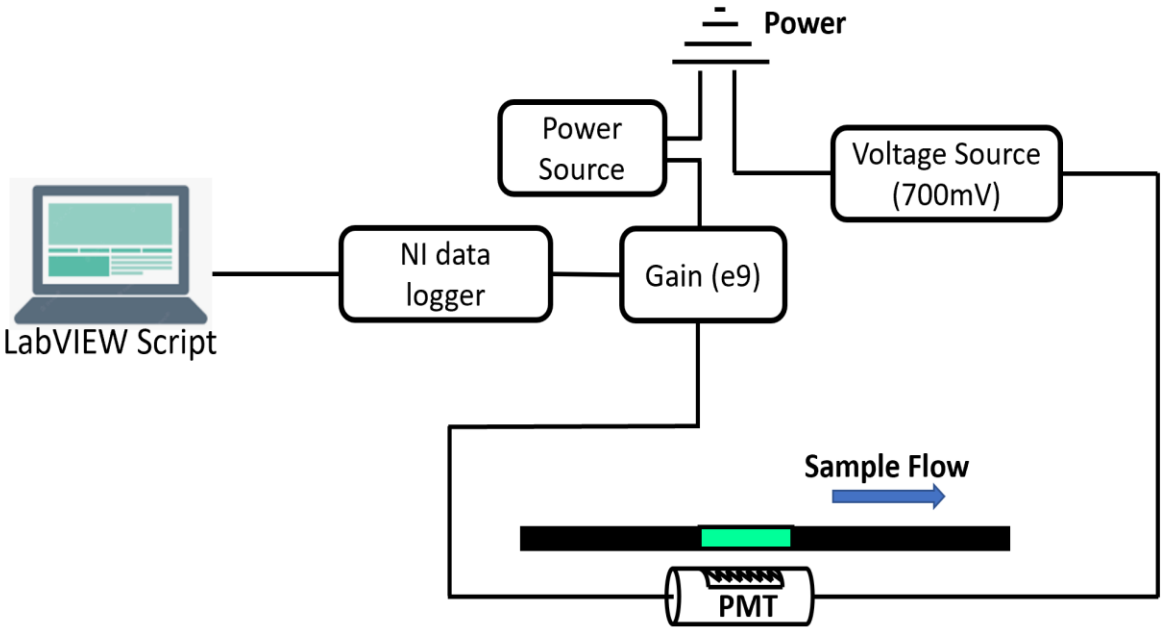

Figure 13. The electronic configuration of the data-acquisition system. The PMT was supplied a voltage through a Hamamatsu module at 700mV. Incident photons on the PMT will discharge this potential and provide a signal in the form of amperage. The amperage incident on the amplifier will be magnified using the energy supplied by the Oriel power source. The amplified signal will then be fed into the NI data logger, where a digitized value will be recorded at 1 kHz and reported to the LabVIEW program on a local computer. Data will be saved as TDMS files, which can be easily opened and analyzed in Excel.

2.2 Dual Strain Bacterial Sensitivity Model

2.2.1 Resistant and Sensitive Strains

Here, we make use of a dual-strain bacterial sensitivity model to investigate the discrimination between sensitive and resistant strains on a microcapillary system. The sensitive strain in this model is NEB5α, an *E. Coli* strain with no intrinsic resistance to common antibiotics. The sensitive strain is referred to in these experiments as Kanamycin Sensitive *Escherichia Coli* or 'KSEC'. The resistant strain in this model is designated E-pET-24a+. This culture of *E. Coli* has been transformed with the pET-24a+ plasmid which codes for the enzyme 'aminoglycoside 3-phosphotransferase' under a constitutive bacterial KanR promoter.

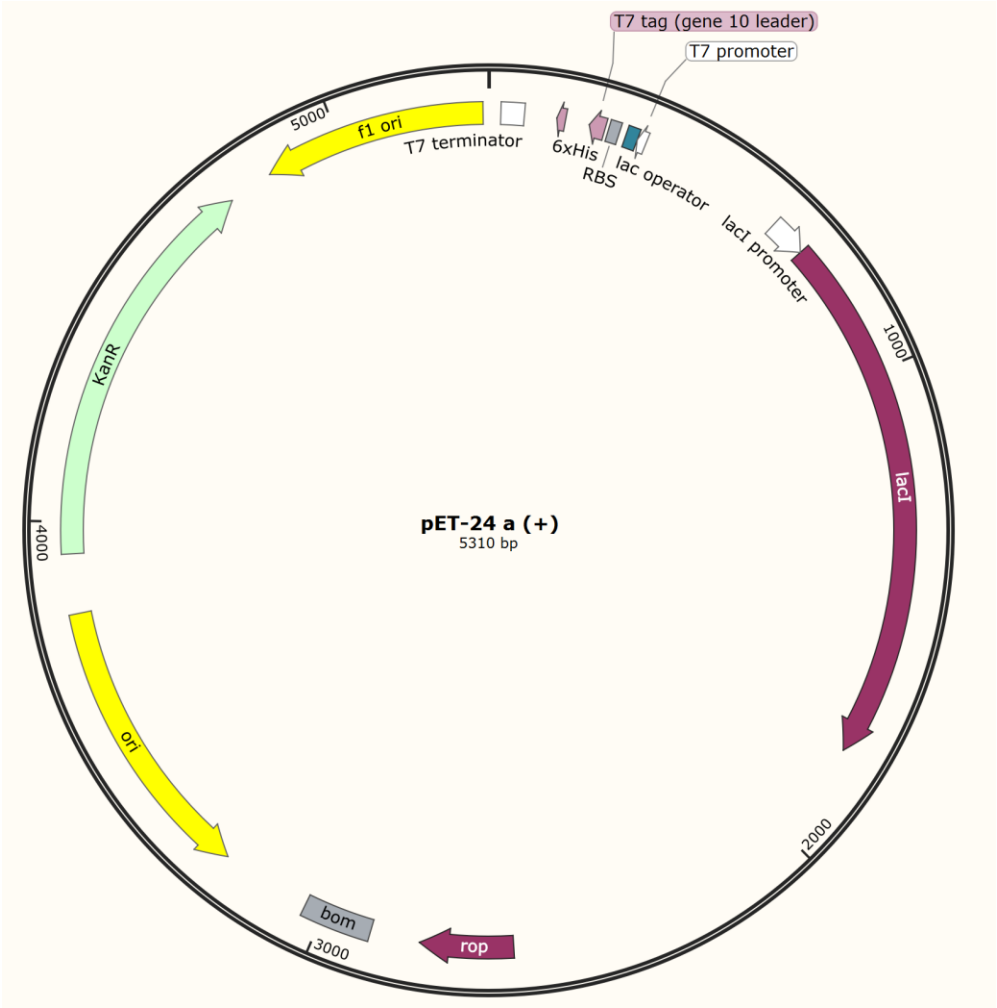

Figure 14. SnapGene rendering of pET-24a+ plasmid was transformed into *E. Coli* to produce the KREC Strain. On the left side the KanR2 cassette is visible in green (coding for the aminoglycoside 3-phosphotransferase). This cassette confers resistance to certain antibiotics of the aminoglycoside family, including kanamycin and neomycin. A constitutive bacterial promoter drives the gene.

This enzyme chemically modifies aminoglycoside antibiotic molecules by tagging them with a phosphate group, rendering them unable to interact with bacterial ribosomes (Figure 15).

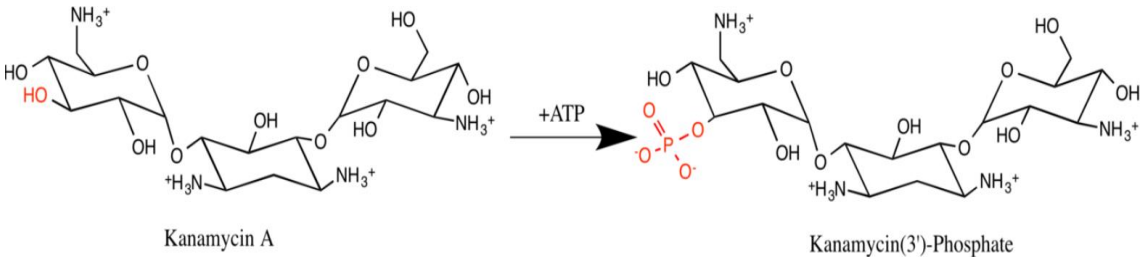

Figure 15. The enzyme-catalyzed addition to the 3' hydroxyl group of the primary amino-sugar alters the structure of the antibiotic. The new structure has a much lower binding affinity for the bacterial ribosome. Therefore, bacteria that express this enzyme can continue normal metabolic function in the presence of aminoglycoside antibiotics such as kanamycin.

Therefore, carrying the pET-24a+ plasmid confers resistance to aminoglycoside class antibiotics such as neomycin and kanamycin. The resistance, plasmid-carrying strain is referred to in these experiments as Kanamycin Resistant *Escherichia Coli* or 'KREC'.

The combination of KSEC and KREC will be challenged with antibiotics in various conditions to observe how the presence of the resistance plasmid affects the accrual of ATP in the extracellular space. These experiments will then be leveraged to optimize the microcapillary detection system. Experimental conditions which maximize the disparity in signal between KSEC and KREC will be adopted.

To better conceptualize the accumulation of extracellular ATP for these strains, a simple model is constructed (Figure 16). The first equation describes the rate of accumulation of ATP as a function of time. It states that the change in ATP is equal to the cell density of viable bacteria (V_t) times the sum of their purinergic signaling (p_t) and the faction of them which are dying ($D_{[RX]}$, the death rate at a given concentration of antibiotic) and the proportion of dying bacteria that will lyse (L) per unit time. The second equation describes the rate of change in the turbidity measurable by a change OD_{600}, over time. It states that the change in viable bacteria will be a product of the current number of viable bacteria at time t (V_t) times the exponential growth rate (k) subtracting off the proportion which are dying in the presence of antibiotic ($D_{[RX]}$). Taken

together, this model may help elucidate the contributions of both the purinergic signaling and lysis components to the accumulation of ATP in the media. What is particularly useful in this model is the observation that both turbidity and ATP concentration will behave differently if the death rate ($D_{[RX]}$) takes a different value. This indicates what we expect intuitively that the presence of antibiotic will result in disparities of ATP concentration and turbidity between sensitive (KSEC) and resistant (KREC) strains.

$$\text{I} \quad \frac{\partial[ATP]}{\partial t} = V_t(p_t + D_{[Rx]}L)$$

$$\text{II} \quad \frac{\partial[V]}{\partial t} = V_t(k - D_{[Rx]})$$

Figure 16. This system of equations is proposed to help describe both the purinergic and lysogenic contributions to the change in observed ATP levels over time. V_t – concentration of viable bacteria at time t. p_t –rate or purinergic signaling as a function of the growth cycle stage. $D_{[RX]}$ – The proportion of the culture dying at the given concentration of antibiotic 'RX'. K- the exponential growth rate characteristic of the bacterial strain.

2.2.2 Kanamycin Test Condition and Levofloxacin Control

To isolate the presence of pET-24a+ as the protective agent against kanamycin treatment, it will be useful to include a control antibiotic, against which pET-24a+ offers no resistance[33]. To satisfy this requirement, we turn to **levofloxacin**, a member of the 'fluoroquinolone' family of antibiotics and an inhibitor of bacterial type-II topoisomerase ligase activity. This inhibitor prevents the completion of new genome copies during replication and division[34]. Levofloxacin is of a different class than the aminoglycoside family, with a different structure and mechanism of action. Therefore, the pET-24a+ plasmid confers no cross-reactive protection against levofloxacin. We may designate kanamycin as the 'conditional' drug, able to damage viability

and proliferation only in the absence of the protective plasmid. Alternatively, we may designate levofloxacin as the ‘efficacious’ drug, capable of inducing cell death and cell cycle arrest in both strains, regardless of plasmid presence (Figure 17).

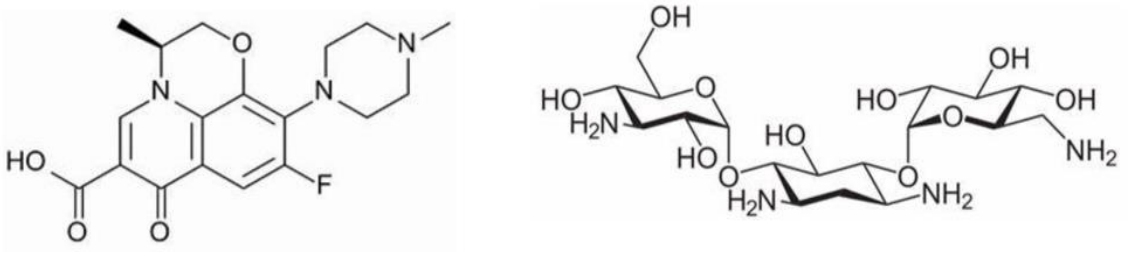

Figure 17. Dual Strain Challenge Antibiotics. Levofloxacin (left) is a member of the fluoroquinolones: fluorine-containing small molecules with the bicyclic quinolone core. Fluoroquinolones act on the replication machinery of the cell. Kanamycin belongs to the aminoglycoside family, which typically consist of 3 linked nitrogen-containing sugar groups and act to bind the ribosome. The pET24a+ plasmid will not provide protection from fluoroquinolone, due to the drastically different structure and mechanism of action from kanamycin.

Drug Interaction	KREC	KSEC
Kanamycin	+	-
Levofloxacin	-	-

Table 1. Expected drug activities in tabular format. Both kanamycin and levofloxacin in are expected to kill cultures of KSEC, whereas only levofloxacin is expected to kill cultures of KREC.

These two strains will be challenged with two separate antibiotics belonging to different classes and mechanisms of action: levofloxacin, a member of the fluoroquinolone family (bacterial topoisomerase II inhibitor), and kanamycin, a member of the aminoglycoside family (ribosomal inhibitor). The advantage of this model is that the built-in controls. The inclusion of the sensitive strain itself serves as a control against which we can compare the strain carrying the resistance plasmid (the biological control). Additionally, while kanamycin is expected to damage the sensitive strain and leave the resistant strain undamaged, levofloxacin is included as a

positive control and is expected to damage the viability and proliferation of both strains. This is expected to verify the Kan-R gene on the resistance plasmid as the causative agent of differential survival between the strains in the presence of kanamycin (the pharmacological control). Using these built-in controls, we will optimize the test conditions in such a way that maximizes the signal disparity (extracellular ATP and turbidity) between the strains. This will serve in increase the signal-to-noise and robust discrimination between strains when the bacterial system is ported to the microcapillary detection system. The behavior of the strains is initially verified by streaking the strains on plates containing Luria-Broth (LB)-Agar and plates containing LB-Agar plus 50μg/mL kanamycin (ThermoFisher, Cat. 11815032). The strains show the expected growth behavior on the streak plates. KSEC grew on the Luria Broth but failed to grow on the Kanamycin-doped plates (LB-Kan). The KREC, alternatively, grew equally as well on both plates. This initial verification shows that our strains behave as expected, and we can move forward with optimization experiments.

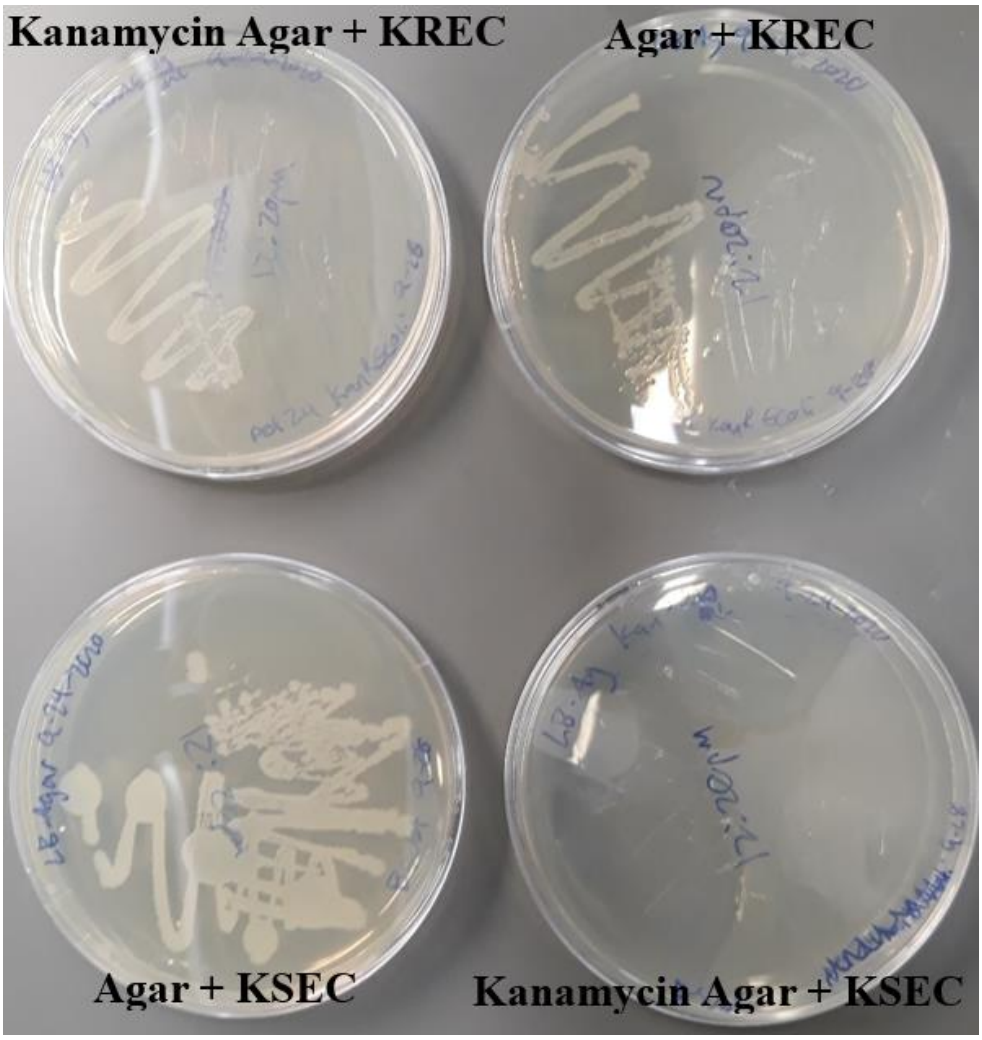

Figure 18. Dual Strain System bacteria. The KSEC grows successfully on Luria Broth (LB)-Agar plates but does not grow on LB-Agar doped with 50µg/mL Kanamycin, referred to hereafter is LB-Kan. The KREC strain grows successfully on either LB-Agar or LB-Kan.

2.3 Optimization of Microcapillary System

2.3.1 Effect of Antibiotic Exposure Time on Differential Efficacy

The effects of antibiotic exposure place on the order of minutes or hours. To identify the duration of exposure which maximizes signal discrepancy between KSEC and KREC, we run an exposure time trial. KSEC is inoculated into 5 mL Luria Broth in a 50 mL conical. KREC is inoculated into 5mL Luria Broth supplemented with 50 µg/mL kanamycin (LB-Kan). Both lids

are turned ¼ to allow for oxygen exchange. The tubes are spun in an incubator shaker 37 C, 250 rpm overnight. The overnight cultures were measured on a plate reader for turbidity (OD_{600} for LB was subtracted off), and both were diluted down to a standard lag-phase turbidity of .005 OD_{600} Into 10 mL LB in a 50 mL Erlenmeyer flask. This step standardizes the turbidity and growth phase for the strains to enable accurate comparisons. The dilutions were capped with loose-fitted aluminum foil to allow gas exchange. The dilutions were placed in a benchtop incubator shaker at 37 C 25 0rpm for 2hr to allow them to reach log phase. Split tubes into 500 µL aliquots in 15mL falcon tubes. Half the tubes from KSEC (6) were designated 'kanamycin' tubes, and the remaining 6 tubes were designated 'control' tubes. KREC tubes were similarly designated. Each series of tubes were designated t_0, t_{20}, t_{40}, t_{60}, t_{80}, and t_{100} indicating the incubation time in minutes. Kanamycin tubes were supplemented with 50 µg/mL kanamycin. The tubes were vented for gas exchange and returned to the incubator-shaker. Tubes were removed from the incubator and measured at their corresponding time points (t_0 at 0 minutes, t_{20} at 20 minutes, etc.). 250 µL cell suspension was moved to a transparent 96 well plate and measured for OD_{600}. The remaining sample was spun down at 2000*g* for 5 minutes to pellet the cells out. The supernatant was removed for ATP measurement. Reporter was prepared as follows: 1 vial of Firefly lantern extract (Sigma, F6303) containing luciferase was co-dissolved with 5 mg luciferin (GoldBio, CAT: LUCK) in 3 mL milli-Q water. The solution was mixed gently by inverting to not damage the enzyme. This mixture is hereafter referred to as Luciferin/Luciferase or 'L/L' mixture.

To measure the ATP, 100 µL of the supernatants were added to a black 96 well plate. Ten seconds before reading, 40 µL L/L was mixed into the supernatant with a multi-channel pipette. The plate was then read on a spectrophotometer on luminescence mode with an integration of

500msec. Experiments were run in triplicate. Errors were reported in +/- 1 standard deviation (Figure 19).

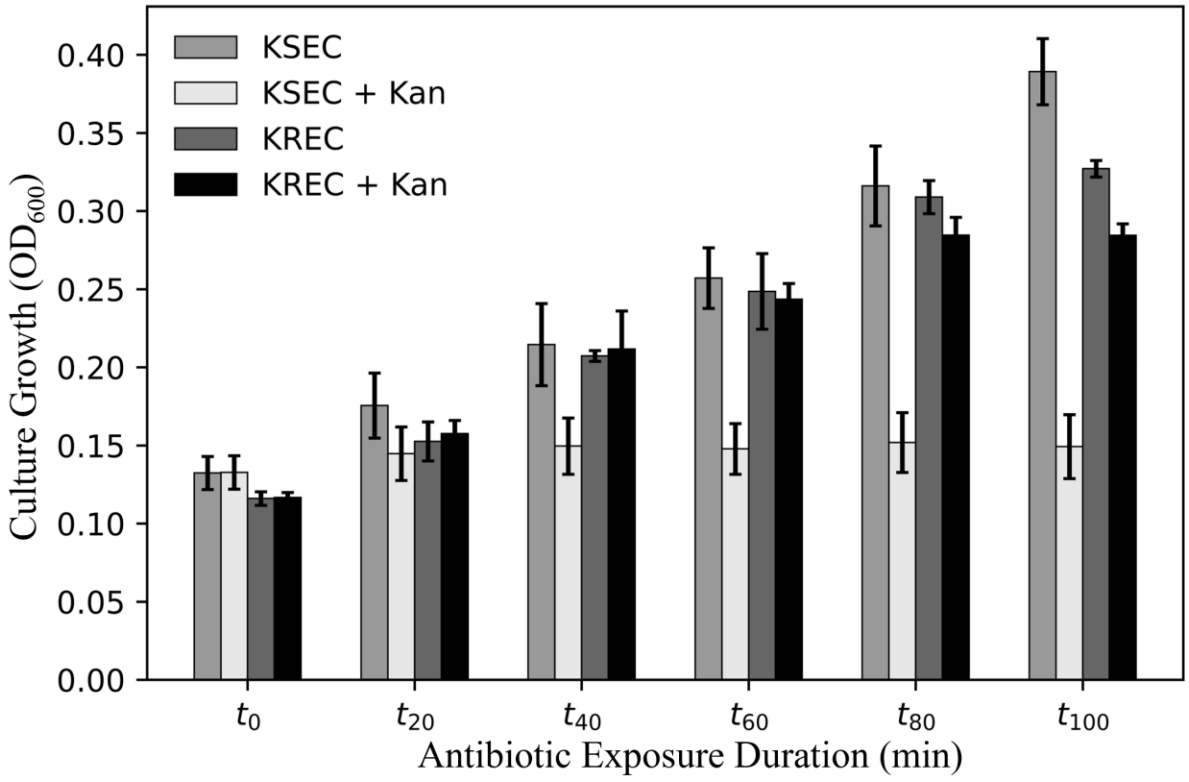

Figure 19. Cell density as measured turbidity is shown as a function of exposure time to incubation.

KSEC grows linearly in the absence of kanamycin over this period, whereas kanamycin totally arrests its growth throughout the entire course of the experiment. This is due either to a bacteriostatic arrest of its binary division or a lethal effect that has actively killed the entirety of the culture. Alternatively, KREC grows both in the absence and presence of kanamycin. The KREC + kanamycin condition shows a mild to moderate decrease in turbidity compared to untreated KREC, suggested milk residual toxicity from kanamycin. However, the culture is largely unaffected by the presence of the antibiotic.

It is also necessary to investigate the ATP release from these conditions to get a proxy for how the combined effects of purinergic signaling and lysis shift between the strains. Additionally,

once this data is collected, it will be necessary to construct our synthetic metric of cell-normalized ATP release (RLU/OD_{600}) to get a sense of how much ATP is released per-cell in the culture. This metric was shown to be useful in approximated cell stress in earlier work by the Spence Group (Heller, et.al.)[31]. The ATP chemiluminescence data is shown below (Figure 20).

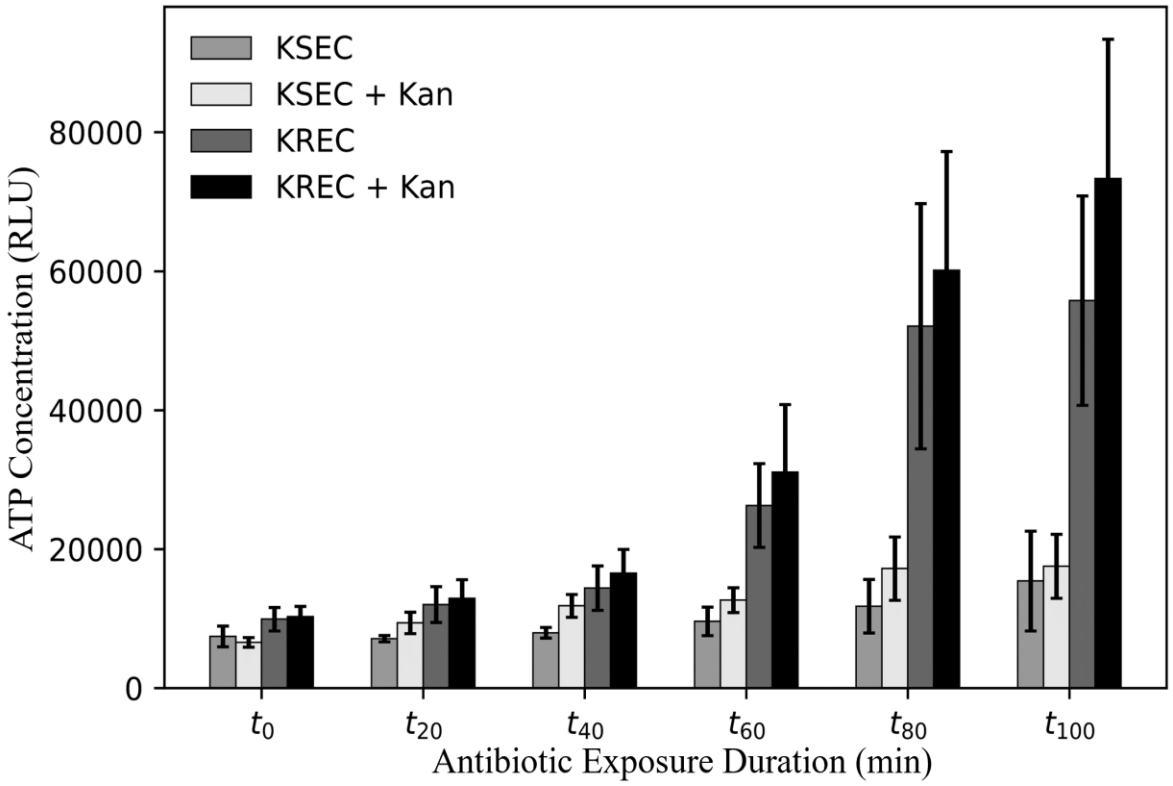

Figure 20. The chemiluminescent signal generated from mixing of culture supernatant and L/L reporter is shown above.

The ATP seems slightly increase in the intreated KSEC strain as time progresses. It is reasonable to assume that cells are not dying at a significant rate in a log-phase culture, so this increase is likely due to purinergic signaling released during growth phase. Interestingly, the concentrations of ATP in the untreated KREC increased ~5 fold over the course of the experiment, which was not expected. This may indicate increased purinergic signaling, or possibly cell-stress induced by the metabolic burden of carrying and copying the plasmid as well as constitutively expressing the Kan-R resistance protein. Resistance plasmids are known to

confer a fitness burden to carrying strains, which may account for this difference. Lastly, we see a potential (non-statistically significant) increase of ATP in the kanamycin treated KREC compared to untreated KREC, indicating potential low-level toxicity and cell lysis of kanamycin on the resistant strain.

Now that the ATP and turbidity data has been collected, it is possible generate the synthetic cell-normalized stress metric data. The results are shown below:

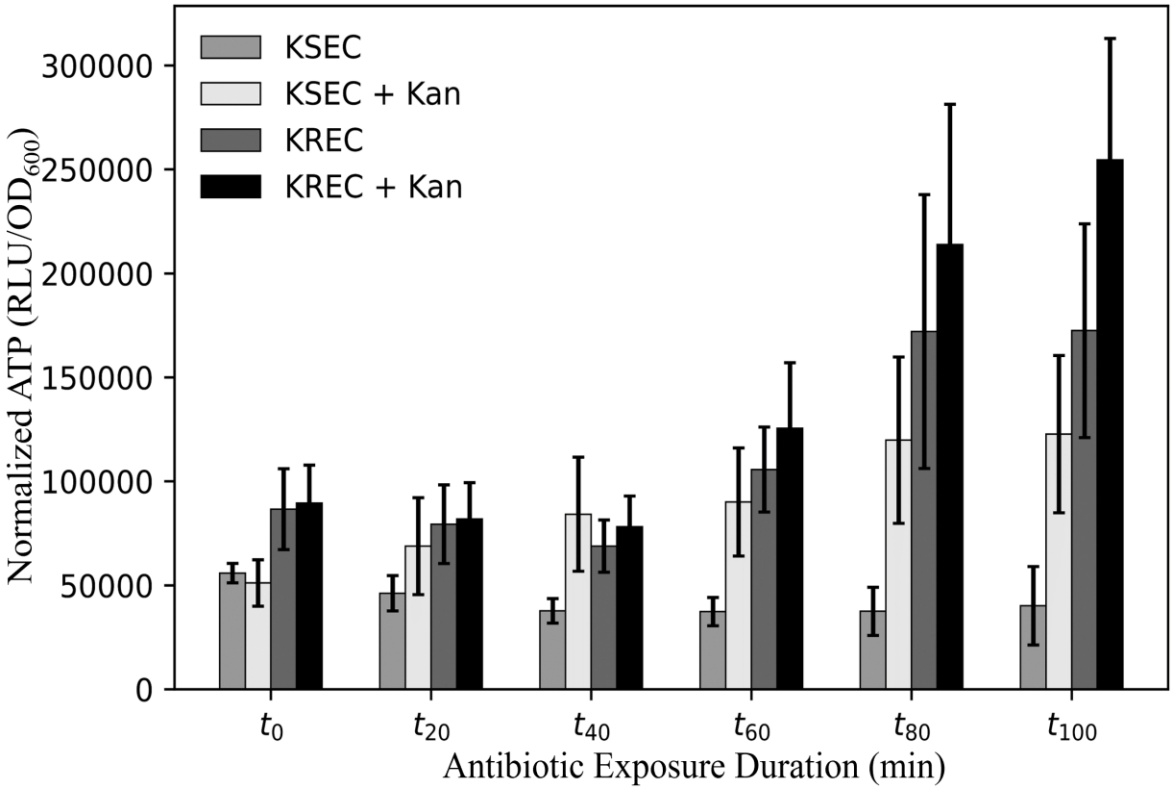

Figure 21. The ratio of the ATP signal to turbidity generates the 'cell-normalized' metric for cell stress. This is reported for up to 100 minutes of antibiotic exposure.

The cell-normalized ATP for untreated KSEC seems to taper off over time as the culture approaches stationary phase. This observation aligns well with the finding that purinergic signaling peaks during log phase growth and tapers off after approaching stationary phase. Cell-normalized ATP in the kanamycin treated KSEC samples showed a steady increase through all time points, likely indicating a delayed lysis of the dead and dying cells in culture as they lose

structural integrity. Untreated KREC has both a higher initial per-cell ATP release, but an upward trending value as the culture continues to grow. This may indicate either low rates of cell death or structural instability; either of these may be attributed to the metabolic burden of maintaining the pET-24a+ plasmids and constitutive expression of the resistance enzyme. Lastly, we see an elevation in ATP per cell in kanamycin treated KREC compared to untreated KREC. This is consistent with the turbidity data in suggesting low-level toxicity of the kanamycin to the KREC Strain.

Lastly, it will be necessary to calculate the perturbation of the kanamycin on each strain by subtracting the control (untreated) cell-normalized values from the corresponding kanamycin treated cell-normalized values to see the perturbation in the per-cell ATP release that can be attributed to the kanamycin. This data should elucidate the time points which are most effective at generating the largest differential in signals between the strains.

The perturbation data is shown below:

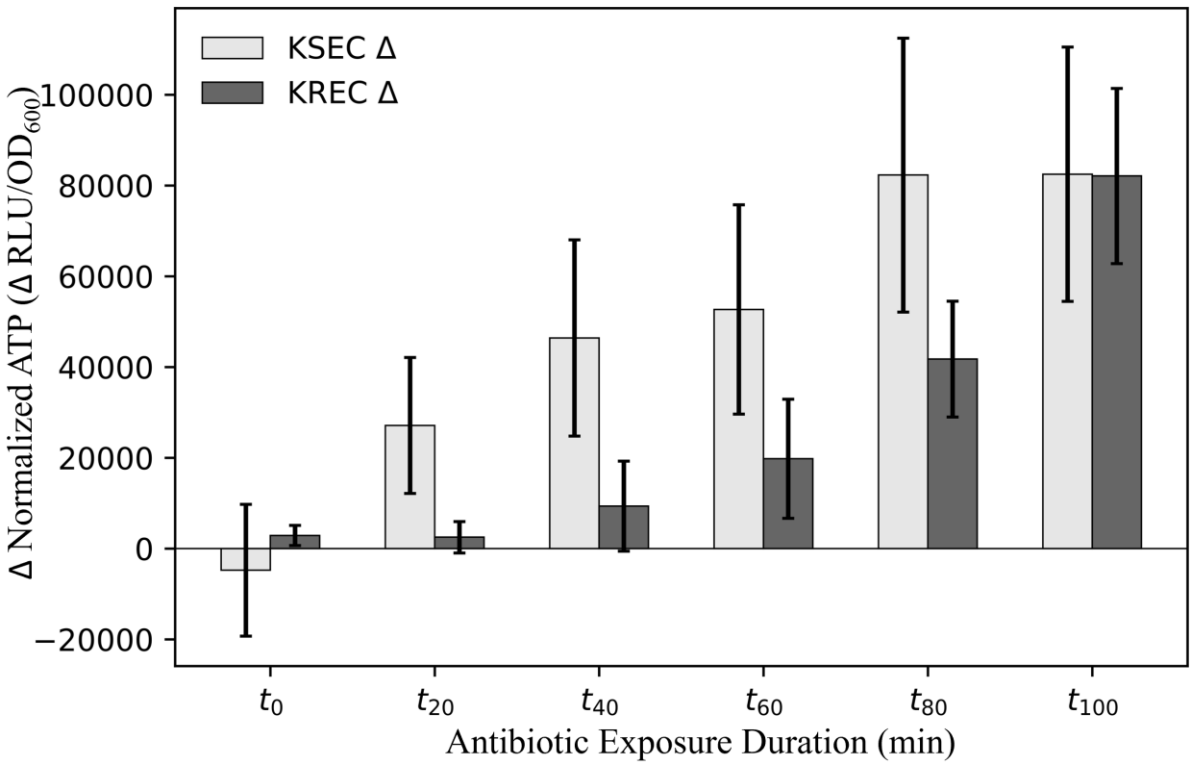

Figure 22. The perturbation on KSEC caused by kanamycin appears to asymptotically approach ~80,000 RLU, whereas the same perturbation on KREC follows a logarithmic approach to the same value. This leaves a gap of differential perturbation in the middle time points which is largest between t_{40} and t_{80}. While these differentials are similar in magnitude, t_{40} is selected in the interest of making the test as rapid as possible.

It is determined by these experiments that 40 minutes is the optimal antibiotic exposure time to magnify the differential signals between the KREC and KSEC strains. It will also be required to investigate the effects of increasing drug concentration (relative to standard physiological concentrations) and growth curve effects of the culture. Once these parameters are optimized, it will be prudent to run the optimized screen on the microcapillary system.

2.3.2 Effect of Antibiotic Concentration on Differential Efficacy

Zero concentration antibiotic will not produce any antibiotic stress on either KSEC or KREC. Similarly, oversaturated drug will at some elevated concentration entirely kill both KSEC and KREC, releasing all ATP stores into the extracellular compartment. Neither of these extreme

conditions will be diagnostically useful. It will be required to find an intermediate drug concentration which will generate the largest signal discrepancy between the sensitive and resistant strains.

Kanamycin will be included as the conditional drug and is expected to show toxicity to KSEC at much lower concentrations than it shows toxicity to KREC. Levofloxacin, being the pharmacological control, is expected to demonstrate similar toxicity to both cell lines. Given that in the exposure duration experiments KREC showed signs of stress (likely from the metabolic burden of carrying a constitutively expressed plasmid) it may be more susceptible to toxicity from levofloxacin than KSEC.

KSEC was inoculated into 5 mL LB in a 50 mL falcon tube. KREC was inoculated into 5 mL LB-Kan in a 50 mL falcon tube. Lids were opened ¼ to permit gas exchange and placed in incubator shaker overnight, 37 C 250 rpm. The tubes were retrieved at 16 hr. The tubes were measured for turbidity using OD_{600} (background OD_{600} of LB was subtracted off). Both strains were diluted to .005 OD_{600} in 10 mL LB in a 50 mL Erlenmeyer flask and capped with loose-fitting aluminum foil. As before, these flasks were spun in a desktop incubator shaker for 2 hr, 37 C, 250 rpm to bring the cultures to log phase.

Sample 15 ml falcon tubes were labeled in four series of five conditions. The series were: KSEC + kanamycin, KSEC + levofloxacin, KREC + kanamycin, and KREC + levofloxacin. Each series contained 5 tubes, corresponding to log-scale concentrations of 0x, 1x, $10^{1/3}$x, $10^{2/3}$x, and 10x. These values represent scalar multiples of the commonly accepted physiological concentrations for these drugs. The commonly accepted physiologically active concentrations are 50 μg/mL for kanamycin[35] and 5 μg/mL for levofloxacin[36]: 1x would correspond to exactly these values, and 10x would correspond to a ten-fold increase in concentration over these values. It is

expected that 0x will demonstrate no antibiotic-induced stress on the cultures, whereas 10x is expected to result in complete lysis of both strains.

Sample tubes are dosed with their labeled concentration of challenge drug and returned to the incubator shaker at 37 C and 250 rpm for 40 min. After 40 min, tubes were removed from the incubator shaker and processed for turbidity and ATP concentration Aliquots of 200 μL were loaded onto a clear 96 well plate and measured by OD_{600}. The remainder of the samples were centrifuged at 2000*g* for 5 minutes. The supernatant was retrieved for ATP measurements.

The turbidity results are shown below:

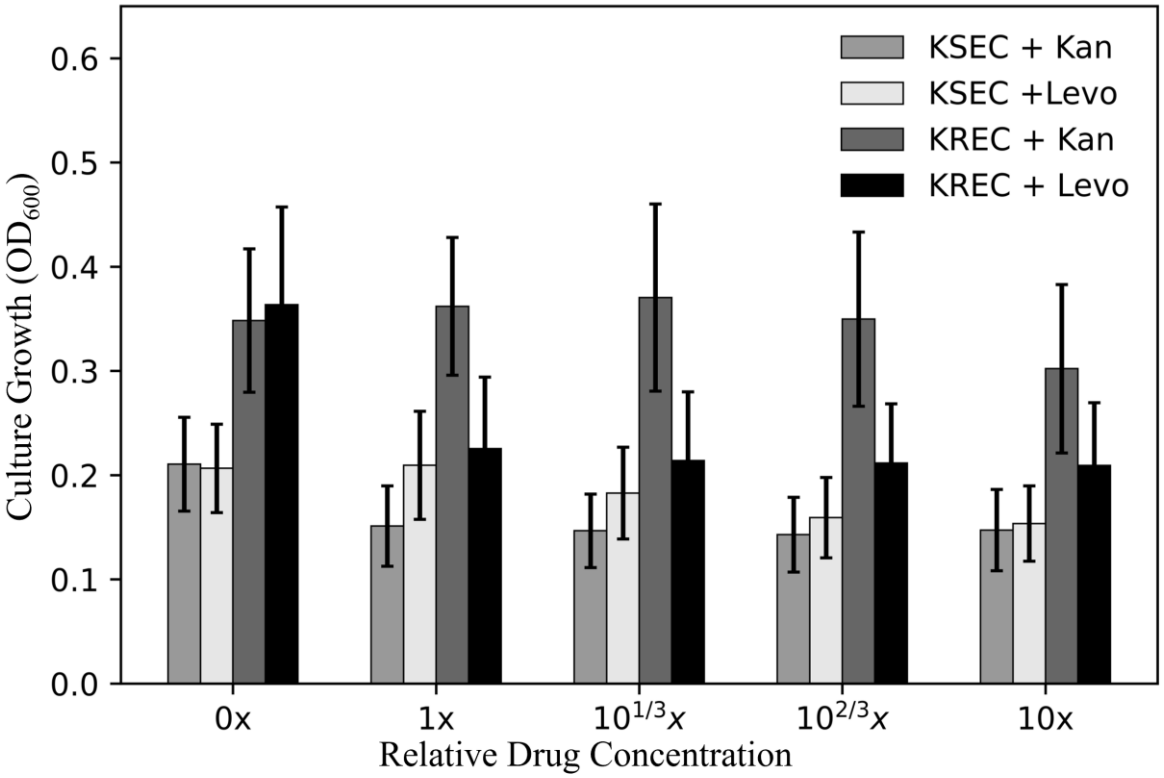

Figure 23. The turbidity of KSEC is reported at the end of the 40-minute exposure to both kanamycin and levofloxacin. The same data is shown for KREC.

KSEC appears to decrease to ~1.5 OD_{600} at 1x concentrations of kanamycin and remain statistically at that level at higher kanamycin concentrations. In conjunction with the exposure duration data, this loss may correspond to the total lysis of the culture. It is possible that the

remaining turbidity is the contribution of the lysed cells. KSEC shows a more gradual loss of turbidity starting at the $10^{1/3}$x concentration. In contrast, KREC shows no decrease in turbidity in the presence of kanamycin, as expected. In contrast, KREC shows a sharper exponential decay in turbidity than its KSEC counterpart. This is consistent with the idea that KREC suffers a metabolic burden (or 'fitness penalty') from carrying the pET-24a+ plasmid.

The supernatants are recorded by adding 100 μL to a black 96 well plate and, 10 seconds pre-recording, mixing 40 μL of L/L reporter by trituration, and recording by spectrophotometer on luminescence mode at 500msec exposure time.

The ATP results are shown below (Figure 24):

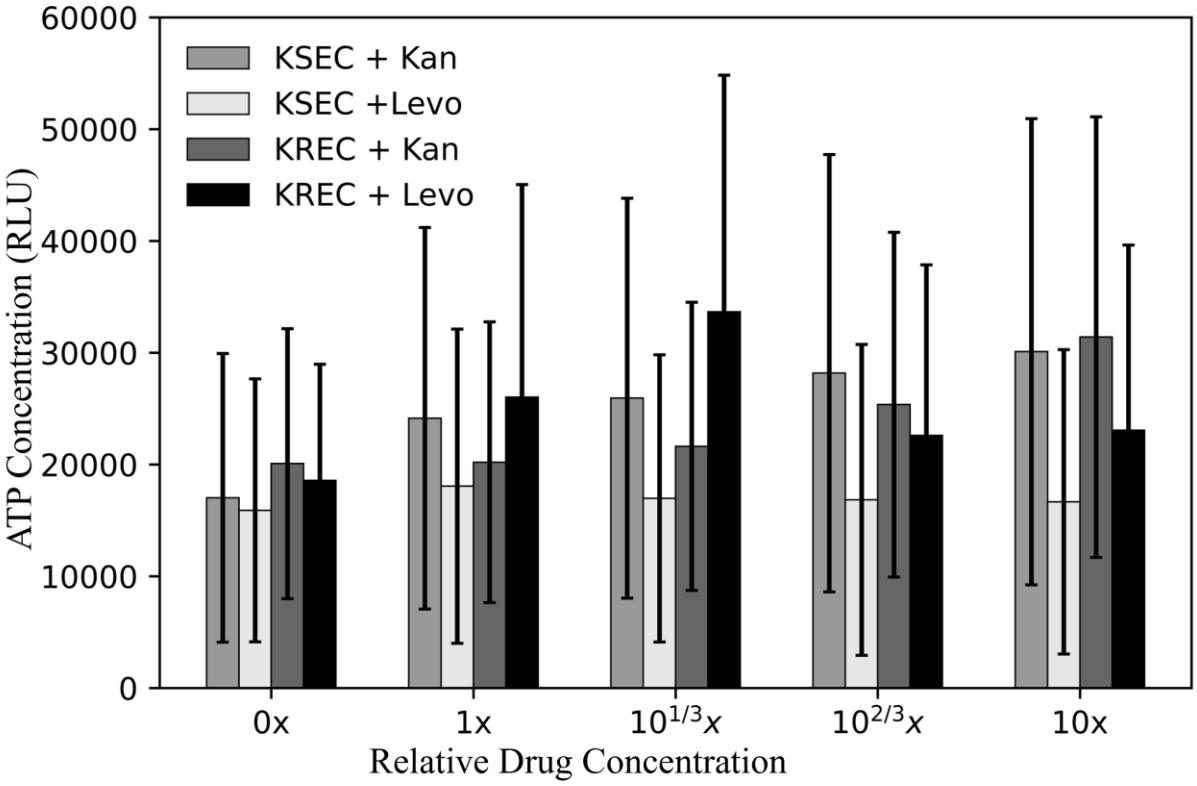

Figure 24. KSEC supernatant ATP levels are shown in the presence of increasing levels of kanamycin and levofloxacin. The corresponding KREC data is shown in the data series on the right.

KSEC showed an immediate jump in ATP concentration as early as 1x kanamycin,

consistent with the exposure duration data. This most likely indicates a rapid lysis of the culture and release of intracellular ATP stores into the extracellular supernatant. KSEC in the presence of increasing levofloxacin shows no such pattern. It is possible that the levofloxacin is merely inducing a bacteriostatic effect and not actively lysing the cells, or that the shifts in purinergic signaling and lysis-induced release are offsetting each other. KREC shows a more gradual increase in signal as kanamycin increases, perhaps as the drug begins to outcompete the enzyme. KREC signal in the presence of increasing concentrations of levofloxacin appears to spike and then decrease; it is difficult to explain this complex behavior and merits more investigation.

Taking the ratio of ATP to their corresponding turbidity measurements as before, it is possible to evaluate the cell-normalized ATP release in the presence of various concentrations of the challenge antibiotics. When the metric is graphed, an interesting pattern emerges (Figure 25).

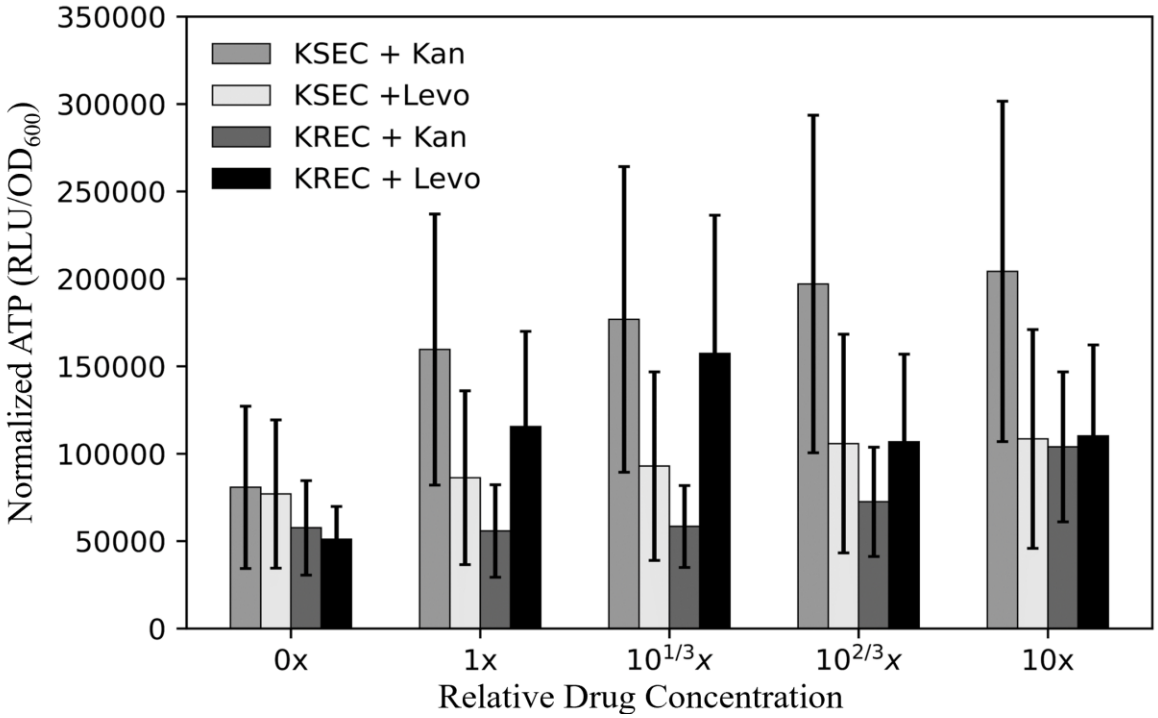

Figure 25. KSEC cell-normalized ATP release in the presence of increasing concentrations of kanamycin and levofloxacin are shown in the two series on the left. The corresponding KREC values are displayed on the pair of series on the right.

The cell-normalized ATP values for KSEC increase with increasing amounts of kanamycin. This is consistent with the idea of the culture dying and lysing. KSEC does not show a growth trend for cell-normalized ATP with increasing levofloxacin, further supporting the idea that levofloxacin is exerting a bacteriostatic effect on the strain rather than a lytic one. KREC shows no increase in cell-normalized ATP until the highest (10x) concentration of kanamycin, consistent with our expectations. It appears that the highest concentration of kanamycin shows signs of the antibiotic outcompeting the protective enzyme and causing cell damage on the KREC cells. Lastly, we again see a complex behavior in the KREC strain in the presence of increasing levels of levofloxacin. The increase and decrease is difficult to account for: perhaps intermediate concentrations kill the culture fast enough to induce constant lysis, but slow enough to allow for continued growth and purinergic signaling.

To find the ideal resolving concentration, it is important to calculate the difference between the kanamycin and levofloxacin effects. The differential was calculated by subtracting the kanamycin-treated value from the corresponding levofloxacin value (of the same strain and relative concentration).

The perturbation results are shown below (Figure 26):

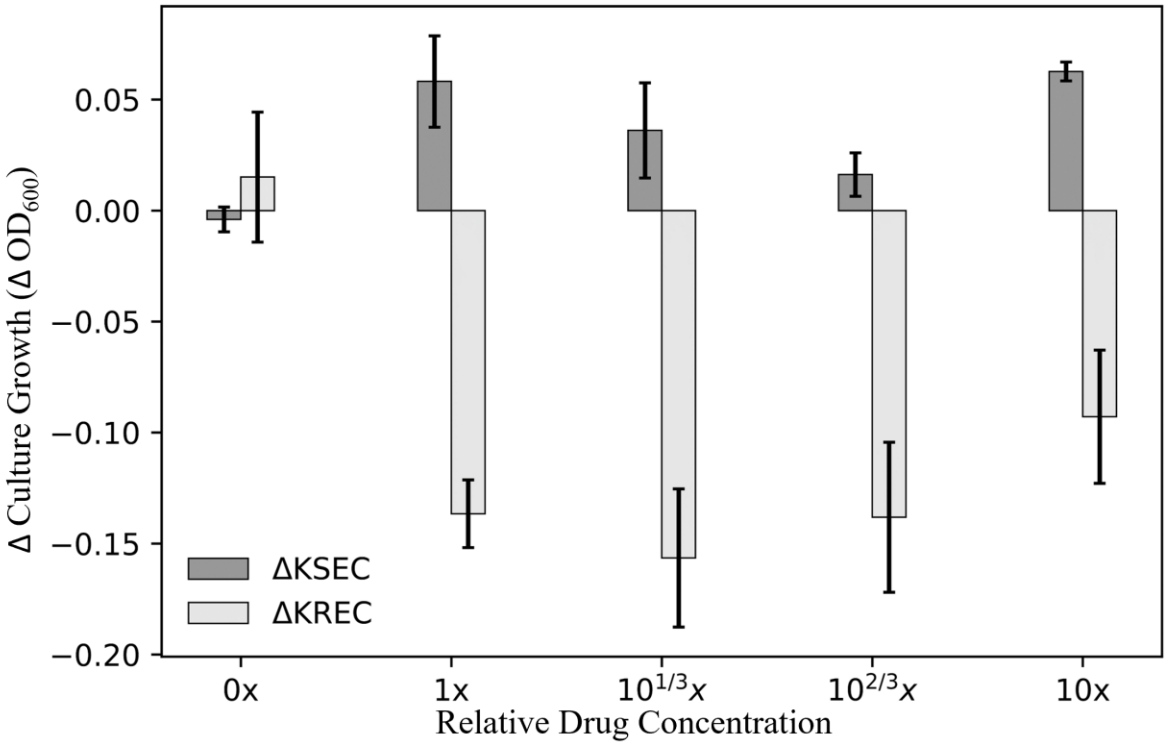

Figure 26. The difference in signal between the levofloxacin-treated samples and the kanamycin-treated samples (L – K).

The largest discrepancy between the differentials will provide the most robust window for discrimination between the strains. The 1 and $10^{1/3}$x conditions have a similar overall magnitude differential, but the 1x condition shows relatively smaller error.

To further explore the resolving capacity of each relative drug concentration, perturbation values were calculated by subtracting off the 'zero' concentration value from each corresponding sample, to get a sense of how that drug concentration perturbed the cell density compared to the untreated strain. Then, the perturbation difference between the two strains in response to a given antibiotic condition was calculated by subtracting off the KREC perturbation value from the KSEC perturbation value for both kanamycin and levofloxacin. Results are shown below (Figure 27):

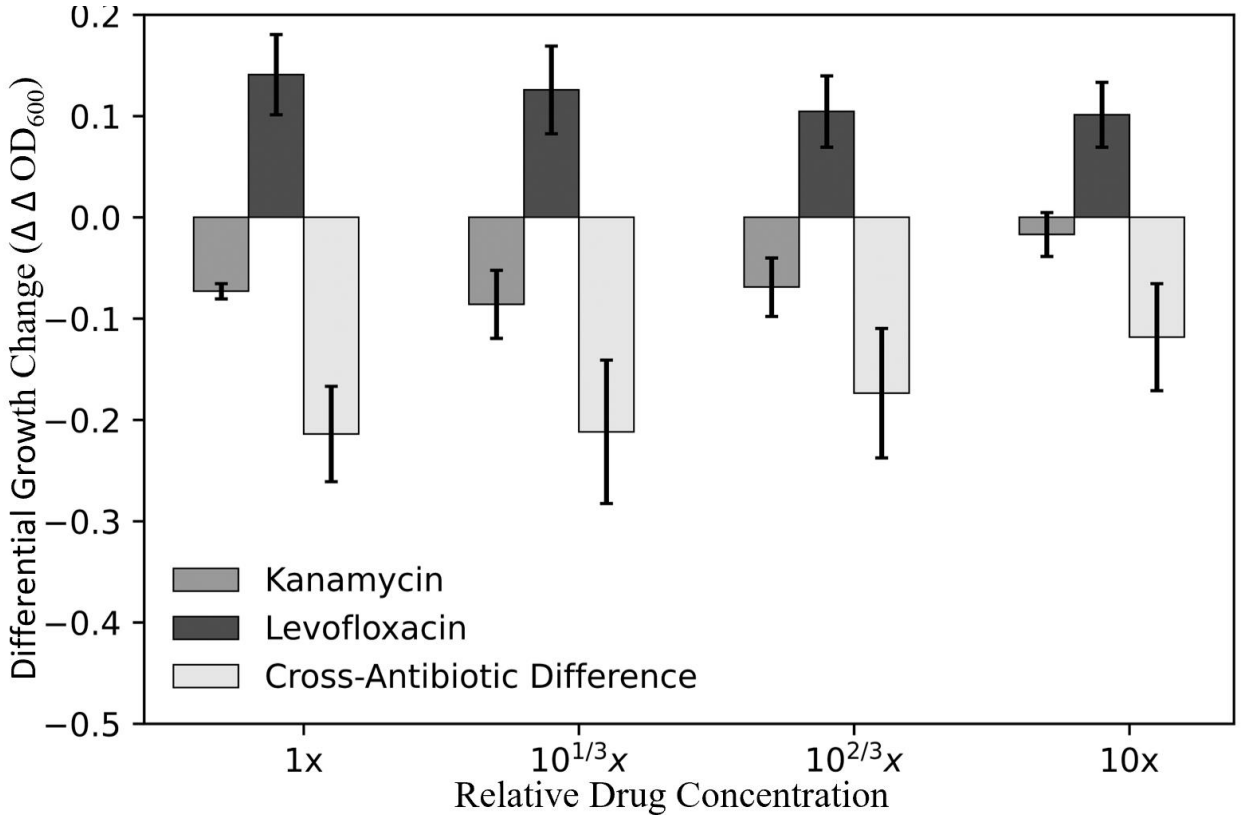

Figure 27. The value show the discrepancy between how much the antibiotic perturbs the cell density of each strain (ΔKSEC - ΔKREC).

Across all relative concentrations, we see a highly reproducible negative value for kanamycin and a highly positive value for levofloxacin. However, the trend loses magnitude as the relative concentrations increase. The highest magnitude and signal to noise ratio is found at the 1x concentration. This indicates that the largest and most reproducible signal can be found utilizing the 1x relative drug concentration, corresponding to a 50 μg/mL kanamycin and 5 μg/mL levofloxacin. These drug concentrations will be used for experiments going forward.

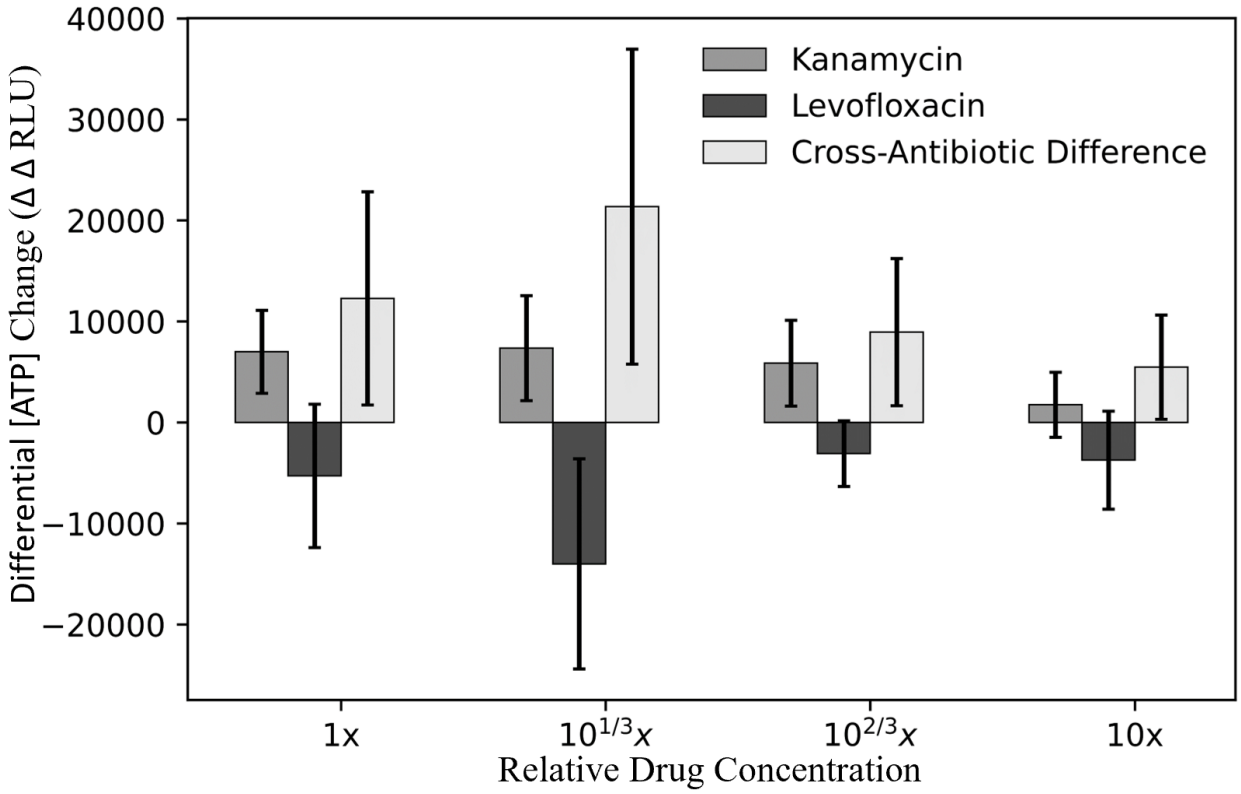

Figure 28. The value show the discrepancy between how much the antibiotic perturbs the ATP of each strain (ΔKSEC - ΔKREC).

The aggregate data suggests that 1x or $10^{1/3}$x are reasonable selections for use in future experiments. That both the perturbation and differential turbidity data show an optimum at 1x, as well as to enable direct comparison to other works in the literature that make use of the 50 ug/ml kanamycin and 5 ug/ml levofloxacin concentrations, 1x was accepted as the concentration to be used in future experiments.

2.3.3 Effect of Growth Curve on Differential Efficacy

The final parameter to be explored will be progression along the growth curve. As previously mentioned, a given antibiotic with a certain mechanism of action will either suppress the active division cells (bacteriostasis) or induce lysis in non-dividing cells (bacteriolysis). Additionally, damage to a culture at various stages of the growth curve will result in different

effects on ATP levels, due to unequal cell numbers and enhanced purinergic signaling during late logarithmic phase. It is reasonable to expect that introduction of antibiotic at different stages of the growth curve will cause different effects on the strains of our dual model system. To this end, we will add antibiotic to the strains at different points in their growth curve, allow the antibiotic to take affect over a limited period, then test the sample for ATP and turbidity levels.

Specifically, KSEC will be inoculated into 5mL LB and KREC will be inoculated into 5mL LB-Kan in 50mL falcon tubes. The tubes were placed in the incubator shaker at 37 C 250 rpm overnight. At 16 hours, the tubes were retrieved and measured by spectrophotometer for turbidity using the OD_{600} metric (background OD_{600} from LB blank was subtracted). Each strain was diluted down to .005 OD_{600} into 10 mL LB in a 50 mL Erlenmeyer flask, loosely capped with aluminum foil and put into the desktop incubator shaker for 2 hr to reach log phase. Samples were aliquoted at 500 μL into the sample series. Tubes were labeled for six series at six tubes each. The series were as follows: KSEC, KSEC + kanamycin, KSEC + levofloxacin, KREC, KREC + kanamycin, KREC + levofloxacin. Each series contained six tubes for time points t_0, t_{20}, t_{40}, t_{60}, t_{80}, and t_{100}. Samples were placed in incubator shaker at 37 C, 250 rpm. The samples were dosed with their corresponding antibiotics at their indicated time points. Samples were retrieved 20 minutes after their exposure to antibiotic (exposure duration was kept to a shorter duration to avoid confounding variables).

Once retrieved, the samples were measured for turbidity and ATP. 200 μL were removed and measured for OD600 on a clear 96 well plate as before. The results are shown below (Figure 29).

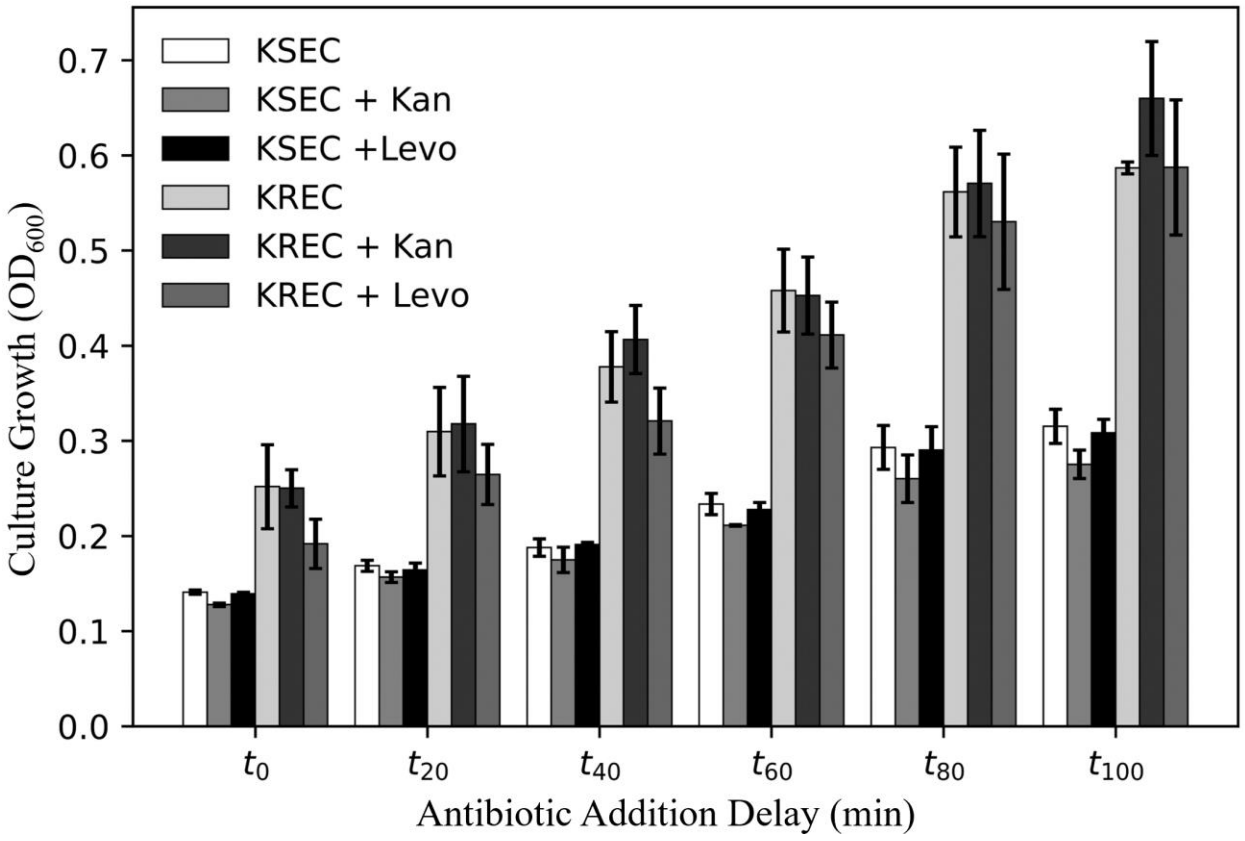

Figure 29. Comparative cell density of cultures challenged with antibiotic at various time lag points.

The KEC series have extremely low variation between treatment conditions at earlier time points. However, as the time points progress, the kanamycin treatment shows a progressively larger loss of cell density as the growth cycle progresses to later stages of log growth.

The remainder of the cultures were spun at 2000*g* for 5 min at room temperature. The supernatant was retrieved and measured on black 96 well plates for luminescence. 100 µL of sample were loaded into wells. 40 µL L/L was added and mixed by trituration using a multichannel pipette. Readings were taken 10 seconds after mixing (Figure 30).

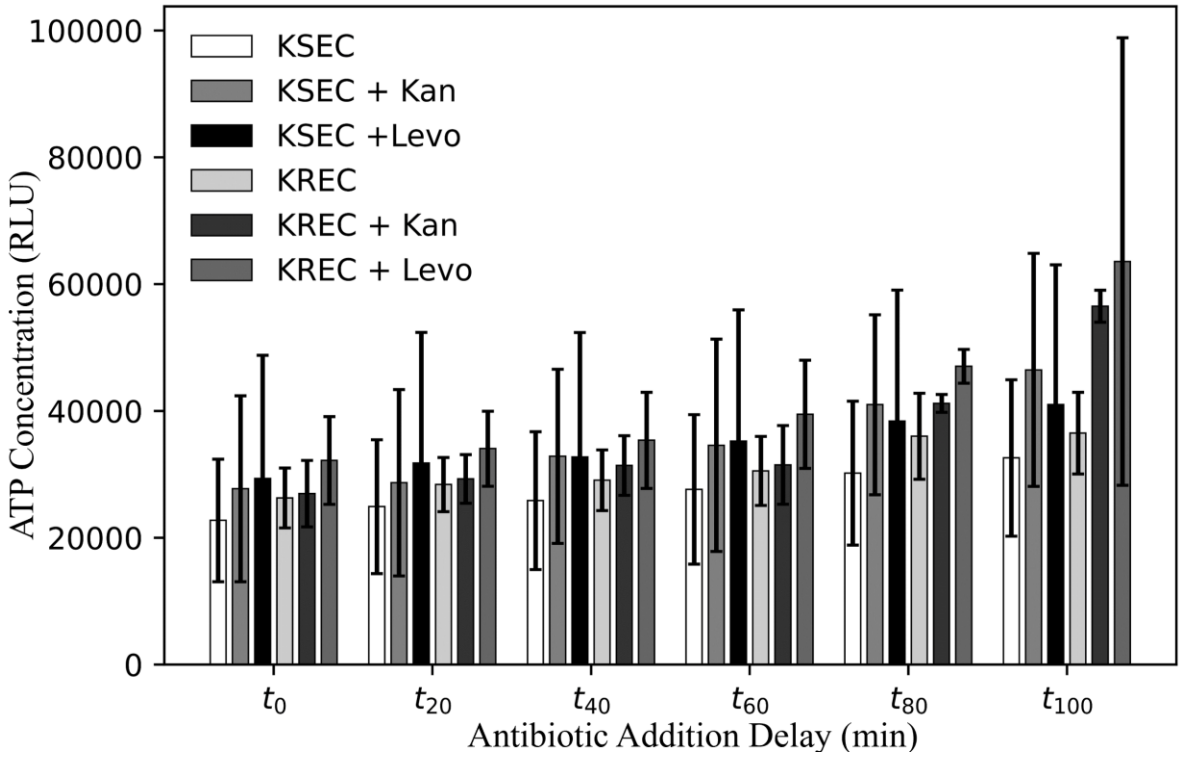

Figure 30. Comparative ATP concentrations of cultures challenged with antibiotic at various lag points.

In the KSEC series, both antibiotics increase the ATP compared to untreated control. Levofloxacin has the greatest increase in earlier time points, whereas kanamycin has a greater effect in later time points. This may potentially be attributed to the differential mechanisms of action acting more effectively depending on the rate of binary division; this explanation would require further experimental verification. In KREC, we see that both antibiotics increase ATP release, but that levofloxacin consistently induces more ATP release than kanamycin. The differential pattern visible between KSEC and KREC should enable an opportunity for discrimination on a PMT detector. The more clearly visualize the effects of the antibiotics, the untreated control sample values were subtracted off from each of the drug-treated samples at each time point. The resulting value indicates the perturbation effect of each drug relative to the untreated condition. The perturbation values were reported for both turbidity and ATP

concentration. The turbidity values are shown below (Figure 31):

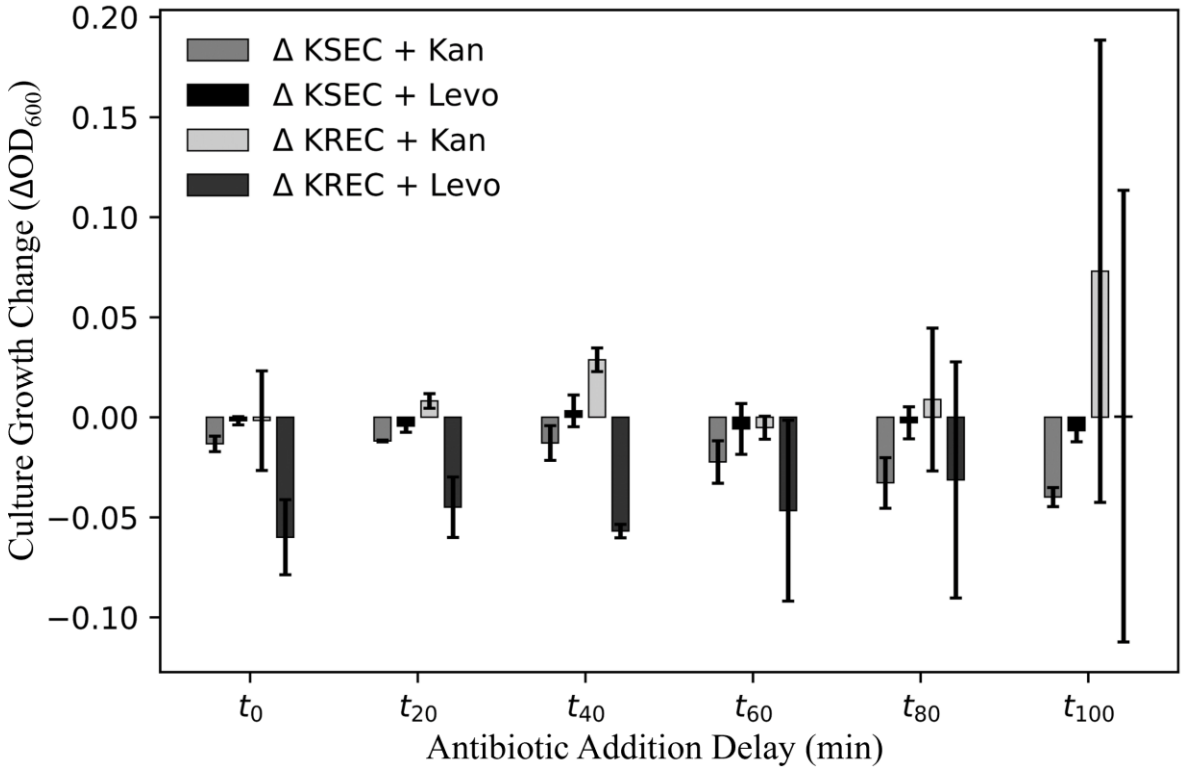

Figure 31. The turbidity signal difference between the treated sample and the corresponding untreated sample (i.e., the perturbation) is shown for each antibiotic at each time point.

This chart makes the pattern clear: Kanamycin has an increasingly severe negative perturbation on KSEC cell density as time progresses, whereas levofloxacin seems to have a very muted effect on the KSEC series. KREC shows a totally different behavior, wherein Kanamycin has local maxima at t40, and levofloxacin has its most significant negative effect at t0. These dramatically differing patterns enable a window of distinction at t40, at which both the difference in magnitudes are maximized and the variability minimized. The turbidity thus suggests that t_{40} is the optimal lag point for addition of antibiotic.

We can similarly investigate the perturbation in ATP levels. The numbers are processed in the same way: The difference between the drug-treated samples and corresponding untreated

controls is calculated. The resulting ATP concentration values are shown below (Figure 32):

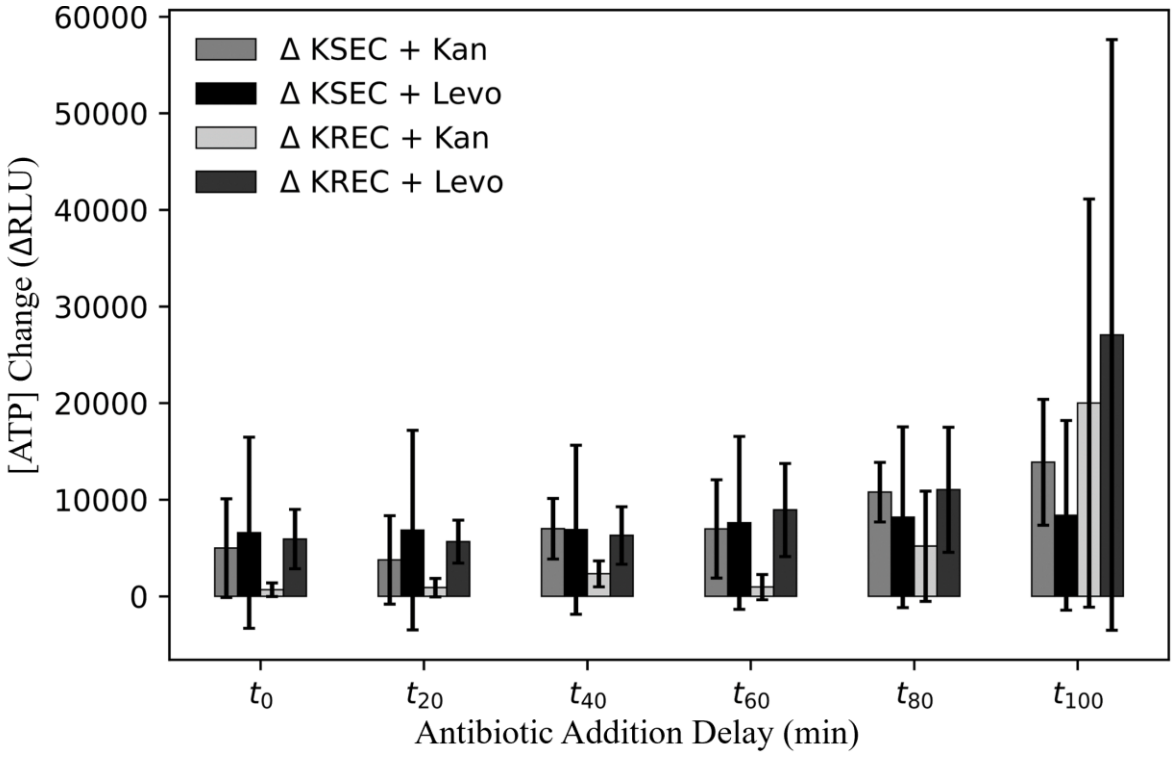

Figure 32. The ATP signal difference between the treated sample and the untreated sample an (i.e., the perturbation) is shown for each antibiotic at each time point.

Again, the patterns of disruption are markedly different between KSEC and KREC. The KSEC series shows an increase in kanamycin samples and simultaneous decrease in levofloxacin samples as time progresses. In contrast, KREC showed a continual pattern where levofloxacin showed higher signal than kanamycin, where the signal for both conditions showed rapid growth over time. This discrepancy in pattern and total signal may again be utilized to discriminate between the two strains. The most reproducible pattern is seen at t_{40}, with the lowest signal to noise ratios. Therefore, t_{40} used as the condition going forward. The cultures will be allowed to incubate for 40 min before the addition of antibiotic.

2.3.4 Optimized Capillary Detection Trials

The desired parameters have been optimized in the previous experiments. The incubation

and lag times which optimally discriminated between the two strains were both found to be 40 minutes. Likewise, the normalized concentrations corresponding to the largest discrepancy was found to be 1x, corresponding to 50μg/mL Kanamycin and 5μg/mL Levofloxacin[36,37]. KSEC (in LB) and KREC (in LB-Kan) cultures were grown overnight at 37 C 250 rpm. At 16 hours, the cultures were measured for turbidity and diluted to a standard .005 OD_{600} in 10 mL LB in 50 mL Erlenmeyer flasks. The flasks were incubated at 37 C 250 rpm for 2 hr to induce cells into log phase growth. The desired parameters have been optimized in the previous experiments. The incubation time of 40 minutes, lag time of 40 minutes, and relative concentration of 1x were utilized for these microcapillary trials.

Six tubes were prepared for the microcapillary trial: KSEC, KSEC + kanamycin, KSEC + levofloxacin, KREC, KREC + kanamycin, and KREC + levofloxacin. The samples were aliquoted at 500 μL, and returned to the incubator for 40 min. The cultures were then treated with 1x concentrations of antibiotic (corresponding to 50 μg/mL of kanamycin and 5 μg/mL of levofloxacin to each corresponding sample). The samples are then returned to the incubator for the 40 min exposure duration. These samples are then retrieved and centrifuged at 2000*g* for 5 min. The supernatant is collected from the cell pellets for use on the microcapillary system.

The system is turned on with the PMT at 700mV and the amplifier set to a gain of 10^9. The data logger is linked to a local computer running the LabVIEW 'Voltage Continuous Input' program at 1000 Hz. The sample and L/L reporter are loaded into 2 syringes and coupled into the syringe pump set to 6000 μL/hr. External lights are shut off to reduce noise and the system is run without recording for 30 sec to allow the lines to equilibrate. Data is then taken until the pumps are exhausted. The arrive at the voltage value for a sample, a simple average was taken of the voltage trace file. To process the data, the untreated strain is treated as baseline and subtracted off

the antibiotic-treated sample values. Experiment was run in triplicate. To account for inter-run variability, sets of data were normalized so that the largest value in the set was assigned a value of one, and the other values were divided by that value. Each value is itself an average of at least 20,000 equilibrium data points. The samples were then averaged, and the error was reported as +/- 1 standard error. The results are shown below (Figure 33).

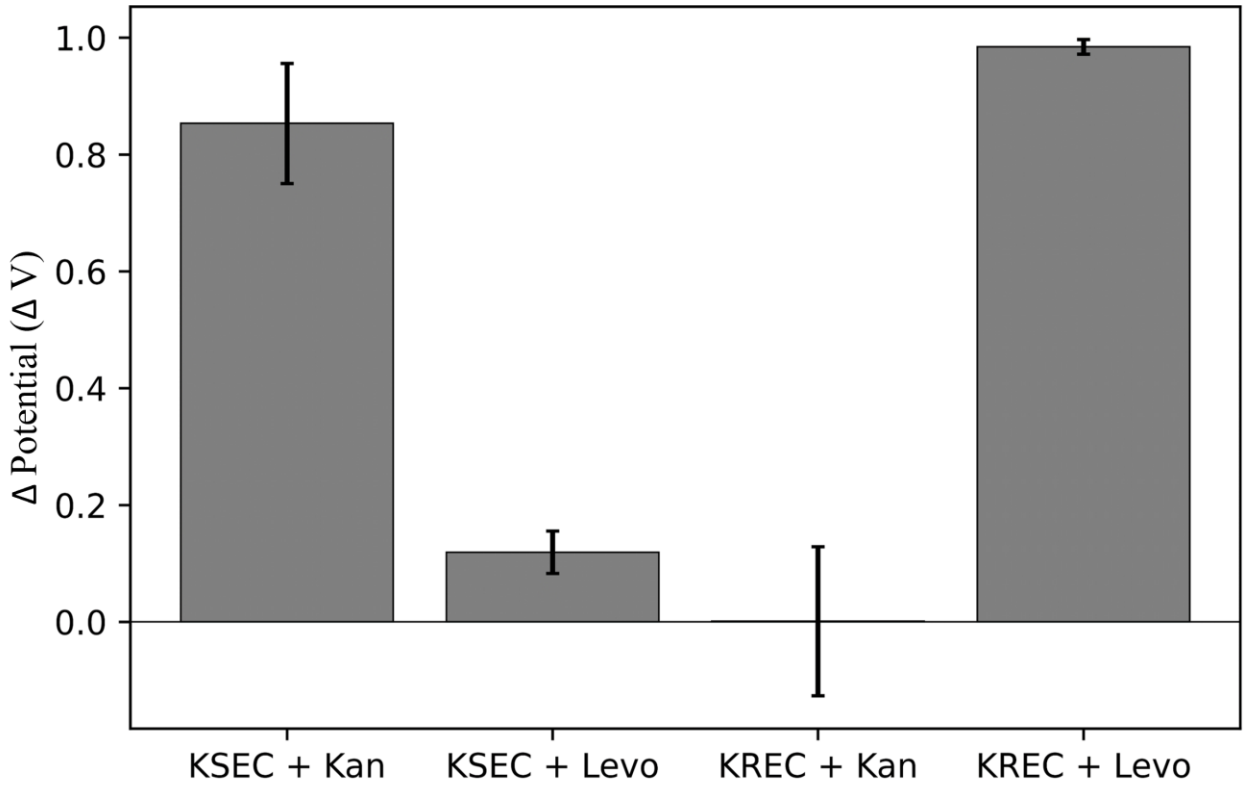

Figure 33. The antibiotic-induced voltage perturbation of each strain compared to untreated baseline. An inverse pattern is seen between the strains. One way ANOVA analysis returns p=0.0003, indicated a robust and statistically significant discrimination between the two strains.

The voltage patterns for the two strains are inverted relative to each other, which kanamycin inducing an increase in KSEC and levofloxacin inducing an increase in KREC. This pattern appears to be robust and statistically significant. This data verifies the capacity of the system to discriminate between resistant and sensitive strains in a reproducible fashion.

Despite the success of the microcapillary system, the system had drawbacks that are

inherent to detecting a continuous aqueous phase. For example, the system suffered a signal loss due to the diffusion of the ATP into the larger continuous volume. Also, the system could make no distinction between cells in a continuous phase, and the ability to sort or genetically analyze cells based on phenotype was not possible. Both problems could be addressed be discretization: ATP concentration per cell can be increased by confining it to a smaller local volume, and cells that lyse (or those that remain intact) can be sorted individually if they are in a discrete, local aqueous volume. Therefore, droplet microfluidics was utilized to improve the system.

CHAPTER 3: DROPLET-GENERATING CHIP DEVELOPMENT FOR INTEGRATION INTO CAPILLARY SYSTEM

3.1 Pilot Design

There are multiple advantages to utilizing the microcapillary platform as described in chapter 2. It is possible to analyze multiple samples in parallel, merely by including more lines and PMT transducers. This will enable an unlimited number of samples and challenge antibiotics, potentially side-stepping laboratory bottlenecks. The internal volume for the detection window is just 1cm long with an ID of 72 μm range, corresponding to a volume of 32 nL. Because each bacteria contains roughly 5 mM ATP internally, and even smaller microbes such as *E. Coli* contain approximately 1-2 cubic μm, it would only require cell numbers in the hundreds to generate the required nanomolar concentrations to routinely detect their ATP signatures on a PMT module[2838]. Certain techniques, such as cooling the equipment down to extremely low temperatures, can increase the sensitivity such that PMTs can detect single photons. As such this setup has the potential to completely obviate the need for the slow, rate-limiting culture-based sensitivity screens (such as the microdilution broth assay or the Kirby Bauer test) and report antibiotic sensitivity profiles in minutes instead of the industry standard of 3-7 days. This promise has the potential to make lab-informed narrow spectrum prescription truly point-of-care, in which a patient's infectious disease is screened during their appointment and initial prescriptions are a narrow-spectrum targeted approach based on the results of the lab findings. The opportunity to move beyond escalation/ de-escalation triage and accurately target infections to avoid the risk of sepsis and shock are enormous in terms of lives and financial resources. The system has other practical benefits; the modularity and relative cheap components allow the lines to be autoclaved and disposed following the run, keeping the pathogen contained and reducing the risk of healthcare associated infection.

However, there are still theoretical improvements that can be made to advance the rapid-screening goals of the system. For example, the current design supports a continuous fluid-phase cell suspension as an analyte. This means that, as with many assays, the result is a composite average of the cell responses and loses the single-cell resolution that may detect minority behaviors or intra-sample variations. Additionally, a continuous aqueous sample dilutes the ATP signal in the flow stream, lowering the concentration of the analyte and therefore introducing signal loss into the system.

The method that best suited to solving these problems is the subfield of droplet microfluidics, previously discussed in chapter 1. Briefly reviewed, the aqueous sample is fed in through on channel, and an immiscible carrier phase is fed into another channel. The two phases will be mixed to generate aqueous droplets which will be carried through the channels by the carrier phase. Frequently a detergent or surfactant is used to stabilize the interface the droplets to prevent splitting, coalescing, or adherence to the channel walls.

The advantage to this system is two-fold: signal enhancement and discretization. Because a single cell may be isolated to a nanoliter-scale droplet, the ATP analyte will be confined to a smaller volume when released from the cell. The more concentrated ATP will generate a stronger signal and be more clearly distinguished by the PMT detectors (Figure 34):

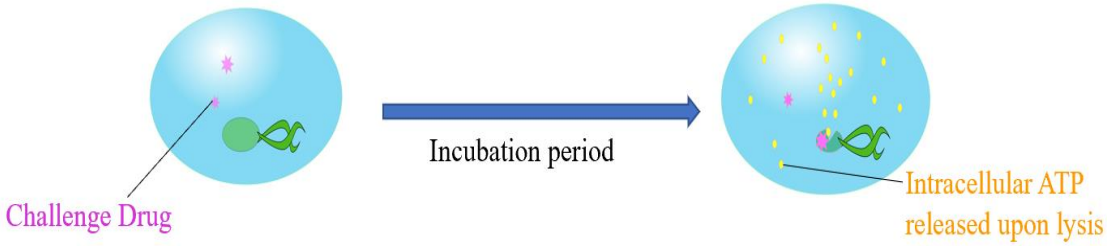

Figure 34. The droplets generated in a droplet microfluidic generator may stochastically trap cells at random. Given a dilute cell suspension, it will be possible to nearly perfectly isolate single cells per droplet. Upon purinergic signaling or lysis, the released ATP will rapidly increase the ATP concentration within the droplet and enable a robust chemiluminescent signal.

The second advantage, discretization, enables compartmentalization each cell in the sample into the functional equivalent of a small-volume, single-cell beaker. Droplets captured in these physically and chemically isolated 'nanoreactor' droplets may be treated as individual samples and measured, isolated, and processed separately from the rest of the droplets. This approach would be impossible in a continuous phase, diffusion-based cell suspension. A prerequisite for this approach is the notion that the cells may be isolated singularly into their own droplets. Unfortunately, particle capture in droplets is a random, stochastic process, and therefore we must leverage statistical tools to guarantee that any one droplet contains at most one cell. The statistical tool that models our situation best is the Poissonian model (Figure 35).

$$P_X(k) = \frac{e^{-\lambda} * \lambda^k}{k!}$$

Figure 35. The Poisson Distribution equation. This equation describes the likelihood that a random discrete, rare independent event with an underlying likelihood will occur in each window of opportunity. This equation represents the likelihood that the underlying random variable P_x will take on the specific realization value k. The average likelihood or expected value is represented by λ.

The Poissonian model elegantly describes the droplet capture problem. The discrete distribution is meant to capture the probability that a rare, independent, randomly occurring event with a constant underlying probability will occur a given number of times within a given window of opportunity. If we take droplet capture of a cell to be our independent event (a justified assumption, given a low cell concentration), the underlying probability to be the cell density in the source suspension compared to the droplet volume, and the window of opportunity to be the droplet volume, we can calculate the proportion of droplets that will contain 0, 1, 2 or

more cells from a given cell suspension. Consider a solution where there is, on average, one cell per ten droplet volumes. This gives us λ = 0.1. Let us calculate the probability that the droplet will either contain 0 or 2 droplets. That equates to Px(0) + Px(1) and turns out to equal 0.9953. That indicates that there is a 0.0047 chance that a droplet will contain multiple cells. This vanishingly small chance enables us to approximate very a binary droplet population that is either unoccupied or singly occupied. This assumption allows us to treat each occupied droplet as a single cell member of a group, rather than part of continuous fluid average.

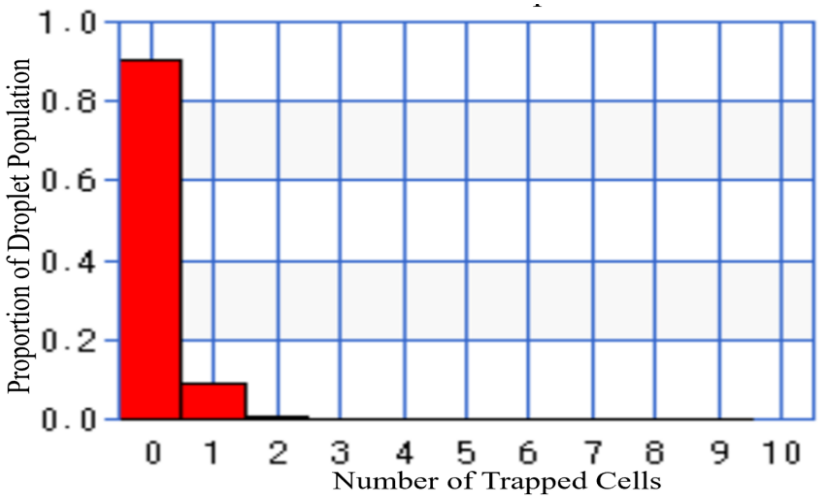

Figure 36. The Poissonian distribution given λ = 0.1 condition. This indicates that if there is, on average, 1 cell per 10 droplet volumes in the main solution, the probability of a droplet containing more than a single cell is 0.0047. This will allow cell-sorting and direct cell-to-cell comparisons and counting.

Discretization allows a very specific advantage in this use case. Droplet containing cells can be grouped by various methods into positive or negative for sensitivity.

Physically fabricating the channels on a polyjet printer is an engineering challenge: Channels cannot support their own weight and must use support material to be printed, yet any the channels are too small to permit the mechanical removal of any solid support material. Fortunately, earlier work in the Spence lab has established the 'print-pause-print' method which utilizes the use of high-viscosity liquid support to produce channels (Figure 37)[39]. The technique

requires printing of the channel layer, which contains the geometry which defines the functionality of the fluidics. The negative space of the channel is then flooded with a 70% Glycerol-EtOH solution (v/v) to prevent flooding of the channel space from the deposition of the upper layers. The print stage is then dropped corresponding to the height of the print. Then, the 'top plate' layer is printed to seal the channels, including any injection ports or effluent spaces. Finally, negative pressure is used to evacuate the glycerol solution from the channels to liberate the negative space. The channels must be repeatedly washed with water to clear residual glycerol from the device. Utilization of this technique enable fabrication of channels down to the resolution of the printer. The nominal resolution of our platform (Stratasys J750) is 27 μm square in the X-Y plane. So far, channels down to 250 μm diameter have been routinely reproduced. The resin used going forward is Veroclear, a methacrylate resin useful due to its optical clarity.

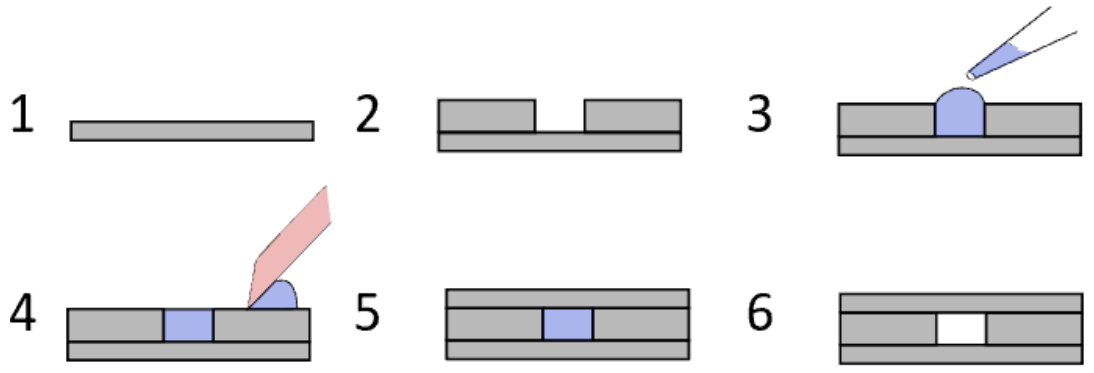

Figure 37. The 'print-pause-print' method involved laying down a channel layer, adding supportive glycerol-ethanol to the negative space, and lay down a sealing plate on top of it. Vacuum can then be used to clear the channels.

To characterize droplet behavior on this polyjet Veroclear platform, a 'T-junction' pilot chip was tested for droplet generation with 250 μm square channels (Figure 38). The chip is designed to facilitate mixing of two aqueous components, mixing and homogenization of the aqueous mixture, and subsequent emulsification of the aqueous phase into discrete droplets by the carrier

phase. Here the carrier phase used is NOVEC HFE 7500, a common hydrophobic carrier phase. Surfactant (S008, Ran Biotechnologies) will be mixed into the NOVEC at 2% w/w.

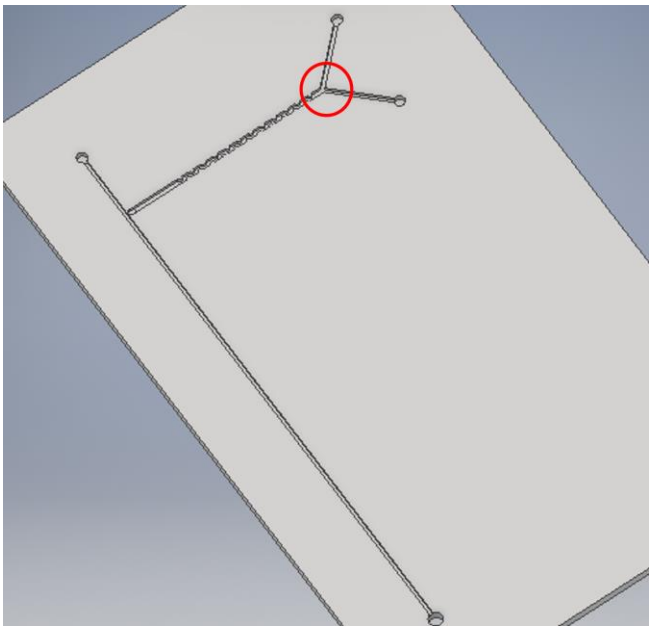

Figure 38. The pilot T-junction chip. The 2 ports on the top right are aqueous inputs. These channels merge and feed into a sinusoidal mixing element, enabling the mixing of two aqueous components before segmentation into droplets. The port at the top left is the carrier phase input. The aqueous channel and carrier channel meet at the T, using shear force to tear aqueous droplets from the bulk.

3.2 Surface Processing and Performance Evaluation

Chips directly off the printer suffer from certain setbacks. Pertinently, these chips are not sufficiently clear to be coupled with optical microscopy. The post-print finish does not import enough optical clarity to the surface to permit high-resolution microscopy of the channels underneath. Therefore, the chips require surface finishing to render the external faces of the chip as smooth as possible. Fortunately, a brief treatment with finishing sandpaper was sufficient to remove roughness and imperfections from the surface. Here, finishing sandpaper (Lanhu, High precision) is used to sand the surface of the chip, progressing through grit from 1,500 to 2,000, 2,500, 3,000, 5,000, and finally 7,000. The treatment rendered the surface optically transparent.

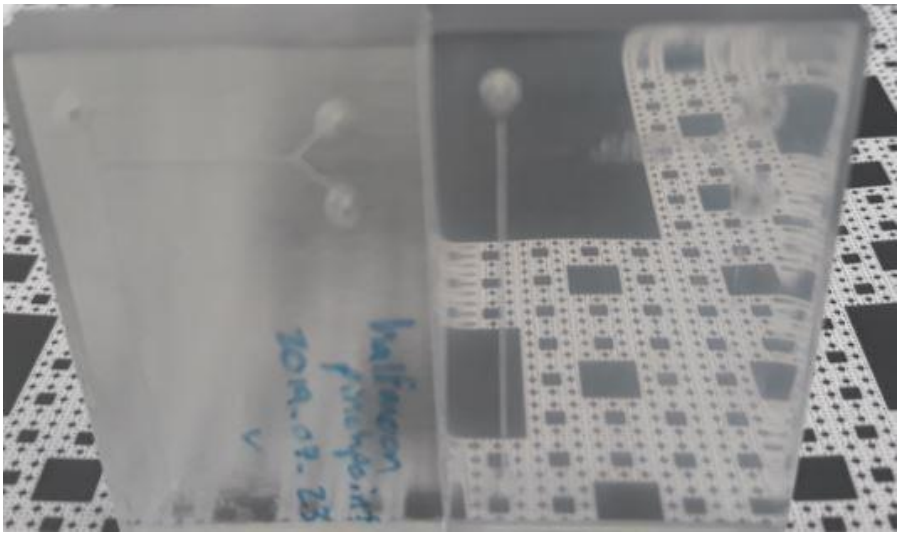

Figure 39. Comparison between unpolished (left) and polished (right) Veroclear fluidic chips over a fractal background.

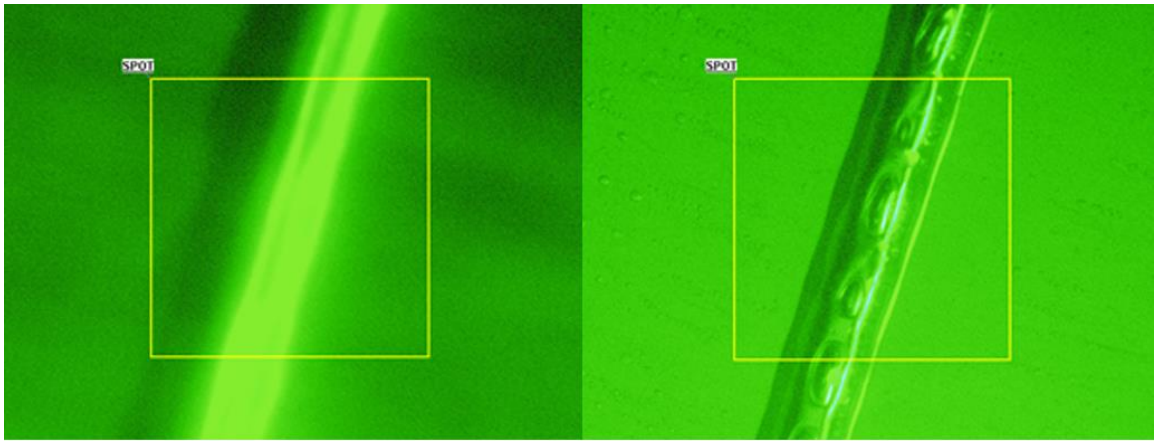

Figure 40. C Channels observed under FITC channel through a 2x objective microscope. Imperfections in the channel become visible after surface sanding treatment.

To quantify this increase in optical clarity, the chip was measured for light transmittance directly after printing, then again after surface sanding. The chip was loaded into a spectrophotometer and measured for OD_{600} as a measure of clarity (pre-polish condition). Then, the chip was polished according to the above protocol and measured again by spectrophotometer in the same manner (post-polish condition). Unsurprisingly, the polished condition returned a

reproducibly lower optical density that the unpolished condition, corresponding to an increase in clarity (Figure 41).

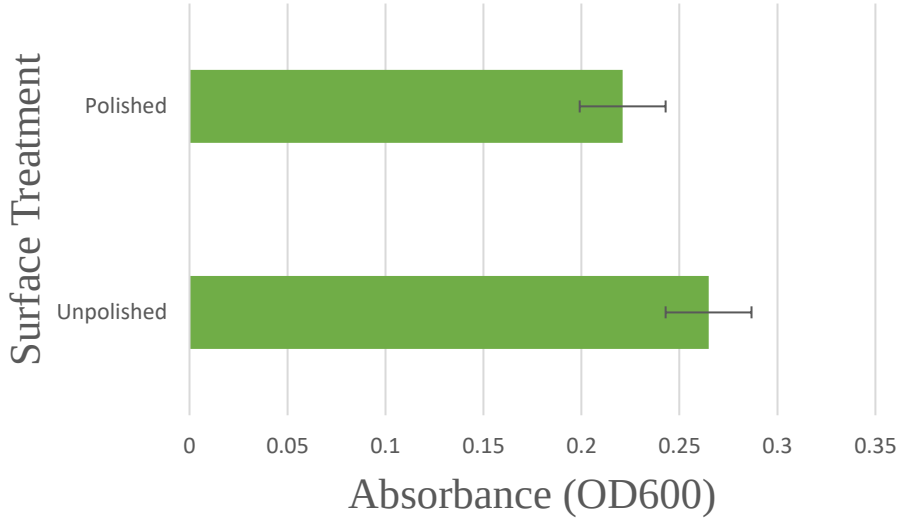

Figure 41. Surface polishing results in a loss of optical density at 500nm. This equates to an increase in transparency/ optical clarity.

The aqueous phase was a solution of fluorescein (0.1mg/mL) which excites under blue light (495 nm) and emits green (519 nm). The immiscible carrier phase was NOVEC HFE 7500, an extremely hydrophobic perfluorinated ether that is commonly used in droplet microfluidics as the carrier[40]. To stabilize droplets, a surfactant S008 (Ran Biotechnologies) was used to stabilize the interface between aqueous and organic phase. The chip was printed with rubber-like 'Agilus' injection ports for insert of the fluidic line leads. Tygon tubing was coupled to both the chip and the injection syringes (Hamilton Gastight 1750 series, 500 µL). One syringe was filled with a NOVEC/ S008 mixture where the surfactant was 2% w/w. The other syringe was filled with the fluorescein solution. The two syringes were coupled to separate high-precision syringe pumps (Harvard Apparatus 11 Plus). Chip behavior was observed on an Olympus inverted microscope through a FITC filter and 2x objective, and runs were recorded in video .avi format. Setting the carrier pump to drive at 300 µL/hr and the aqueous phase to run at 90 µL/hr produced the

following behavior:

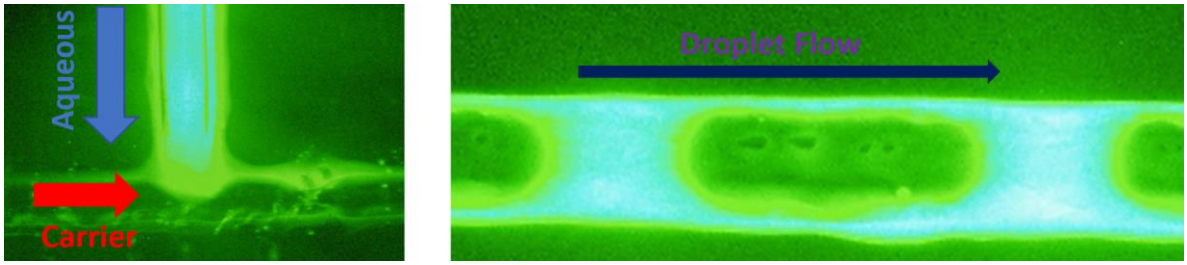

Figure 42. The T-junction pilot chip in Veroclear. Fluorescein pilot experiment successfully segmented droplets. The walls have affinity for the aqueous phase due to the concave nature of the droplet interface. This observation called for further inquiry.

Ideally, the droplet generation rate should be tunable for so that it can be optimized for the application at hand. For this system, the droplet generation rate may be controlled by adjusting the aqueous pump rate. To quantify the relationship between aqueous rate and droplet generation rate, the pump was varied from 60 to 300 µL/hr, and droplets per second were determined by analysis of the .avi video files (Figure 43). The droplet generation rate is surprisingly controllable as a function of pump settings, with a Pearson R-squared value of 0.9827.

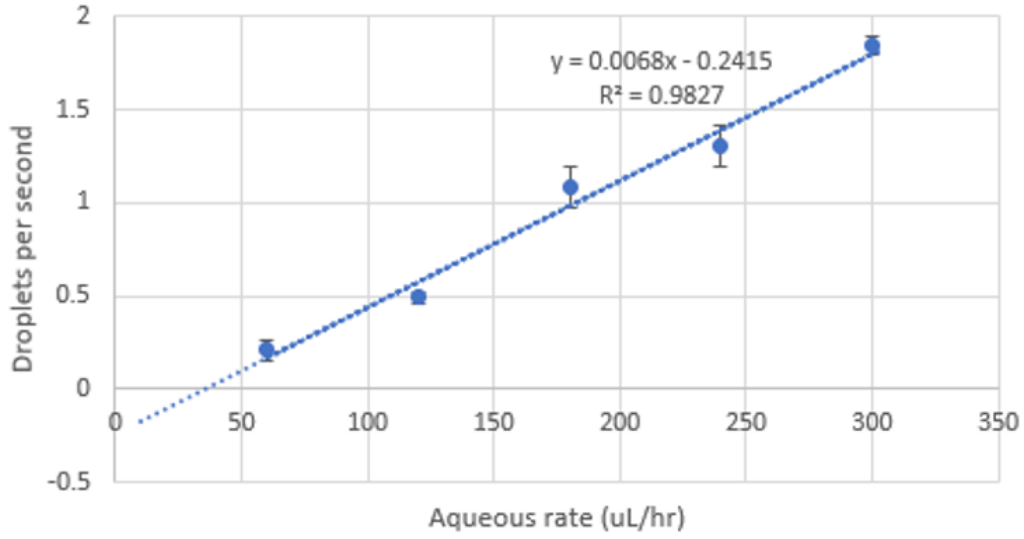

Figure 43. Droplet generation rate tunability as a function of aqueous pump rate setting. The generation rate is highly tunable, linearly increasing with pump rate.

While qualitatively the chip appears to behave successfully, it is important to quantitatively evaluate the droplet behavior. To evaluate these videos with precision, MATLAB code was developed to extract data from the image stack. Briefly, the code identifies the channel on the images, draws a midsection line that traverses the center of the channel, and evaluates changes in pixel intensity patterns form frame to frame. This allows the program to identify droplets and track their traversal down the channel. Finally, the program can catalog droplet volumes and the temporal spacing between the droplets. The final output are histograms showing the distributions of the parameters of interest.

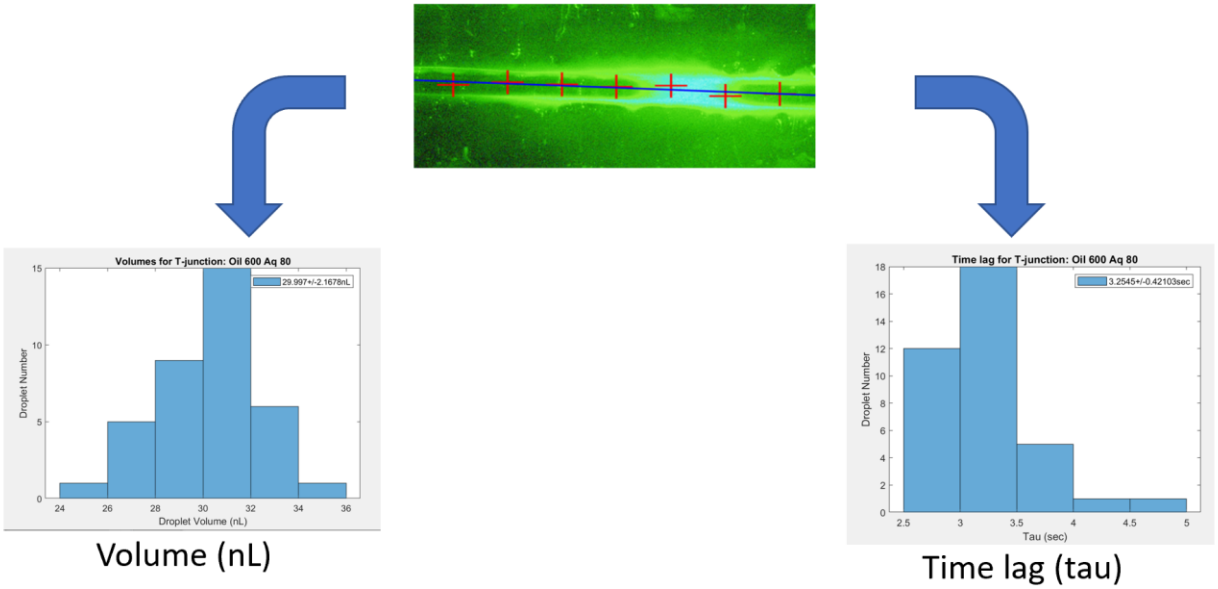

Figure 44. Above is the channel projection MATLAB assigned to the video to monitor for signs of fluorescence. On the left is the droplet volume output in histogram format and on the right is the histogram of time lag between droplets.

Unfortunately, neither the droplet volumes nor the temporal spacing between them in the channel was adequately predictable in this pilot chip. The volume itself ranged from approximately 24-36nL (a 33% variation). Additionally, there is room for improvement on the average droplet volume. The 24nL average is on the higher end of fluidic droplet volumes.

Future versions of the chip should be designed with a reduced volume in mind.

Now that droplets have been produced on a pilot chip, it will be required to confirm that it is possible to detect ATP utilizing the luciferase assay on these devices. The chip should be able not only to detect ATP via the chemiluminescent assay, but to acquire a discrete signal from each droplet and discriminate any given droplet signal from its neighbors. Initial experiments suggested that light scattering in clear chips interfered with the production of resolving individual droplets by luminescent signal (due most likely to internal light scattering). Hence, it was necessary to design a fluidic device that screened internal light scattering and only permitted escape of light at a region of detection next to the PMT detector. This approach should reduce noise and allow the signal from each discrete droplet to resolve from adjacent droplets. A 'dark chip' printed in the opaque 'Veroblack' resin was printed with a small optical detection window, measuring 2 mm on each side, allowing transparency for at only the droplets currently traversing the window (Figure 45):

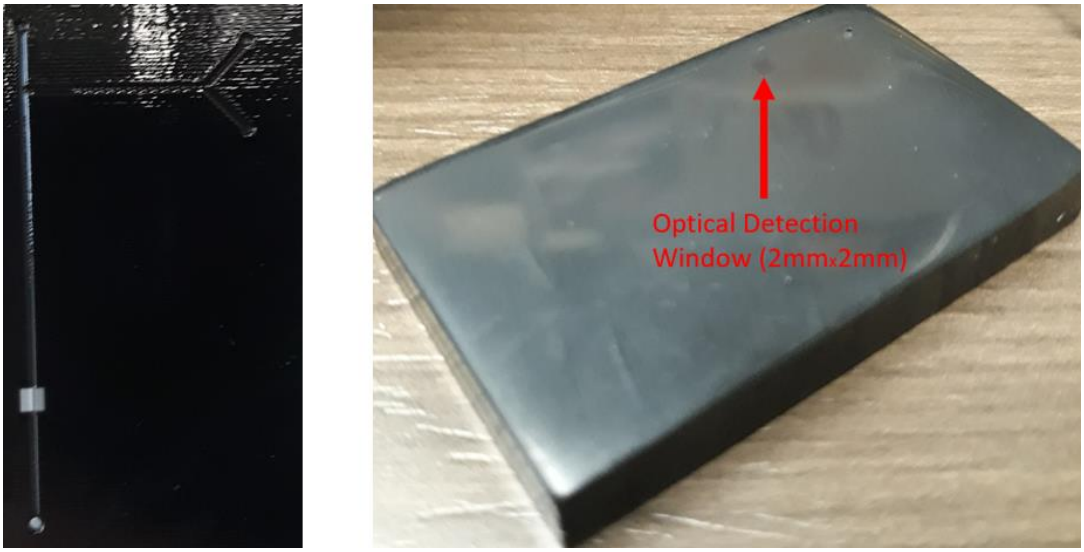

Figure 45. A Veroblack proof-of-concept chip. The left panel shows the T-junction channel design and the imbedded detection region along the downstream section of the channel. The right panel shows the completed chip with the polished detection well visible on the surface. The black resin should assist in screening internal light scattering and hench help eliminate noise from the data.

The chip was placed in a darkbox lined with aluminum foil to exclude ambient light. The detection window was positioned directly over a PMT detector module. Two syringes were used for aqueous phase inputs: 1 aqueous phase syringe was loaded with an 80 μm ATP solution, and the second aqueous phase syringe was loaded with L/L reporter. A negative control will be included as a 0 μm ATP solution, which is essentially water. An additional syringe was used for the carrier phase and was loaded with NOVEC with 2% S008 surfactant w/w. The two aqueous syringes were hooked up to the same syringe pump. The carrier phase syringe pump was hooked up to a second syringe pump. The fluidic lines (Tygon tubing) were coupled from the aqueous syringes into the darkbox and onto the aqueous ports. The carrier line (Tygon tubing) was coupled from the carrier syringe into the darkbox and onto the carrier phase chip port. To further screen an ambient light, an opaque cover was set over the chip. The PMT was connected to an external Data Acquisition (DAQ) device or 'data logger' and fed into a local laptop running the 'Continuous Voltage Input' LabVIEW program to collect data.

When running the experiment, lab light was shut off to reduce ambient noise. The trans-PMT voltage was set to 750 mV. The carrier pump was set to 600 μL/hr. The aqueous pump was set variably to verify that the droplet rate would rise or fall corresponding to the aqueous input rate. The aqueous rates tested for this experiment are: 60 μL/hr, 80 μL/hr, and 106 μL/hr. If the droplets are successfully detected, it would be expected to appear in the output trace as a spike increase in voltage. The 'sharper' the peak is, i.e., the lower the 'full width half max' value, would correspond to a greater signal-to-noise strength. Faster aqueous rates are expected to generate droplets at a faster rate and therefore correspond to more densely packed voltage spikes. The results of the experiment are shown below (Figure 46):

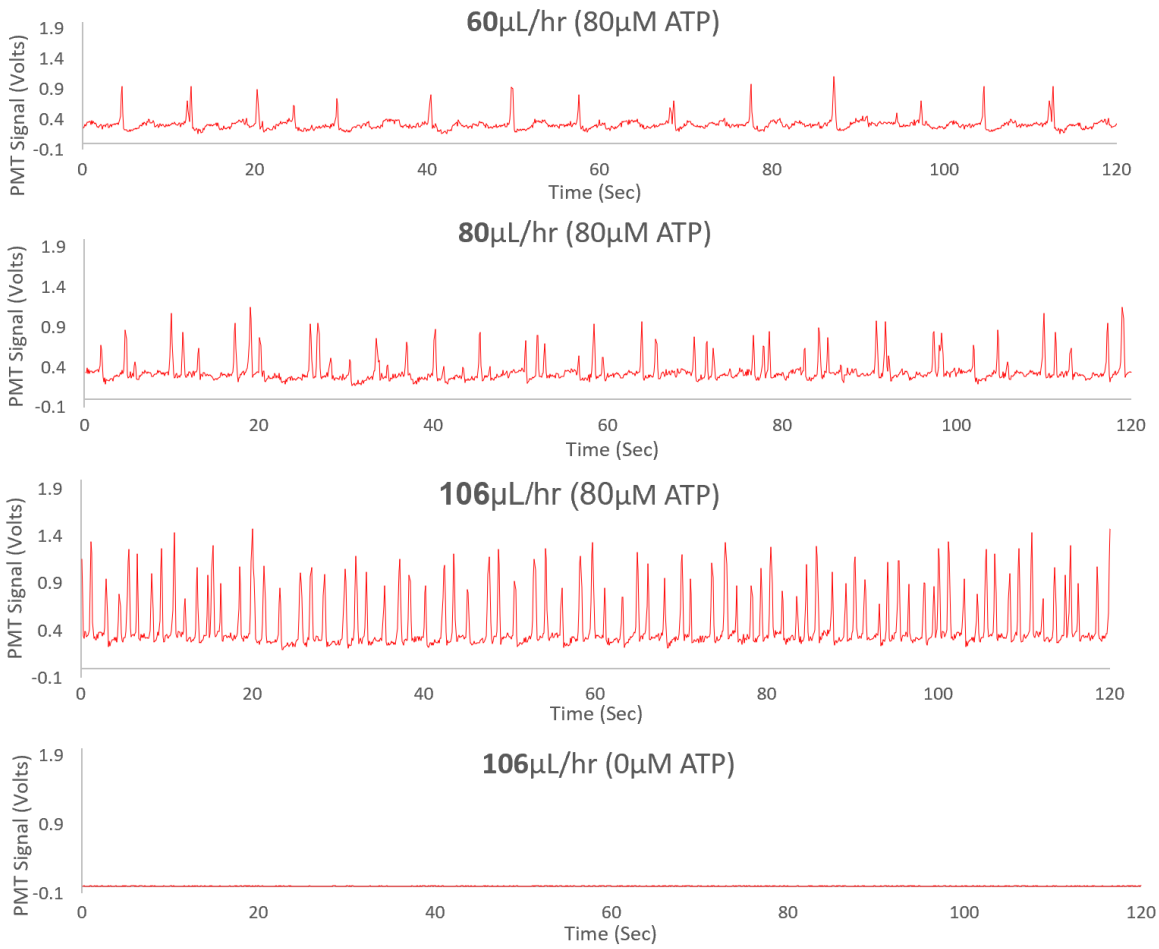

Figure 46. (A) Luminescent ATP droplet detection as a function of aqueous pump rate. Droplet detection becomes more frequent as the aqueous pumps are set to higher rates. The 0 concentration of ATP results in no detection as expected.

The results are as expected. The droplet rates (droplets per second or DPS) increase as aqueous pump rates are set higher. The 0 µm ATP produces no signal in response to L/L and therefore generates no luminescence and no signal spike, as expected. Finally, the signal is well defined with a 'decibel' value of 8.4, corresponding to a signal-to-noise (S/N) ratio of 6.9. This is compelling evidence that ATP can be successfully detected with L/L on the Veroclear chips on the darkbox platform.

3.3 Hydrophobicity Treatment and Channel Geometry Candidates

While these proof-of-concept experiments were encouraging. The fluorescein experiments

elucidated a fundamental problem with the printed chip: The aqueous phase demonstrated affinity for the cell walls. This is in direct contrast with the PDMS casted chips, where the walls are extremely hydrophobic and help stabilize the formed droplets. If the channels walls have affinity for the aqueous phase, the droplets may smear, break apart, coalesce, or exhibit out forms of unstable stochastic behavior[41]. The surface of the channels must therefore be treated to improve the hydrophobicity. We can evaluate the success of our treatment by the 'Young Equation' (Figure 47)[42]. The contact angle 'θ' depends on the 3 forces that dominate the surface interaction (liquid-liquid affinity, liquid-fluid affinity, and liquid-solid affinity). If the liquid-solid affinity dominates, θ will be small and the liquid will flatten out and 'wet' the surface. If the liquid-liquid affinity dominates (corresponding to a high surface tension) θ will be high and the liquid will 'bead' away from the surface as the system energy tries to minimize. If we are successful in increasing the hydrophobicity of the channel, we will see visual indicators of an increase in θ.

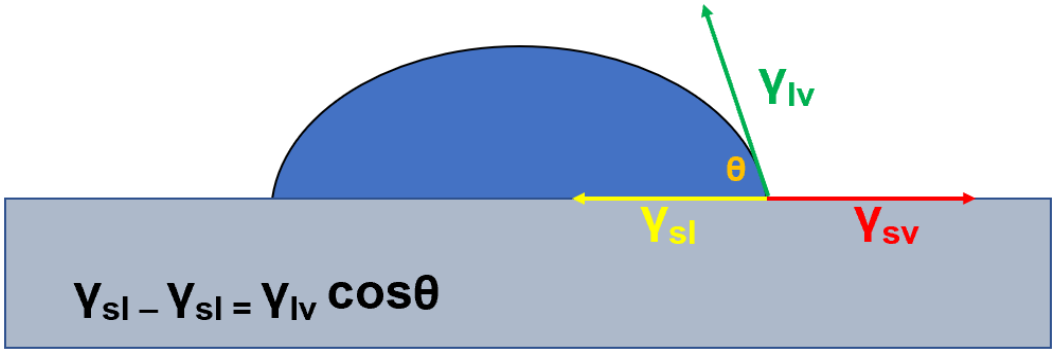

Figure 47. (A) The Young Equation. The contact angle θ will increase (the liquid become more spherical) as the channel surface hydrophobicity increases, due to the decrease in the liquid-solid affinity stretch force.

To increase the hydrophobic nature of the channel, the channel may simply be flushed with a commercially available PDMS solution to allow adherence to the walls. Specifically. The channels will be flooded with PDMS solution, which will be allowed to remain in the channels

for 30 minutes. The excess solution will then be gently dripped out, and the liquid remaining in the channels will be allowed 1hr to dry. The flooding, draining, and drying procedure was repeated a second time to allow the maximum amount of PDMS to adhere to the channel walls and solidify as possible, maximizing the chances the channel properties will behave as a PDMS cast chip. Microscopic observations were taken on the channels before and after PDMS treatment (Figure 48).

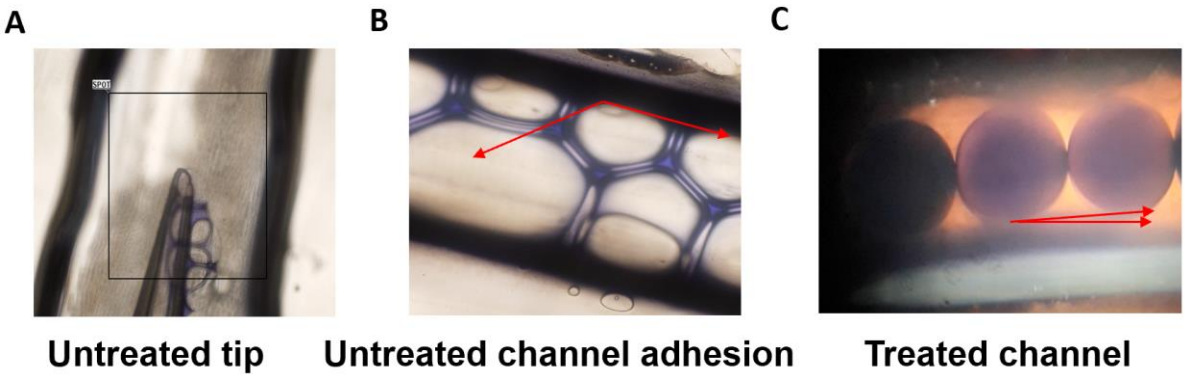

Figure 48. (A) Untreated borosilicate tips attract the aqueous phase and do not permit droplet formation (B) Untreated Veroclear preferentially interacts with the aqueous phase over the carrier phase. (C) PDMS-treated Veroclear shows an increase in θ, with perfectly spherical droplets forming along the channel. This signals that the PDMS successfully imparts hydrophobicity to the channel.

To Panels A and B above show the effects of borosilicate (sometimes used as an injection mechanism in fluidic chips) and Veroclear before PDMS treatment. In panel B we see that the water is adhering to the walls as closely as possible despite being the minority constituent, and carrier phase itself forming droplets in a situation known as 'inverse emulsion'[43]. Panel C, Veroclear after PDMS treatment, shows the exact opposite behavior. The carrier phase is appropriately sequestered around the channel walls and the aqueous droplets are forming stable droplets with very little contact surface area with the channel walls. We can conclude that the PDMS treatment was a success and use it in all droplet experiments going forward.

With chip surface and channel treatments addressed, it is necessary to identify the channel

geometry that most effectively produced the droplet population that is advantageous to cell-based applications. The desired properties are: minimized volume to increase analyte concentration, rapid production to increase capacity for high through-put experiments, and droplet volume monodispersity to allow cross-cell comparison. The geometry that permits the droplet population that most closely meets these requirements will be selected for future experiments.

There are three common droplet-generating geometries reported in the literature: T-junction, flow-focus, and co-flow geometries (Figure 49)[44].

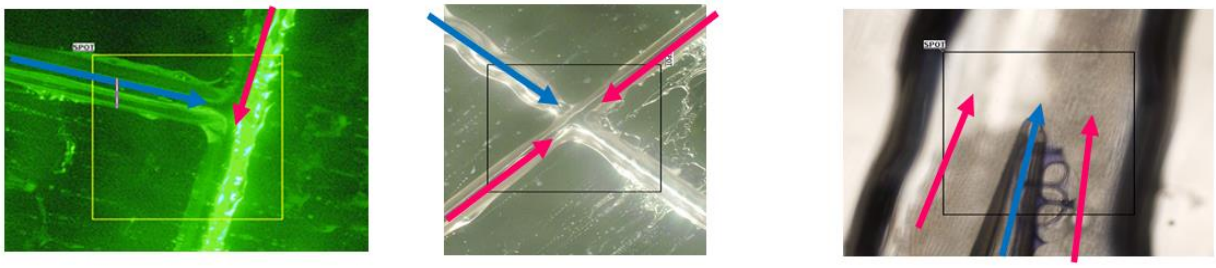

Figure 49. (A) T-junction droplet generator (B) Flow-focus generator (C) Co-flow generator. The blue arrows represent aqueous flow, and the red lines indicate carrier phase/ organic flow. Droplet generation occur at the intersection of the two flow phases.

All three were printed in Veroclear, surface-polished, and PDMS treated. The three candidates were tested for their ability to produce adequate droplet profiles. It proved difficult to product droplets below a certain volume threshold (~30nL) using the T-junction. Additionally, the droplet-per-second read is suboptimal for running a high-throughput experiment on hundreds of cells. Therefore, the T-junction geometry was not selected for future experiments. The co-flow geometry roved unpredictable in droplet production rate, volume, and behavior while using either the two common modalities (‘dripping’ or ‘jetting)[45]. The co-flow chip was discarded, as its unpredictable performance limited its utility as a point-of-care clinical tool.

The flow-focus design was found in preliminary tests to meet all criteria: it was able to quickly generate small, monodisperse droplets. The CAD for the flow-focus design selected is

shown below (Figure 50). There are two aqueous ports at the top that merge into a mixing element which will allow us to mix two components as before. The two ports below are the carrier/ organic phase inputs. Briefly, the carrier phase channels flow perpendicular to the aqueous phase channel and pinch the aqueous phase into droplets using shear force. The droplets are then released into the larger, low-pressure downstream channel. Because the downstream channel is larger in diameter and depth, the flow rate of the droplets is slower, allowing any time for any chemical reactions to develop here- and therefore is referred it is referred to as the incubation channel. The droplets eventually flow out of the incubation channel and are pushed through the effluent tip at the base of the chip.

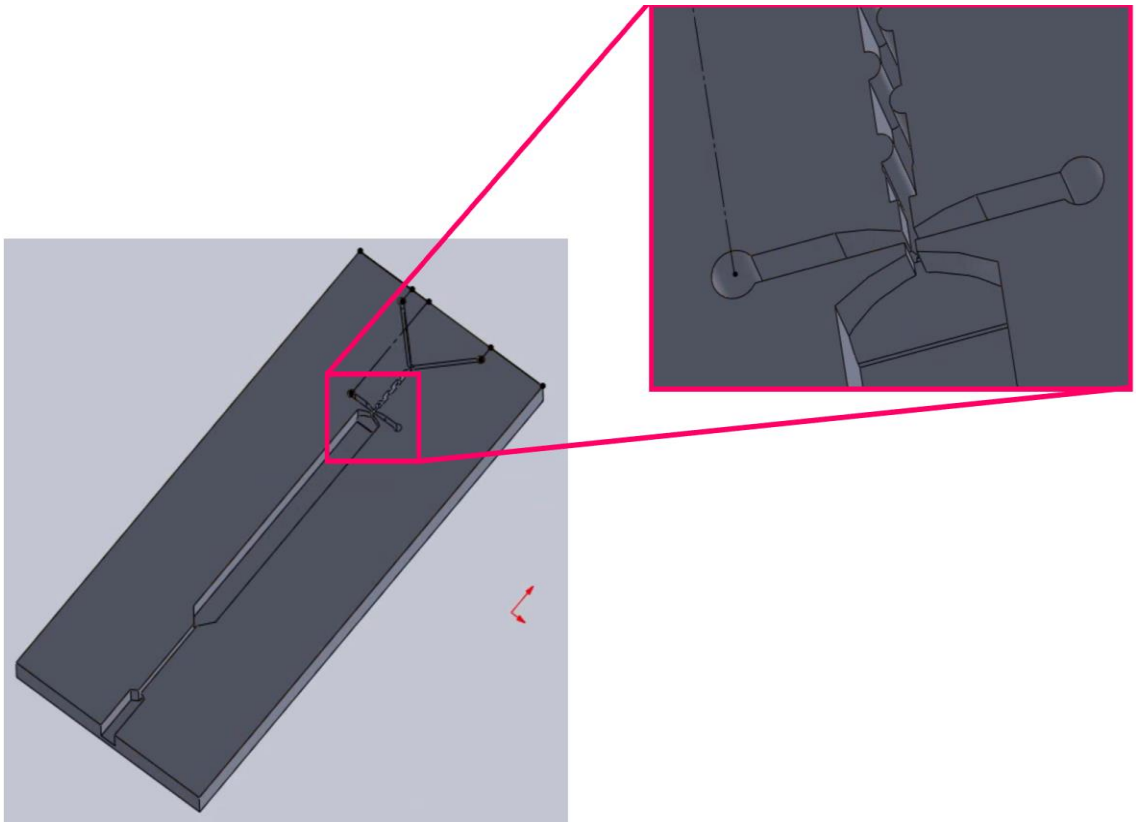

Figure 50. Chosen flow-focuser chip design. The ports at the top of the chip allow for aqueous injection. The aqueous ports may then be homogenized at the mixing element below, the segmented the carrier phase, which is supplied in a perpendicular flow supplied at the two lower injection ports. Droplets are fed into the wider incubation chamber before passing through the effluent tip.

The overall fabrication steps involve printing the base layer, gluing in the effluent tip with epoxy, forming the channels using the print-pause-print method, surfacing polishing, and channel treatment with PDMS. Lastly, epoxy must be applied around the edges of the effluent tip to avoid leaks. The final product is shown below:

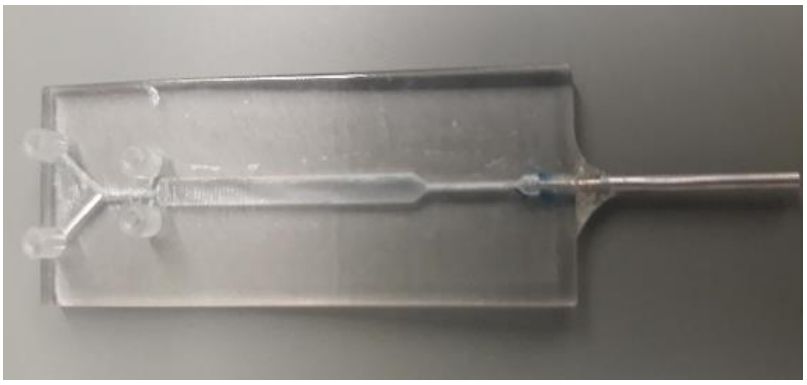

Figure 51. Finished fabricated flow-focus chip product.

It will be of interest in applications to detect droplets leaving the chip in downstream experiments. To check the ability to detect droplets one at a time, a microcapillary tube was fixed to the effluent line of the chip, and a clear detection window was introduced into the line by flame-treatment. Lastly, optical tape was attached to the line to provide a clearly defined detection window. Ideally, droplets would traverse this window one at a time.

Now that the physical chip has been produced, it must be quantitatively evaluated based on the droplet profiles it produces.

3.4 Resulting Droplet Profiles

The selected candidate chip requires a performance evaluation of its droplet generation rate, volume and monodispersity to evaluate its fitness for cell-based screening applications. To observe the generated droplet population more easily, brilliant blue food dye was diluted in water at a concentration of ~10 μL/mL and the resulting solution was used for the aqueous phase. Two aqueous syringes were filled with this brilliant blue solution and fixed to a syringe pump.

Alternatively, two carrier phase syringes were filled with NOVEC 2% S008 w/w and fixed to a second syringe pump. The syringes were coupled to the corresponding ports via Tygon tubing and 21-gauge Brostown syringe needles. The carrier phase pump was set to 9000 μL/hr and the aqueous phase was set to 630 μL/hr. Video was recorded on the flow-focus junction and the incubation channel. Stills were taken of the incubation channel after droplets filled the field. Droplet generation rate was difficult to resolve due to the insufficient frame rate of the camera. However, several droplets were generated per second (a much faster rate than the pilot chip). Visually, the droplets stack across the incubation channel in a uniform, crystalline manner which suggests low variability in the volume distribution (i.e., the droplet population is 'monodisperse') (Figure 52).

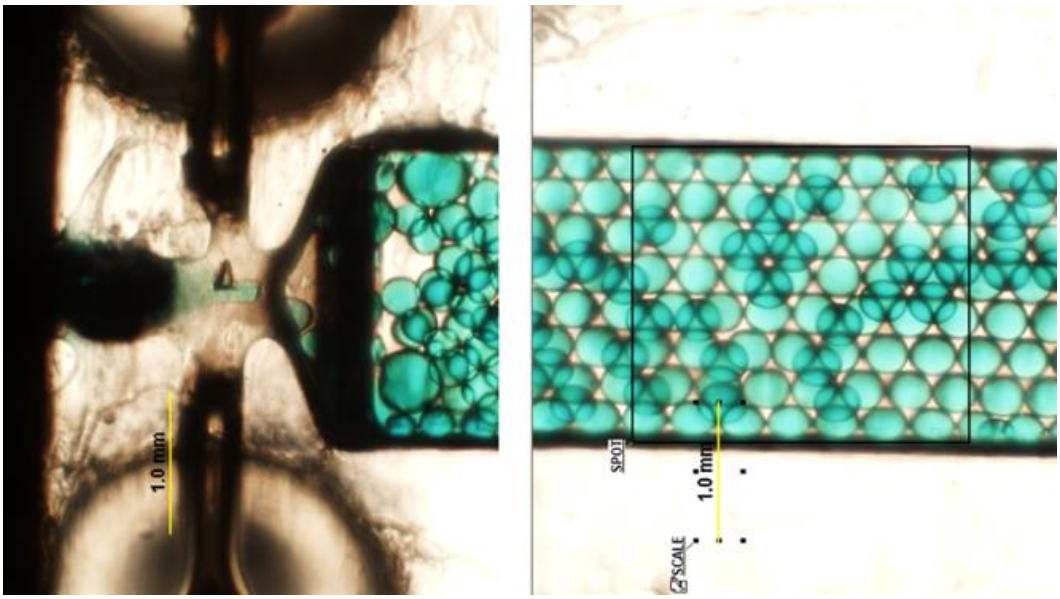

Figure 52. Stills taken from a typical run on the flow-focus chip. The left panel shows droplets forming in the junction and being pushed into the low-pressure incubation channel. The right panel shows the crystalline stacking of the a monodisperse population of droplets slowly traversing the channel.

Video and stills were also taken in the downstream capillary detection window. Ideal behavior would indicate only a single droplet passing through the detection window at any

given time. The data shows frequently two droplets crossing as a time. This problem may be addressed in future experiments by either adjusting flow rate or by simply making the detection window narrower.

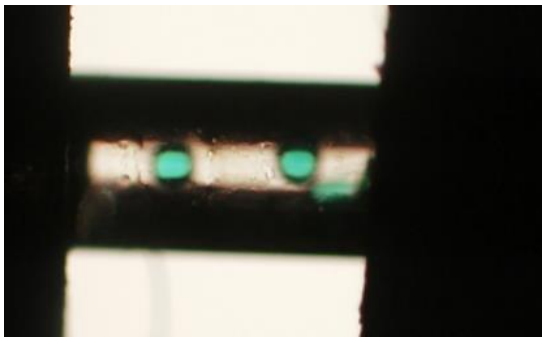

Figure 53. Two droplets are seen crossing the downstream detection window. Optimization is required to ensure single-droplet resolution detection.

To investigate the volume distribution of the droplets, still frames were saved and imported into ImageJ. Cross sectional diameters of the droplets were measured on 24 representative samples. The ‘1 mm’ nominal scale bar was also measured. The data was then exported to Python, in which the pixel measurements were converted to microns by normalizing to the scale bar. The script further converted the cross-sectional distances into volumes by approximating the droplets as perfect spheres and constructed a histogram of the 24 samples. The results were saved as a pandas dataframe.

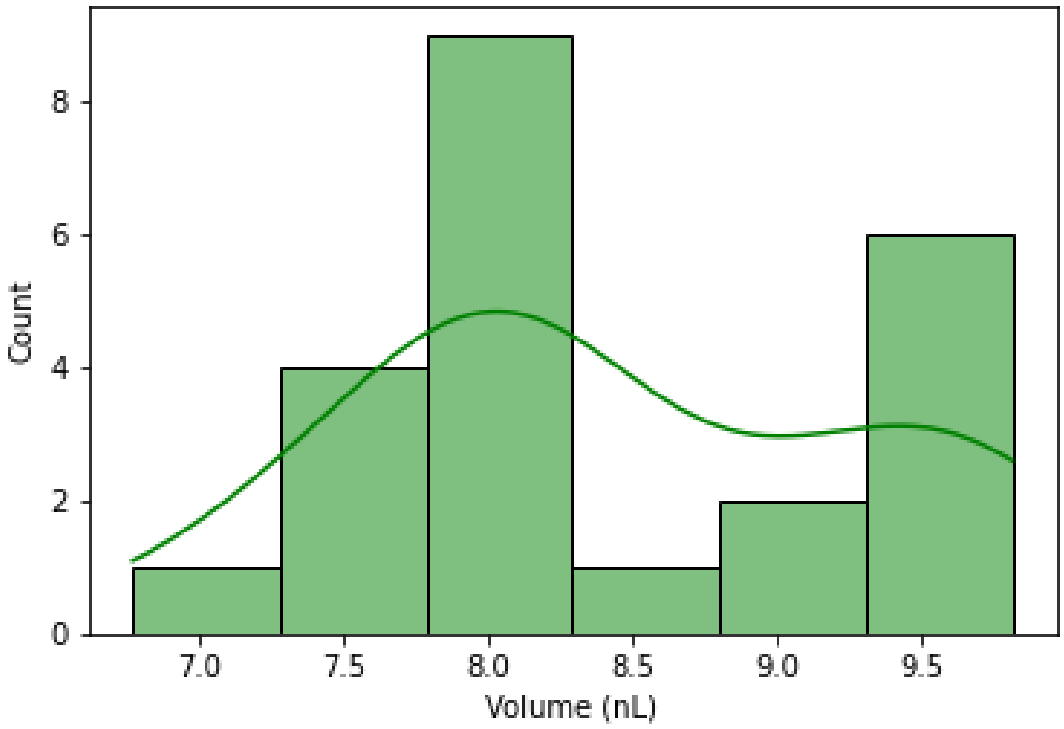

Figure 54. The volume profile derived from the flow-focus candidate chip. The average volume is significantly reduced from earlier experiments (8.4 +/- 0.86 nL). While the population is sufficiently monodisperse, there does seem to be some bimodality in the data, which is not yet accounted for.

In the histogram, it becomes clear that the average droplet volume has dropped significantly relative to those produced by the pilot chips. The volumes in this population were measured at 8.4 +/- 0.86 nL. The standard deviation is only 10.2% of the average, and the entire range spans only ~2.5nL. This evidence suggests that the flow focus chip succeeds in all the metrics that were required for successful application to cell-based assays: an increase in droplet generation rate, a small average volume, and a decrease in volume variability (or equivalently, an increase in monodispersity). This chip is the correct candidate to move forward with integration into biomedical applications such as the antibiotic resistance detection system.

CHAPTER 4: FURTHER 3D PRINTING APPLICATIONS TO BIOMEDICAL ENGINEERING

4.1 Cardiac Organoids

4.1.1 Organoid Background and Perfusion Rationale

Tissue engineering is frequently used for development of biomimetic systems to understand biological systems more thoroughly. Here, I describe my collaborations with the Aguirre et.al. group to develop their model of a human heart more fully using 3D printing and fluidic techniques. The model consists of a heart 'organoid'. An organoid is a miniaturized and simplified simulacrum of an organ that may function as an experimental model[46]. These organoids are built using human pluripotent stem cells (hPSCs). These precursor cells may potentially differentiate into several different cell lineages. For the purposes of this model, they are treated with the known WNT pathway moderators CHIR99021 and Wnt-C59 to induce differentiation into cardiomyocytes[47]. The result is a structure that is strikingly mimetic of a nascent heart. It is a ~2mm spheroid with an internal cavity that is capable of intrinsic beating reminiscent of the human heartbeat[48].

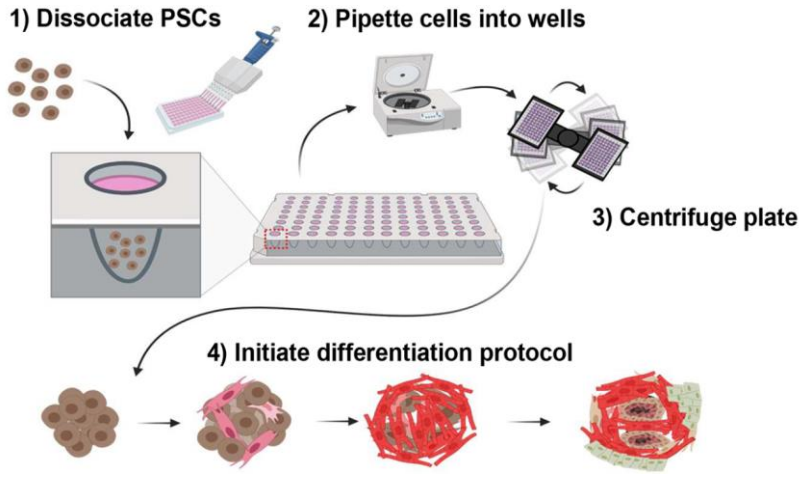

Figure 55. Generation of heart organoids from hPSCs from the Aguirre lab.

The organoids derived from this process are not fully mature hearts. They lack

compartmentalized internal chambers and organized vasculature. The vessels that do exist are tangled, chaotic and nonfunctional. We hypothesized that the lack of organized vasculature can, in part, be attributed to the lack of perfused internal positive pressure that native developing hearts experience as the heart beats and receives blood.

To test this hypothesis, it is necessary to develop a fluidic system that will perfuse media directly into the organoid; this approach will induce tension and stretch onto the organoid tissue, providing a mechanical environment that more closely resembles the *in-situ* environment of the human heart. Before and after positive pressure perfusion for 5 days, alignment of the capillaries in the organoid tissue immunohistochemistry will be measured by immunohistochemistry, along with expression changes in vasculature-associated genes including VEG-F and various mechanoreceptors[49].

4.1.2 Perfusion Experiments

The first requirement in this experiment is the coupling of fluidic lines to a needle capable of puncturing the organoid surface. We make use of borosilicate glass capillaries with an internal diameter of 0.5 mm (Sutter Instruments, BF 100-50-10). These capillaries are traditionally used for creation of micropipettes (pipette tips with extremely fine micro-scale tips) in the field of electrophysiology for patch-clamping neurons[50]. Here we repurpose them for fluidic perfusion of the organoids. To create a micropipette from the capillary, we utilize a capillary puller (Sutter Instruments, Model P-97 Flaming/ Brown Micropipette Puller). Briefly, the machine secures the capillary at each end, softens the middle with a heating filament, and pulls the ends apart. The softened middle then splits into two sharpened tapers, each with an opening on the order of single microns (Figure 56). Empirically, custom program P74 which consisted of 4 heating cycles with a temperature gradient of -1 C for each step (568 C to 565 C) consistently produced

tips with a tip cross section diameter of 16 μm.

Figure 56. Heating and pulling the borosilicate capillary results in a tapered tip on the order or microns. This will serve as the puncturing device for perfusion experiments.

The second requirement of the project is to develop housing that will support the health and survival of the organoid and stabilize the perfusing micropipettes. Considerations include keeping the heart submerged in media and the environment humid to avoid desiccation, providing sufficient oxygen to the organoid to avoid hypoxia, avoiding rapid fluctuations in temperature, and maintaining the constant positive perfusion pressure in the organoid for the duration of the experiment. Initial designs consisted of a simple cup with a tapered bottom to stabilize the organoid in the center. There are inlets on either side of the cup: one to accommodate a micropipette for puncture and media perfusion and a second inlet to accommodate a micropipette for puncture and drainage on the opposite side. The cup was also fitted with a heatsink block to maintain temperature and provide stabilization in the incubator, and a vented lid to prevent evaporation and contamination (Figure 57).

Figure 57. The first-round design organoid chamber. The cup contains channels on either side for pipette insertion. Included was a heated block and a vented lid.

In the initial design, media would be fed through a line into the perfusion micropipette. This media would be perfused under pressure via a pump into the organoid, inducing internal positive pressure and stretch. This pressure and stretch is the mechanical input hypothesized to encourage vascular organization and development in the developing heart. Once pressure was sufficiently built up, it was intended to drain into the low-pressure micropipette inserted into the opposite side of the organoid. A vacuum could be applied to the low-pressure drainage micropipette if drainage were not sufficient to maintain proper homeostasis on the organoid.

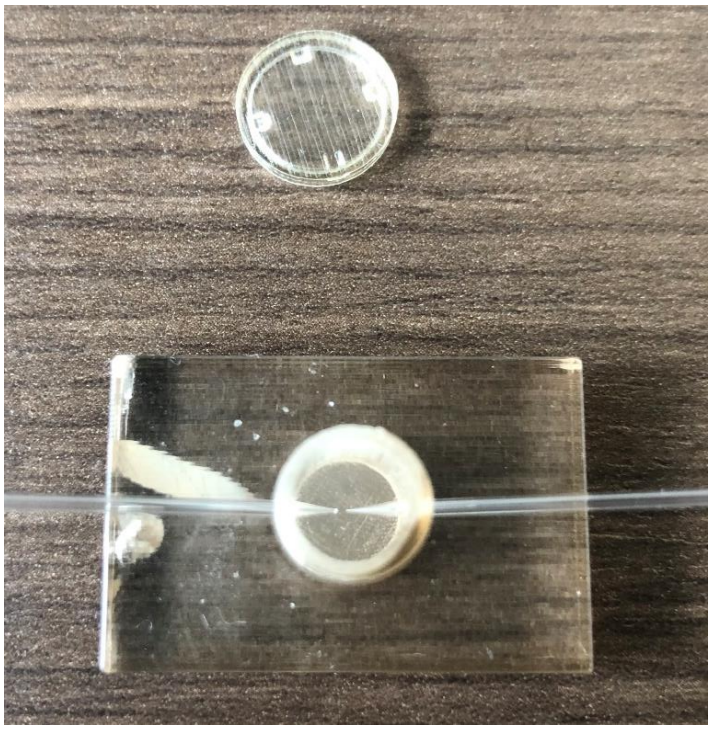

Figure 58. The organoid was intended to be placed in the cup and covered with media. The cup was to be inserted into the heat sink block and micropipettes fed into the channels on either side of the cup, one for perfusion and one for drainage. The vented lid was meant to prevent contamination and evaporation in the incubator.

This designed failed primarily due to its instability. The micropipettes were difficult to secure at the appropriate angle for long-term storage in the incubator, and the organoids in the cup or ‘chamber’ appeared susceptible to desiccation. Additional support structures seemed necessary to guarantee a biologically favorable and mechanically stable perfusion chamber. Such supports include micropipette guides to keep the micropipettes fixed in place during the perfusion, a channel array to allow perfusion of multiple organoids at once while providing mechanical stability, and an overhead drip system that drops media on top of the organoid and prevents desiccation in the event of media evaporation (Figure 59).

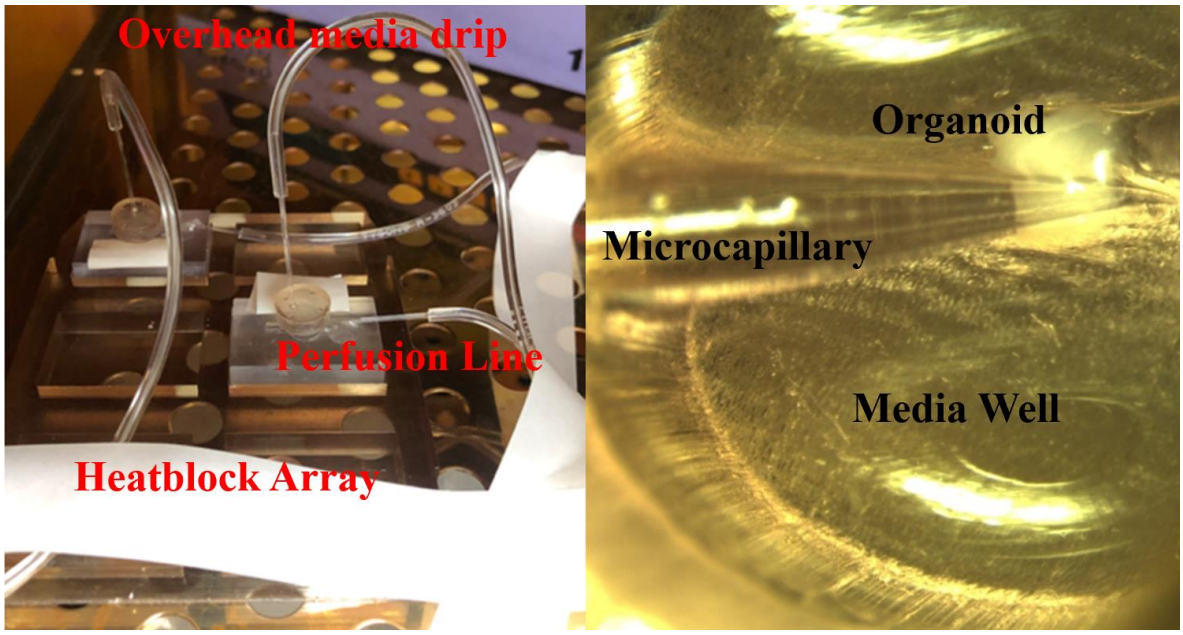

Figure 59. In the left panel, the organoid chamber is re-imagined as an extended array. Microcapillaries are supported by guide channels and secured in place by epoxy. In the left panel, we see issues with the unstable positioning of the organoid as it is pushed around the surface by the micropipette tips.

The organoid chamber was redesigned as part of an array. This array serves dual functions of permitting the perfusion of multiple organoids in parallel as well as mechanically stabilizing the system in the incubator. Additionally, the guide channels were integrated into the heatblock next to the ports to secure and support positioning of the micropipettes. Finally, ports were placed in the lids to allow for an overhead media drip system. This allows insertion of an unpulled capillary to drop media at a slow rate onto the organoid to avoid any problems with the tissue drying out.

The design failed due to the toughness, or rigidity, of the organoid tissue. The micropipettes tended to push the organoid across the surface rather than pierce it, indicating the need for a redesign with further translational restrain on the organoid. Additionally, the epoxy seems to soften and loosen in the incubator, rendering the microcapillary unstable.

The refactored organoid chambers feature a ‘pedestal’, which houses the organoid in a

concave bowl to secure it in place. The pedestal also has opposing notches to allow insertion of the micropipettes. Around the organoid was placed a bath of media, intended to increase local humidity, and lower the odds of desiccating the organoid. Other added features such as the channel array and the micropipette guides were retained from previous designs. A black dye was dissolved in the aqueous phase to permit visualization of the perfusion more easily. Initially, it was necessary to verify that the pedestal stabilized the organoid securely enough to permit puncturing from either side by the micropipettes. Multiple organoids were successfully perfused on the pedestal structure, verifying reproducibility when piercing the internal cavity of the organoid (Figure 60).

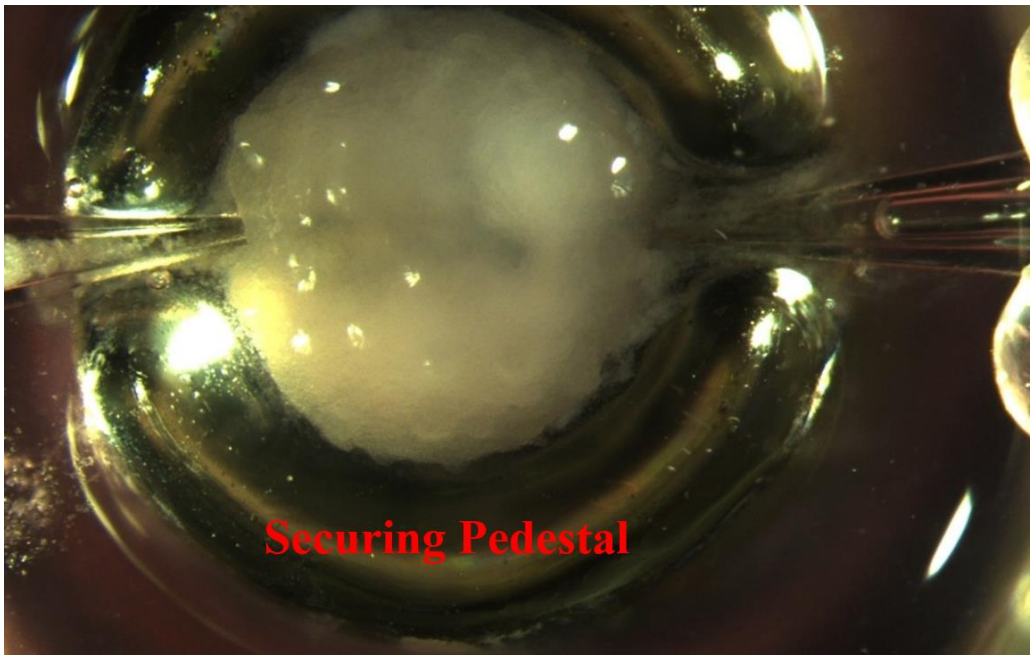

Figure 60. Successful puncture of the organoid by the perfusing micropipette (left) and the drainage micropipette (right). The black tracker dye is partially visible in the organoid.

Once the capacity to puncture the organoids with high precision was established, it could now be determined if pumping media through the micropipettes induced a positive pressure stretch on the internal cavity of the organoid. Experimental validation of the theory is shown

below (Figure 61). The organoid was placed in the pedestal and punctured on either side by the micropipettes. The perfusion pump was set to 300 μL/hr, and the resulting flow into the organoid was recorded in .avi video format:

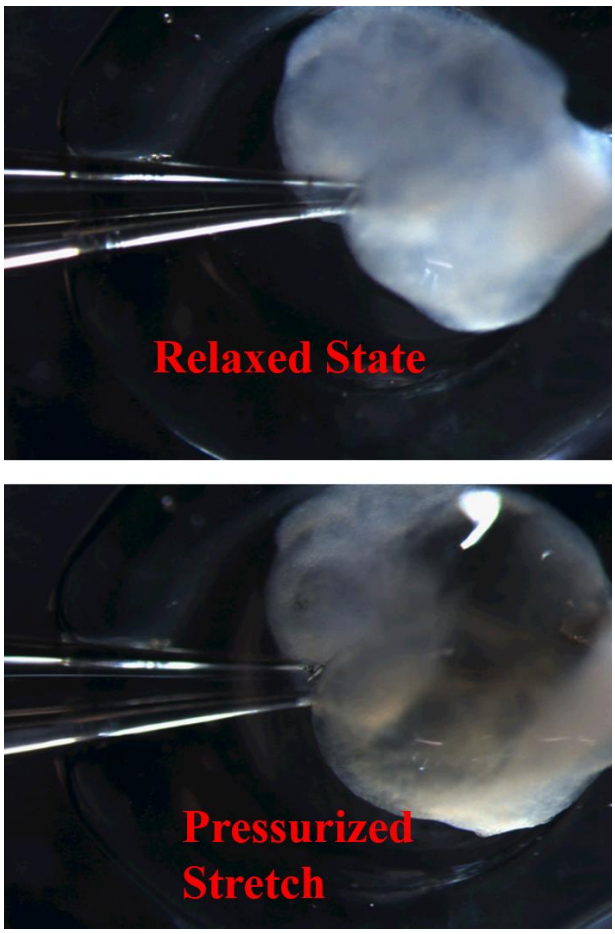

Figure 61. Flow at 300 μL/hr into the organoid is observed. Over the course of 2 minutes, the organoid swells and stretches, with the black ink visible inside the interior cavity. At approximately the 2-minute mark, the organoid bursts.

Over the course of approximately two minutes, the organoid visibly swells and eventually bursts. This indicates that, while 300 μL/hr pump rate is too high, the positive perfusion and mechanical stretching of the organoid tissue is a feasible approach. Further experiments indicated that 100 μL/hr more sustainably stretched the internal cavity while avoiding rupture. The device to this point was found lacking on the issue of syringe volume. The organoid must be perfused

for between 5-7 days before immunohistochemistry and expression analysis are performed, so even the largest available syringes will not carry sufficient volume to pump at this rate for such a long duration. Therefore, the new organoid chamber must make use of media recycling, in which the pump pushes the media into the organoid, and the media is later retrieved and returned to the pump in a closed circuit.

The media blocks were redesigned with drainage channels, meant to collect the media after it had been pushed through the organoid cavity. The collected media was designed to be driven to a specified media-reservoir device, which would then be re-perfused into the organoid in a cyclical fashion. To perform this pumping mechanism, the driving pump technology would be a peristaltic pump, rather than a syringe pump. With this advent, theoretical perfusion time becomes unlimited rather than a function of the internal volume of a syringe.

Practically, rather than the perfusion being limited by the syringe eventually running out of media, it would only be limited by the eventual nutrient depletion of evaporation of media as it continually circulates in the incubator. However, both potential issues may be addressed merely by adding fresh media to the modular ‘media reservoir’ mid-run without disturbing the organoid chamber itself. The redesigned closed-circuit chamber system was designed to address all the shortcomings of the previous devices.

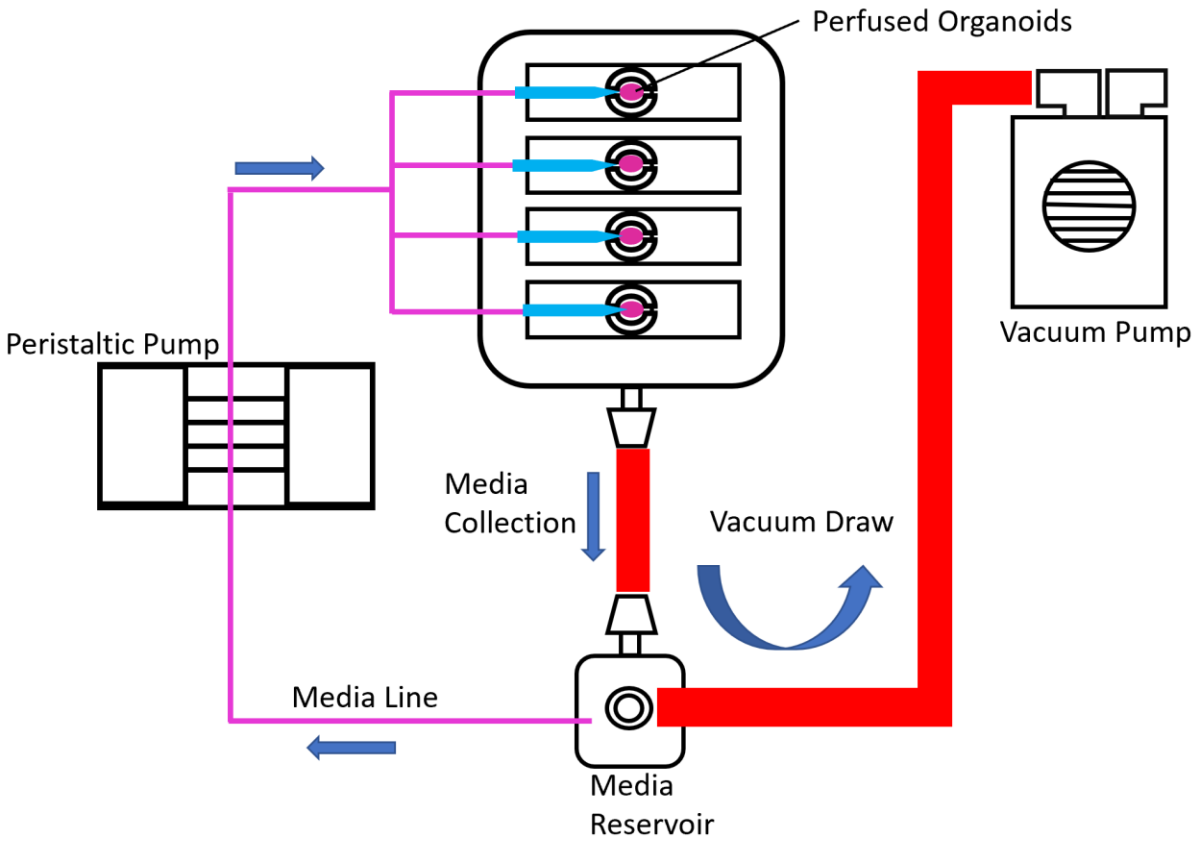

Figure 62. The redesigned peristaltic pump closed-circuit system. Recovered media is to be drawn out of the organoid chamber by vacuum into a media reservoir where it can be recycled back into the perfusing media line. The overhead drip system is retained to prevent organoid desiccation.

In this closed-circuit system, the perfusion is no longer limited by the limited media capacity of the syringe. If media is refreshed at the modular media reservoir, the system theoretically permits perfusion without an upper time bound.

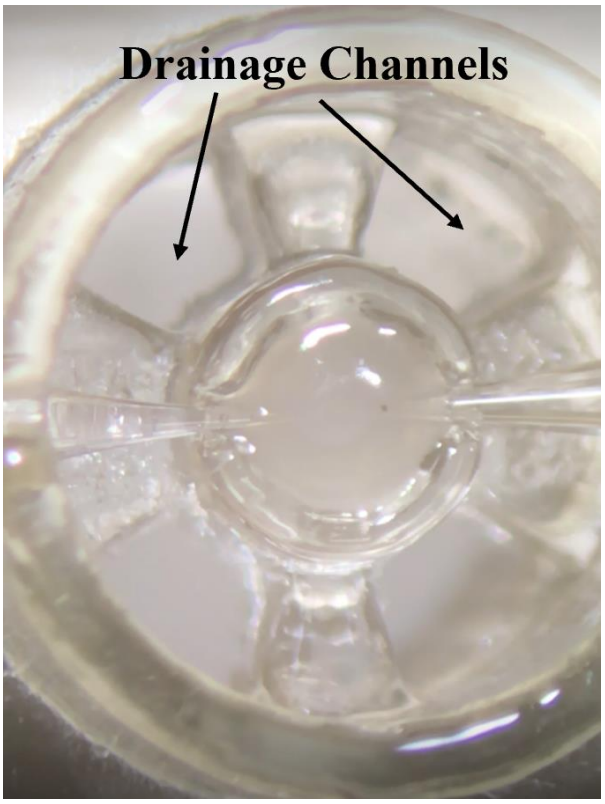

Figure 63. To permit media recirculation, the organoid pedestals and base blocks were fit with drainage channels. The vacuum pump included in the circuit is intended to draw the media back to the modular reservoir with negative pressure.

The circuit was tested as described above. The organoid was perfused as previous described, the vacuum pump was activated, and the peristaltic pump was set to 1.55 μL/min. The entire circuit was allowed to run in the incubator at 37 C, 5% CO_2 overnight. Signs of success would include a lack of visible leaks anywhere in the circuit and the organoid appearing viable and demonstrating signs of surface stretch. At 16 hours, the organoid chamber was retrieved from the incubator and the system was opened for inspection.

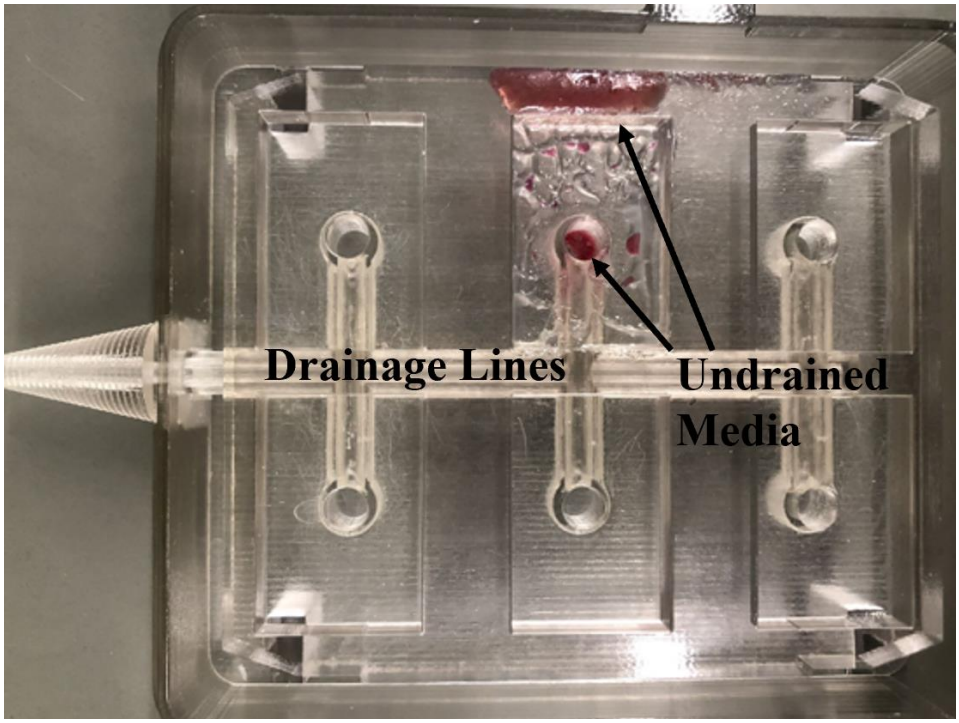

Figure 64. The drainage system failed to return the media to the modular reservoir, and it appears the overhead drip system leaked offsite rather than dripping onto the organoid. A more robust system will need to be devised.

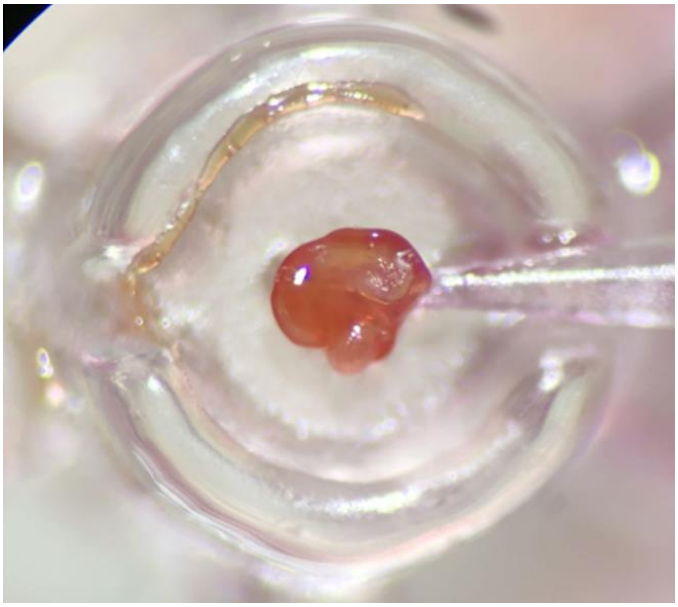

Figure 65. The organoid has dried to a hard, tacky consistency. Media remained in the micropipette tip, but the perfusion pump had failed to prevent the organoid from drying out. The overhead drip system is not adequate for organoid viability.

The chamber clearly showed signs of leakage. Additionally, the organoid itself had completely desiccated to a shrunken, tacky consistency. This evidence indicates that not only is the overhead drip system prone to failure, but also that the drainage system (as designed) to does not return media to the reservoir. A more robust system is required to prevent the desiccation of the organoids. To address this problem, the chamber was redesigned to keep the organoid totally submerged in a media bath during the entire perfusion process.

The bath system involved perfusing the organoid in a fully submerged environment and allowing the ejected media to enter the bath. Media would be recovered directly from the bath by a 'sip' system, where collection tubes draw media back to the reservoir by negative pressure, again driven by a vacuum pump (Figure 66).

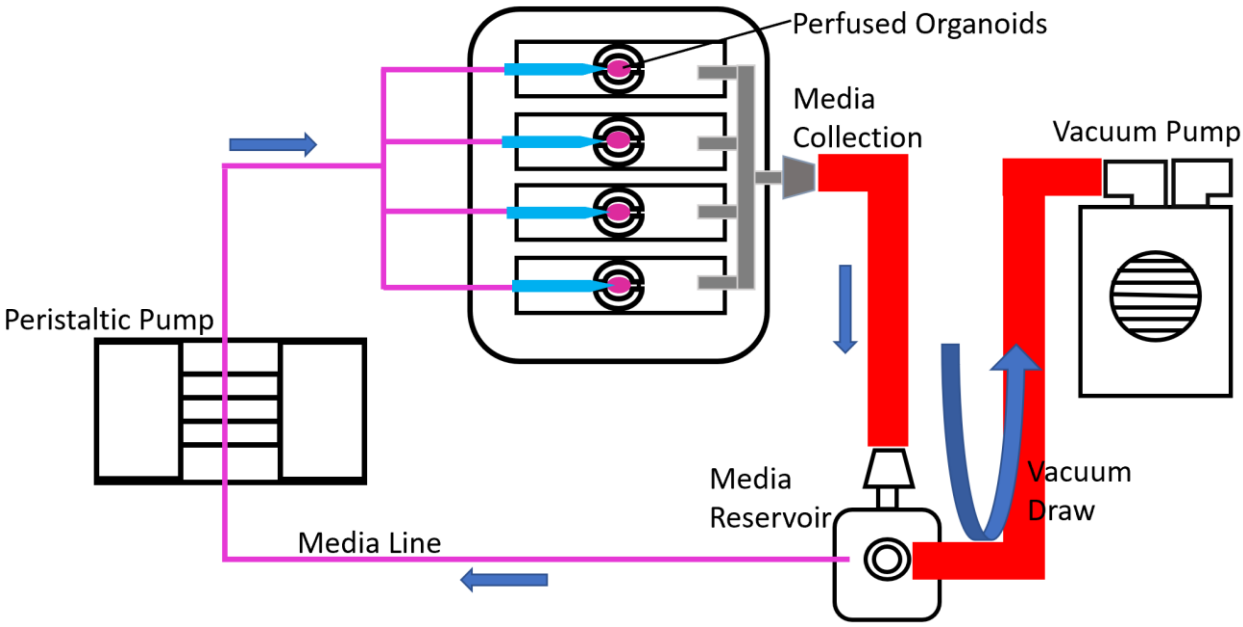

Figure 66. The revised system keeps the organoid submerged in a media bath during perfusion to avoid desiccation. The 'sip' is intended to draw media from the bath back into media reservoir and circulate it back to the perfusion micropipettes.

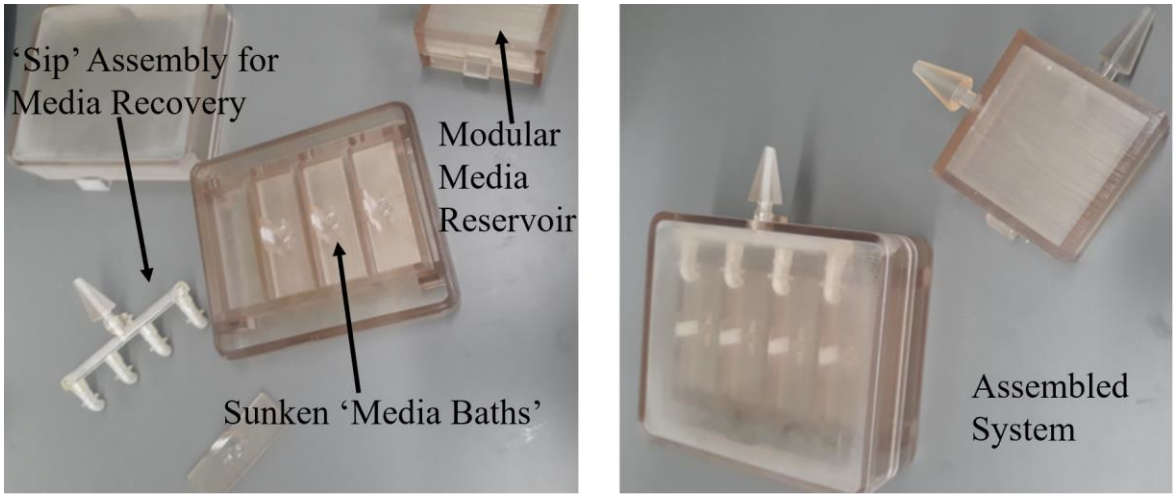

Figure 67. Left Panel: The revised organoid chamber (center) shows the pedestals submerged in modular baths. The sip (left) can be set in the braces to position it for media drainage during the run. On the top left the chamber lid is shown and on the top right the modular media reservoir is visible. Right Panel: Assembled chamber and modular media reservoir.

The performance of this update, like previous iterations, requires validation via an overnight perfusion test. The organoids were perfused on the pedestal as before, which was then submerged into the media bath on the organoid chamber. The sips were then lowered into the baths and the chamber was fully assembled with the media circuit. The entire system was moved into the incubator overnight (Figure 68). At 16 hours, the chamber was retrieved from the incubator and the system was carefully observed.

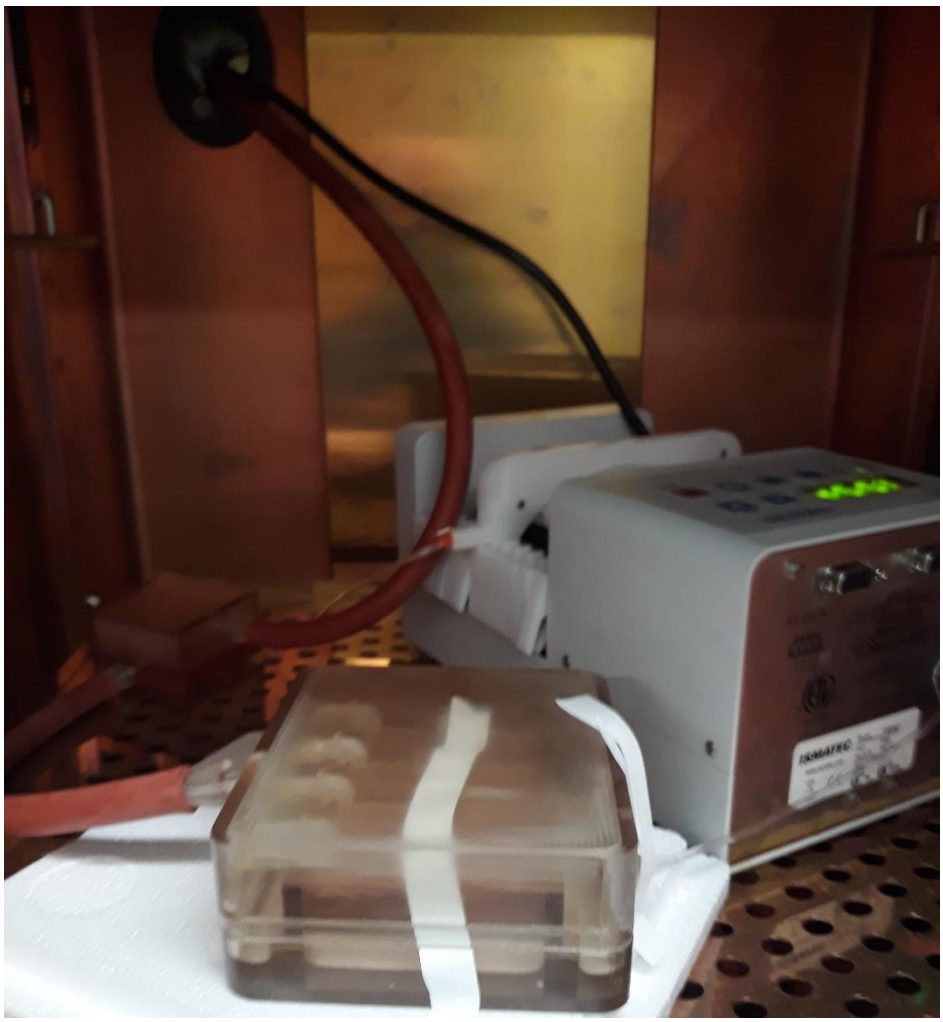

Figure 68. The system was assembled in the incubator, and the vacuum lines were fed out to the external pump. The temperature, CO2, and humidity of the incubator should favor the survival of the organoid for a 5-day perfusion.

Upon observation, the modular media reservoir was completely dry, and the media in the media baths were suffering from evaporation. This experiment made it clear that the negative pressure from the vacuum pump was promoting rapid evaporation of the media in the circuit (by increasing vapor pressure). To build a successful circuit, the vacuum pump must be eliminated from the circuit and a replacement driver must be included to move media from the chamber back to the media reservoir.

This problem was solved by simply assigning the recovery function back to the peristaltic

pump. The vacuum pump can be obviated from the circuit by simply using the same peristaltic pump to drive media in and out of the chamber (two media lines running an antiparallel fashion). The antiparallel system is shown diagrammatically below (Figure 69):

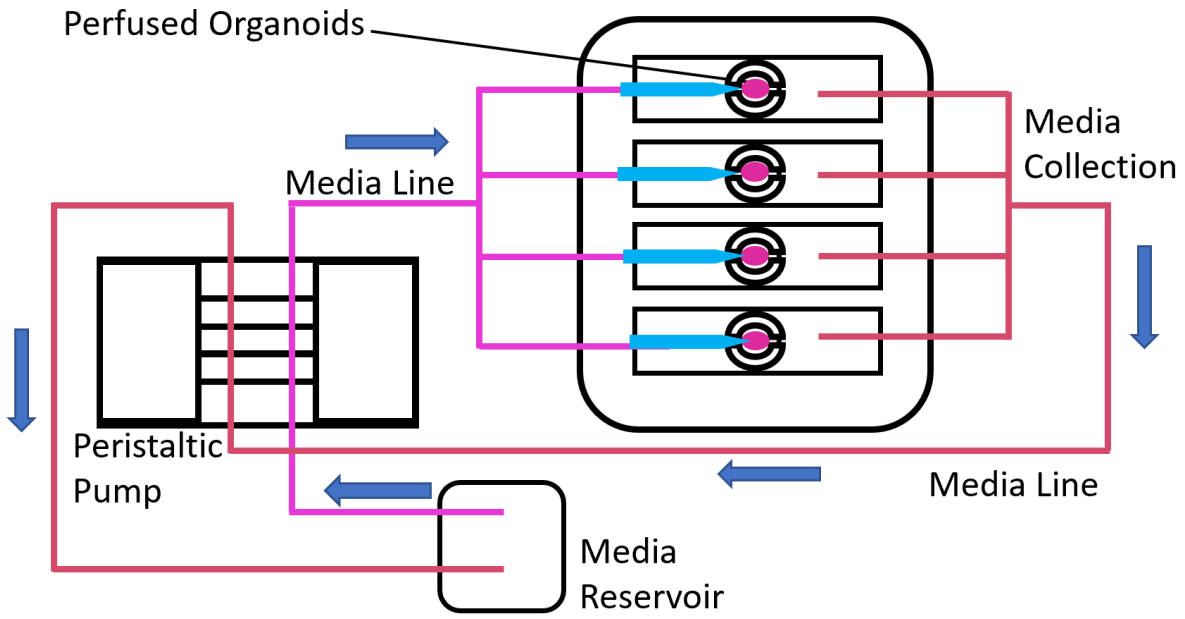

Figure 69. The perfusion line draws from the modular media reservoir and splits in between four micropipettes feeding into the organoids. Simultaneously, the retrieval line pulls media from the chamber and returns it to the media reservoir, running in an antiparallel fashion to the perfusion line.

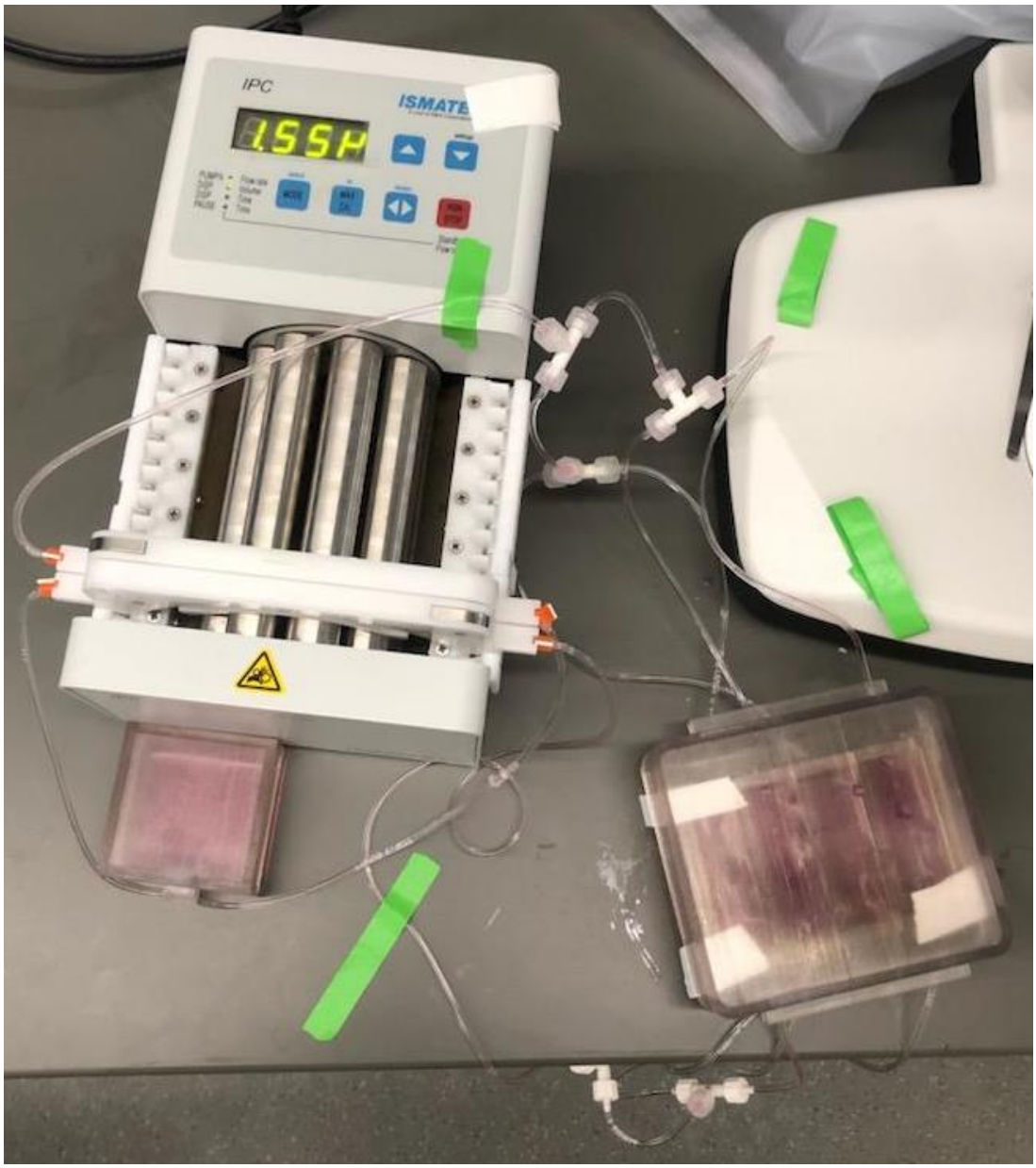

Figure 70. The constructed system using Harvard fluidic components and Tygon tubing. The removal of the vacuum pump and near-complete isolation of the system should eliminate the evaporation problem and prevent organoid desiccation. Additionally, epoxy was replaced with dental rubber bands and an Agilus gasket for fixing the micropipettes in place after organoid puncture.

Organoids were punctured as normal, and micropipettes were secured with dental rubber bands. The system was assembled as shown (Figure 70), and the peristaltic pump was turned on and allowed to run for 1 hr on the benchtop. The real-time observations of this circuit trial

suggest that this design is successful. Media was observed being drawn into the retrieval line, and after 1 hour of perfusion, the organoid did not appear to have torn or burst.

This current antiparallel circuit design appears to be adequate to proceed with extended perfusion experiments. Additional considerations for a 7-day experiment may be the need to replace media in the modular reservoir as nutrients deplete and possible deformation of the Tygon tubing over time. After an extended perfusion, the organoids will need to be imaged, analyzed by IHC, and expression profiled by RNA-Seq.

The hypothesis that positive pressure perfusion and stretch play a role in maturing the nascent heart would predict that post-perfusion organoids will more closely resemble mature hearts than pre-perfusion organoids. Semblance to mature hearts can be measured by fluorescent microscopy (i.e., if the vessels are organized into orderly capillary beds or internal chambers have developed) and RNA expression patterns. If the variance in expression of vasculature and mechanoreception genes between organoids and mature hearts decreases over time (in other words, if the covariance increases and the deviation decreases), it is justifiable to say that the organoids have been stimulated to ‘mature’ in response to perfusion.

4.2 Synthetic β-Islets

4.2.1 β-Islets: Type 1 Diabetes and Grafts

Type 1 diabetes is an autoimmune disease canonically characterized by the body’s immune system attacking its own pancreatic β-cells[51]. These β-cells form the central components of the ‘Islets of Langerhans’ in the pancreas which are responsible for secreting the insulin that controls blood glucose levels in a healthy human[52]. Destruction of these islets results in loss of insulin secretion, and a consequent inability to moderate serum glucose concentrations. Spikes and irregularities in glucose cause many downstream problems in human physiology including

immune suppression, neuropathy, blindness, and early death. This underlying pathology and its associated symptoms are collectively referred to as ‘diabetes’. Several methods have been explored to mitigate the symptoms of diabetes including diet control, exogenous insulin injections, and C-peptide therapies[53]. However, a more proactive approach is to engineer pancreatic tissue ex-vivo for the purpose of grafting into the patient and restoring the lost function[54]. The additive method suited to creating synthetic pancreatic tissue is bioprinting. Cells in the pancreatic Islets of Langerhans consist largely of interacting β-cells and endothelial cells. To replace lost pancreatic islets, it will be necessary to print a hydrogel laden with β-cells and endothelial cells in a geometry that favors both the adherence of the islet to the pancreatic surface and a high enough surface area to volume (SA/V) ratio to efficiently excrete insulin. The ‘taurus’ is a donut-shaped geometry, which combines both a planar overall structure and a relatively high surface area to volume ratio.

In collaboration with the laboratory of Dr. Ping Wang, I worked to produce synthetic Islets of Langerhans, consisting of a hydrogel laden with HUVEC-GFP cells (human endothelial cells tagged with a green, fluorescent tracking protein). Ideally, these synthetic islets should not exceed 300 μm in diameter.

In service of this goal, we make use of a pneumatic driven 3D bioprinter, the ‘Allevi 3’. Hydrogels and synthetic ECMs, called ‘bioinks’, will be mixed and loaded into syringes for deposition into the correct geometry by the bioprinter.

4.2.2 Bioprinting Synthetic β-Islets

Two frequently utilized resins for tissue printing applications are sodium alginate[55] and GelMa[56]. Sodium alginate is a soft polysaccharide that prints as a liquid and is later polymerized by exposure to divalent cations such as Ca^{2+}. Sodium alginate has certain advantages, in that it is

cheap relative to other bioinks and biocompatible with many cell types. However, alginate is very soft and can have trouble maintaining structural integrity. Additionally, sodium alginate has no binding site for the cells and has limited mechanical interaction with them. Finally, sodium alginate must be printed as a liquid and cured with divalent cations post-print. This can make printing fine details at higher resolution requirements difficult due to simple diffusion limits. GelMa, on the other hand, is an expensive acrylate-based derivative of gelatin. It has binding sites for cells and interacts with them in a more involved mechanical arrangement like *in vivo* tissues. Also, due to the acrylate-based polymerization, GelMa may be cured concurrently with the print by irradiating with blue (~405 nm) light on the nascent print between deposition of each layer.

As part of a pilot study, we attempted to print a pilot cell-free taurus (designed in SolidWorks as a CAD file). Sodium alginate was chosen as the bioink due to cost considerations. The sodium alginate was dissolved to 2% w/v in milli-Q water (2 drops of brilliant blue food dye was added for visualization) and loaded into a 5 mL Allevi syringe. The syringe was fixed with a metal 27G tip and loaded into the Allevi print head.

The printer bed was loaded with a petri dish full of the company-recommended bead-based support material: ‘Life Support’. The printer was set to the following parameters: 0.2 mm layer height, 12 mm/sec printer speed, 5 psi, 21 C. The printer Z axis was manually calibrated, and the file was printed. Once the print was complete, the part was submerged in 100 mM $CaCl_2$ to initiate polymerization The resulting prints are shown below (Figure 71):

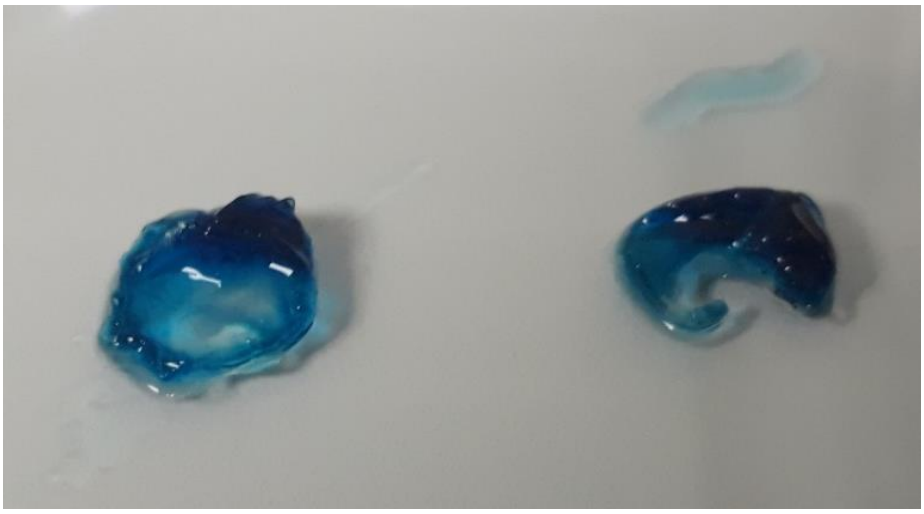

Figure 71. The taurus structure printed in sodium alginate failed to hold its shape. In one of two attempts, the structure failed to successfully complete the circle.

The sodium alginate failed to hold its shape to any degree of accuracy. The soft polysaccharide deformed during the Life Support/ alginate system does not appear well-suited to this application. The next step will be to attempt the same print using GelMa as a bioink. GelMa is a stiffer hydrogel and should provide more structural integrity than the alginate.

To prepare the bioink, 0.15 g GelMa was mixed with 0.0075 g LAP (the photoinitiator required for polymerization) and dissolved in 1.5 mL PBS to generate a 10% w/v GelMa solution. The mixture was stirred in a sealed vial at 60 C for 20 minutes to facilitate the dissolution of the GelMa. To remove bubbles from the ink, the solution was centrifuged at 1000*g* for 3 min at room temperature. The bubble-free ink was then loaded into an Allevi syringe coupled to a 30G metal syringe type. The syringe was stored on ice to increase viscosity while the software was prepared. Parameters were set to 21 C, a pressure of 3 psi, and print velocity of 12 mm/sec. A 3 mm diameter taurus was loaded into the software and the print job was started. The program was set to cure with blue light every 2 layers (N = 2). The resulting prints were retrieved from a petri dish and measured for diameter. The nominal diameter of the file is 3mm, but the resulting structures more closely approach 4-5 mm (Figure 72).

Figure 72. The taurus shapes printed in GelMa were a success. The shapes were correct, and the rigidity was sufficient to survive removal from the substrate and transfer to media. The resulting diameter was slightly larger than the nominal diameter specified in the CAD file, but the print protocol may be optimized.

The results are much closer to the nominal design structure than those of sodium alginate. While the nominal diameter is not precisely the dimension specified in the CAD file, the shape is well defined and keeps its shape well when removed from the petri dish. Considering the relative success of this pilot experiment, GelMa is the appropriate bioink to proceed with further developing the synthetic islets. The next step in the process is the inclusion of HUVEC-GFP cells.

To test the efficacy of cell inclusion, a T75 flask of HUVEC-GFP was grown to 75% confluency and cells were harvested to and spun down to a cell pellet. GelMa was prepared as before, and 2mL was used to resuspend the pellet and gently homogenized by trituration to avoid introduction of bubbles. The cell-bioink mixture was loaded into the Allevi syringe with a 30G metal tip. The Z-axis was manually calibrated, and the mixture was dispensed onto the petri dish and cured with UV. The resulting polymer was then visualized under FITC channel.

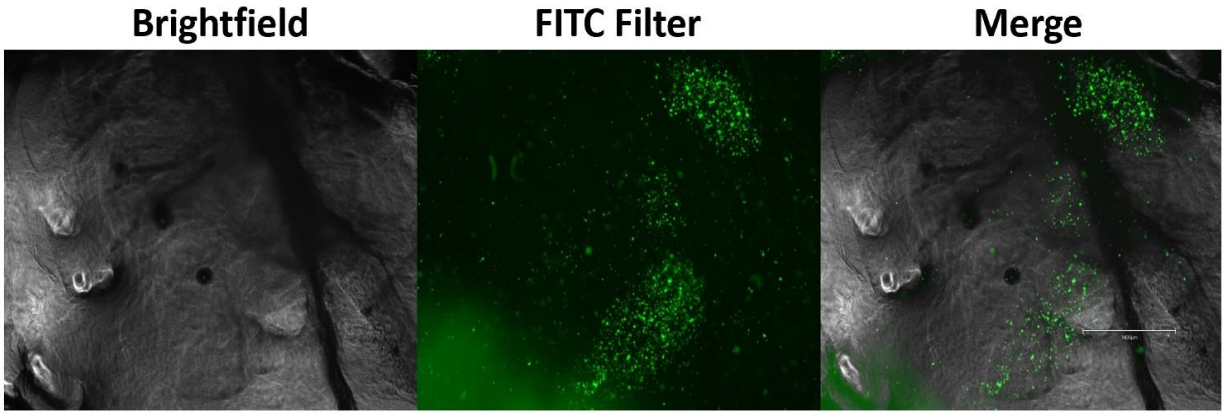

Figure 73. In this pilot cell-inclusion study, the HUVEC-GFP appears as green, fluorescent dots under the FITC channel suspended within the GelMa bioink.

The HUVEC-GFP was visible as green dots in the hydrogel. The cell inclusion appeared successful. However, the cells are not dispersed evenly. For future experiments, greater care will need to be taken to homogenize the cell suspension before printing.

Following validation of cell inclusion, it will now be required to produce a homogenous cell-laden taurus. 10% GelMa was prepared as previously described. 0.8 mL of the GelMa solution was mixed with 4 million HUVEC-GFP cells by gentle but thorough pipetting to avoid introduction of bubbles. Remaining bubbles were removed by centrifugation at 1000*g* for 3 minutes. The mixture was pipetted again very gently to counteract any settling of the cells. The solution was then pipetted into the Allevi syringe, and cool on an ice bath for 10 min. A 30G metal syringe tip was fixed to the syringe, and it was loaded on the Allevi under the following parameters: 21 C, 3 psi, 12 mm/sec. However, it seemed that the cells had caused the bioink to thicken, and the ink did not exit the tip. To counteract the increased viscosity, the temperature was increased in 0.5 C increments until it reached 23 C. Photocure settings were set to 15%, 10 seconds every layer (N=1). The bioink finally printed the taurus as follows:

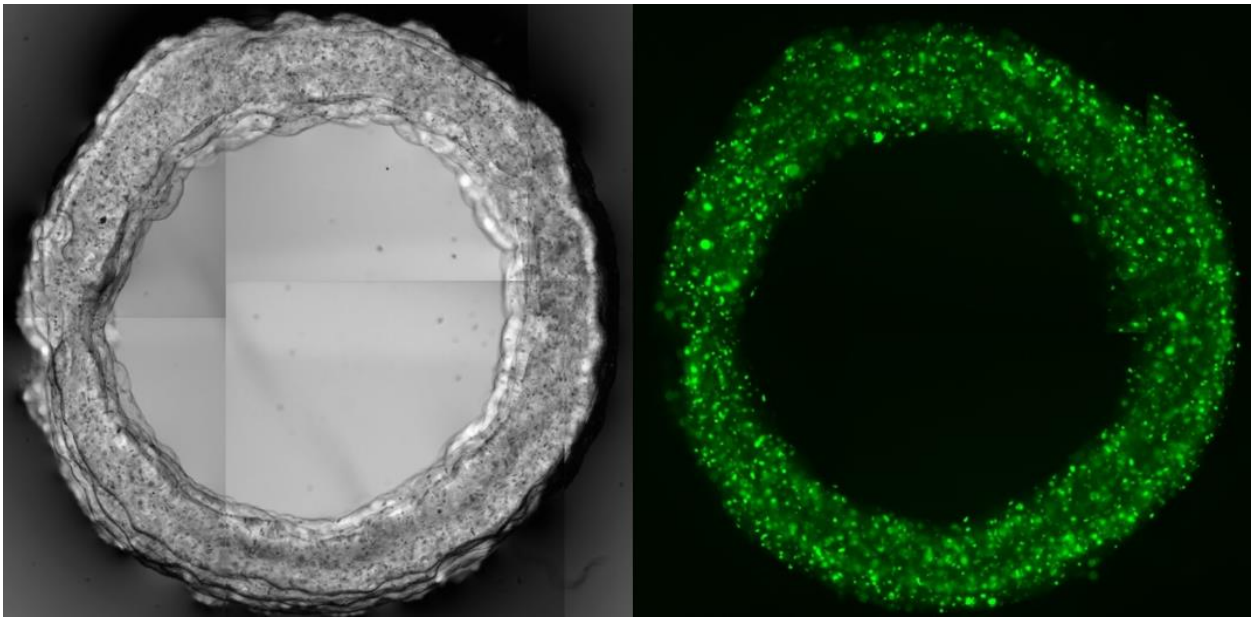

Figure 74. Left Panel: Optical Microscopy view of the 3mm cross section taurus. Right Panel: HUVEC-GFP visualized by fluorescence under FITC channel.

The print faithfully reproduced the CAD file taurus specifications. Additionally, the cells were homogeneously distributed throughout the GelMa. However, given the failure to decrease the features significantly below this scale, as well as the 30G tip being the smallest available tip for this system, the Allevi 3 lacks the sufficient resolution to achieve the desired print size of 300 μm. It is important to consider other bioprinting platforms to find a sufficient resolution.

4.3 Phantom Fabrication for Training of Neural Nets in Image Segmentation

4.3.1 Motivation for Training Neural Networks to Recognize Cell-Dense Regions

A related problem to the synthesis of Islets of Langerhans for transplantation into patients is the *in-situ* detection of transplanted cells and discrimination between live and dead cells. This becomes particularly important when tracking the efficacy of the synthetic islets to detect how well they are surviving and secreting insulin. Historically, these kinds of transplanted islets tend to progressively die over time, and therefore their ability to modulate serum levels of glucose deteriorates[57]. It is therefore of scientific and clinical importance to monitor the viability and

location of transplanted cells.

In a collaboration with Dr. Ping Wang's group, PET/MRI dual imaging modalities are combined into a dual mode-detection system. This system is used to improve sensitivity of detecting radiolabeled cells. However, due to temporal signal decay and selection bias, artificial intelligence is required to interpret the signal from the PET/MRI data. Training this AI (specifically 'convoluted neural net' or CNN) will require exposing it to defined shapes containing known amounts of cells and radioactivity. This CNN can learn to identify and segment regions of cells, as well as quantify the number and viability of cells in the region.

These shapes are 3D printed casts referred to here as 'phantoms'. The phantoms are filled with radiolabeled cells and then exposed to PET/MRI imaging. The data from the imaging is then used to train the CNN to identify the cell regions and quantify cell viability.

4.3.2 Phantom Design and Fabrication

The phantoms are printed the specifications of the detection stage. Simple geometric patterns are used for the training patterns (polygons), and one non-geometric pattern (a raindrop shape) was also used for CNN training. The parts were printed in Veroclear, and a gasket-sealing lid was manufactured to prevent evaporation during measurements. The CAD files (Figure 75) and physical prints (Figure 76) are shown below.

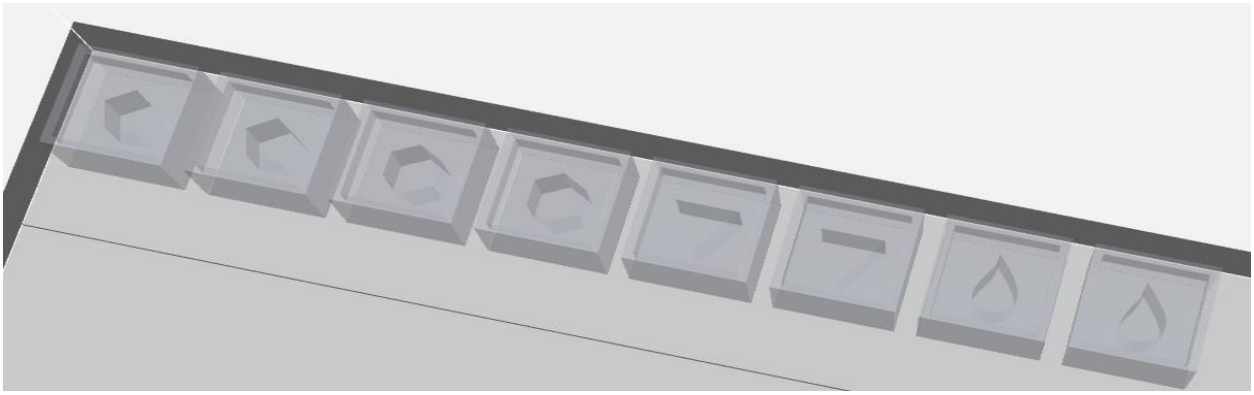

Figure 75. CAD Rendering of the phantoms used for training the neural net.

Figure 76. Veroclear fabrications of the cell-region phantoms.

Upon integration of the synthetic islets into diabetic patients, it will be necessary for the islets to be evaluated in terms of distribution and survival over time. The PET/MRI dual imaging modality may advance the ability to detect the distribution and viability of cell *in-situ*, but the image-reading AI must first be trained and additive-manufactured phantoms like the ones above.

CHAPTER 5: FUTURE DIRECTIONS

5.1 Integration of Droplet Chip into Capillary System

Antibiotic resistance is one of the most serious healthcare threats of the 21st century. This problem is compounding over time as many of the most serious pathogens acquire genomic mutation and plasmids that confer resistance to multiple board-spectrum drugs and drugs of last resort. The spread is aggravated by modern practices such as prolific global travel, routine doping into livestock feed, and inappropriate use of antibiotics to treat viral infections. Paradoxically, healthcare settings are the worst offenders of propelling antibiotic resistance. The unique concentration of immunocompromised and elderly admissions, constant influx of patients carrying resistance pathogens, and physical circulation of physicians and hospital staff constitutes a highly favorable environment for resistance spread. To slow the spread of antibiotic resistance, it will be necessary to remove some of the selective pressure that favors the survival and proliferation of resistant bacterial strains over their more innocuous antibiotic-sensitive neighbors.

One method of reducing pressure would entail the elimination of escalation/de-escalation strategy. The common-place tactic prescribing board-spectrum antibiotics before the results of antibiotic screens are available is, while often effective at improving individual patient outcomes, is a major accelerant of the spread of resistance. However, summarily ending the practice would certainly result in mistakes, untreated illnesses, and increased patient deaths. Thus, the laboratory results must be accelerated, to such a degree that laboratory information can be returned in a truly point-of-care fashion. The objective is to test a patient during admission or during their scheduled appointment times, much in the same way that current flue-tests are administered. This advancement would eliminate the need for escalation entirely, and thus relieve a tremendous

amount of selective pressure currently driving the obsolescence of several clinical antibiotics.

In chapter 2, the potential of a microcapillary device to test resistance on extremely small amounts of analyte was explored as an alternative to commonly use plate-based screens. By optimizing the device in a stepwise fashion, the protocol for detection was systematically determined and the device successfully discriminated between a kanamycin resistant strain and its sensitive analog. After this proof-of-concept, the specific sample preparation for the device needs to be considered to minimize the time between patient arrival and the availability of robust resistance profile.

As discussed in chapter 3, there are strengths to utilizing a droplet microfluidic platform for biochemical (and particularly cell-based) sample screening. Particularly, small levels of analyte may generate a high concentration and more discernable signal when confined to droplets of only a few nanoliters. Further, cell-level resolution becomes available when cells are isolated into droplets from the general population. Instead of a population ATP average, it would become feasible to see what percentage of the cells are resistant to any given challenge drug. Alternatively, it may be such that covariance of the discrete droplet signals might discriminate between a single multidrug strain or a polygenic mix of different pathogens. But the most interesting case-specific application of droplet microfluidics is the potential to couple phenotypic and genotypic data through droplet sequencing.

Droplet sequencing is a developing field which seeks to gather sequencing data on a population of discrete droplets rather than a bulk solution. Several applications are already matured and monetized, such as the now-common digital droplet PCR test or ‘ddPCR’. Here, it may be possible to correlate which cells lyse in response to antibiotic with their underlying genetic information. It is easy to conceive a system in which the droplets are sorted based on

fluorescence (again, already a commonplace practice in FACS protocols) and probing them both with sequencing primers to test for specific genetic differences between the resistant and sensitive populations. Primers targeted at genes associated with the drug's mechanism of action, such as the penicillin binding protein or bacterial ribosomal subunit, might carry mutations or other sequence difference between the strains. Primers might also be targeted to sequences found in common resistance plasmids. Different amplification between resistant and sensitive strains in an experiment like this might shed some causal evidence on what genetic elements are contributing to a resistance phenotype.

A useful tool that could be applied to on-chip droplet sequencing is LAMP, or loop-mediated isothermal amplification. On contrast with PCR, LAMP uses 2 or 3 sets of primers that 'self-displace' each other while producing copies of the template. This means that, while PCR requires thermal cycling to amplify the underlying DNA template, LAMP may be conducted at a uniform or 'isothermal' temperature. This is advantageous for this platform due to potential to generate an amplification signal to the droplet merely by providing the LAMP reagents to the aqueous phase and holding the chip at the optimal amplification temperature.

The dual advantages of increased sensitivity to limited analyte and sequencing-based insight into the genetic basis of a sample's resistance phenotype can only be unlocked by combining the microcapillary device developed in chapter 2 with the droplet generator developed in chapter 3 and incorporating droplet-sorting mechanisms downstream from the PMT. Trivially, this could be accomplished by placing the droplet chip inline, downstream from the mixing element on the microcapillary device, such that the homogeneous solution is broken down into discrete droplets which contain cells according to the Poissonian distribution. The droplets will confine the lysed and purinergically released ATP to droplets of about 8.4nL and therefore produce a much higher

concentration and clearer signal than would be achievable in the continuous phase system. At this stage in development, LAMP may begin to be introduced to the system design. LAMP can be most easily incorporated by introducing the primers and polymerase into the aqueous phase along with the L/L reporter mixture. LAMP has been shown to successfully amplify DNA in sorted fluidic droplets[58]. These advancements would provide not only proportions of resistance on a cell-counting basis, but also potentially insights into the genetic basis for the observed resistance phenotype.

Returning this type of data quickly enough to perform the test during a patient examination would eliminate the need for the escalation strategy and would truly convert the standard of care to a screen-based narrow spectrum prescription that would not force physicians to hedge bets at the cost of aggravating selective pressure.

5.2 Molecular Analysis of Long-Term Perfused Cardiac Organoids

In collaboration with the Aguirre lab, I developed a closed-circuit media pump which perfuses heart organoids under positive pressure and keeps them submerged in media to maintain their health over long experiments. However, the goal of the experiment is the identify the effects of positive pressure-induced stretch on the further development and maturation of the heart organoids. The metrics that will be used to measure the maturity of the organoid are partitioned internal chambers, organized capillary beds, and expression patterns more like adult myocardium.

Next steps include utilizing the current circuit to perfuse the organoids for 7 days. The organoids will then be retrieved and evaluated on both our metrics (anatomical and molecular). Anatomical evaluation will include brightfield microscopy to check for changes in over diameter and the presence on internal chamber development. Immunohistochemistry may be used to check for the alignment of capillaries. Finally, an RNA-Seq panel may be run on an Illumina platform.

Genes specifically involved in myocardium lineage, mechanoreception, and blood vessel development will be incorporated into a heatmap. Pre- and post-perfusion organoids will then be compared to available expression patterns from adult myocardium.

It is hypothesized that the stretch factor from the pump will organize the vessels into native capillary beds, and that the internal pressure will stimulate an increase in the diameter of the organoid and formation of more mature cardiac muscle. If that anatomical and expression data supports this hypothesis, the next step may be mechanistic investigations.

BIBLIOGRAPHY

1. Terry, S., Jerman, H. & Angell, J. A Gas Chromatograph Air Analyzer Fabricated on a Silicon Wafer. *Electron Devices, IEEE Transactions on* **26**, 1880–1886 (1980).

2. Manz, A., Graber, N. & Widmer, H. M. Miniaturized total chemical analysis systems: A novel concept for chemical sensing. *Sens Actuators B Chem* **1**, 244–248 (1990).

3. Xia, Y. & Whitesides, G. M. Soft Lithography. *Angew Chem Int Ed Engl* **37**, 550–575 (1998).

4. Rao, H.-X., Liu, F.-N. & Zhang, Z.-Y. Preparation and oxygen/nitrogen permeability of PDMS crosslinked membrane and PDMS/tetraethoxysilicone hybrid membrane. *J Memb Sci* **303**, 132–139 (2007).

5. Nishat, S., Jafry, A. T., Martinez, A. W. & Awan, F. R. Paper-based microfluidics: Simplified fabrication and assay methods. *Sens Actuators B Chem* **336**, 129681 (2021).

6. Yadhuraj, S. R., Gandla, S. B., Omprakash, S. S., Sudarshan, B. G. & Kumar, S. C. P. Design and Development of Micro-channel using PDMS for Biomedical Applications. *MATERIALS TODAY-PROCEEDINGS* vol. 5 21392–21397 Preprint at https://doi.org/10.1016/j.matpr.2018.06.545 (2018).

7. Shim, J. *et al.* Ultrarapid Generation of Femtoliter Microfluidic Droplets for Single-Molecule-Counting Immunoassays. *ACS Nano* **7**, 5955–5964 (2013).

8. Miralles, V., Huerre, A., Malloggi, F. & Jullien, M.-C. A Review of Heating and Temperature Control in Microfluidic Systems: Techniques and Applications. *Diagnostics (Basel)* **3**, 33–67 (2013).

9. Zilionis, R. *et al.* Single-cell barcoding and sequencing using droplet microfluidics. *Nat Protoc* **12**, 44–73 (2017).

10. Liu, Y. & Lu, H. Microfluidics in systems biology-hype or truly useful? *Curr Opin Biotechnol* **39**, 215–220 (2016).

11. Ariati, R., Sales, F., Souza, A., Lima, R. A. & Ribeiro, J. Polydimethylsiloxane Composites Characterization and Its Applications: A Review. *Polymers (Basel)* **13**, (2021).

12. Shim, S., Belanger, M. C., Harris, A. R., Munson, J. M. & Pompano, R. R. Two-way communication between ex vivo tissues on a microfluidic chip: application to tumor-lymph node interaction. *Lab Chip* **19**, 1013–1026 (2019).

13. Bennett, P. M. Plasmid encoded antibiotic resistance: acquisition and transfer of antibiotic resistance genes in bacteria. *Br J Pharmacol* **153**, S347–S357 (2008).

14. Roca, I. *et al.* The global threat of antimicrobial resistance: science for intervention. *New Microbes New Infect* **6**, 22–29 (2015).

15. Martínez, M. L., Plata-Menchaca, E. P., Carlos Ruiz-Rodriguez, J. & Ferrer, R. An approach to antibiotic treatment in patients with sepsis. *J Thorac Dis* **12**, 1007–1021 (3AD).

16. Augustine, S. & Bonomo, R. A. Taking stock of infections and antibiotic resistance in the elderly and long-term care facilities: A survey of existing and upcoming challenges. *Eur J Microbiol Immunol (Bp)* **1**, 190–197 (2011).

17. Roope, L. S. J. *et al.* The challenge of antimicrobial resistance: What economics can contribute. *Science (1979)* **364**, eaau4679 (2019).

18. Hassan, M., Tuckman, H., Patrick, R., Kountz, D. & Kohn, J. Hospital Length of Stay and Probability of Acquiring Infection. *Int J Pharm Healthc Mark* **4**, 324–338 (2010).

19. Cristina, M. L., Spagnolo, A. M., Giribone, L., Demartini, A. & Sartini, M. Epidemiology and Prevention of Healthcare-Associated Infections in Geriatric Patients: A Narrative Review. *Int J Environ Res Public Health* **18**, (2021).

20. van Staa, T. P. *et al.* The Safety of Delayed Versus Immediate Antibiotic Prescribing for Upper Respiratory Tract Infections. *Clin Infect Dis* **73**, e394–e401 (2021).

21. Remick, D. G. Pathophysiology of sepsis. *Am J Pathol* **170**, 1435–1444 (2007).

22. Rüddel, H. *et al.* Adverse effects of delayed antimicrobial treatment and surgical source control in adults with sepsis: results of a planned secondary analysis of a cluster-randomized controlled trial. *Crit Care* **26**, 51 (2022).

23. Revelas, A. Healthcare - associated infections: A public health problem. *Niger Med J* **53**, 59–64 (2012).

24. Newman-Toker, D. E. *et al.* Rate of diagnostic errors and serious misdiagnosis-related harms for major vascular events, infections, and cancers: toward a national incidence estimate using the “Big Three”. **8**, 67–84 (2021).

25. Moraes, R. B., Guillén, J. A. V., Zabaleta, W. J. C. & Borges, F. K. De-escalation, adequacy of antibiotic therapy and culture positivity in septic patients: an observational study TT - Descalonamento, adequação antimicrobiana e positividade de culturas em pacientes sépticos: estudo observacional. *Rev Bras Ter Intensiva* **28**, 315–322 (2016).

26. Levy, M. M., Evans, L. E. & Rhodes, A. The Surviving Sepsis Campaign Bundle: 2018 Update. *Crit Care Med* **46**, (2018).

27. Hudzicki, J. Kirby-Bauer disk diffusion susceptibility test protocol. *American society for microbiology* **15**, 55–63 (2009).

28. Mempin, R. *et al.* Release of extracellular ATP by bacteria during growth. *BMC Microbiol* **13**, 301 (2013).

29. Verkhratsky, A. Early evolutionary history (from bacteria to hemichordata) of the

omnipresent purinergic signalling: A tribute to Geoff Burnstock inquisitive mind. *Biochem Pharmacol* **187**, 114261 (2021).

30. Verkhratsky, A. & Burnstock, G. Biology of purinergic signalling: Its ancient evolutionary roots, its omnipresence and its multiple functional significance. *BioEssays* **36**, 697–705 (2014).

31. Heller, A. A. & Spence, D. M. A rapid method for post-antibiotic bacterial susceptibility testing. *PLoS One* **14**, e0210534–e0210534 (2019).

32. Fetah, K. *et al.* The emergence of 3D bioprinting in organ-on-chip systems. *Progress in Biomedical Engineering* **1**, 12001 (2019).

33. Fong, D. H. & Berghuis, A. M. Substrate promiscuity of an aminoglycoside antibiotic resistance enzyme via target mimicry. *EMBO J* **21**, 2323–2331 (2002).

34. Hooper, D. C. Emerging mechanisms of fluoroquinolone resistance. *Emerg Infect Dis* **7**, 337–341 (2001).

35. Lee, H., Lolicato, M., Arrigoni, C. & Minor, D. L. Chapter Eight - Production of K2P2.1 (TREK-1) for structural studies. in *Ion Channels: Channel Production and Optical Methods* (eds. Minor, D. L. & Colecraft, H. M. B. T.-M. in E.) vol. 653 151–188 (Academic Press, 2021).

36. Fish, D. N. & Chow, A. T. The clinical pharmacokinetics of levofloxacin. *Clin Pharmacokinet* **32**, 101–119 (1997).

37. Zaunbrecher, M. A., Sikes, R. D., Metchock, B., Shinnick, T. M. & Posey, J. E. Overexpression of the chromosomally encoded aminoglycoside acetyltransferase eis confers kanamycin resistance in Mycobacterium tuberculosis. *Proc Natl Acad Sci U S A* **106**, 20004–20009 (2009).

38. Kubitschek, H. E. Cell volume increase in Escherichia coli after shifts to richer media. *J Bacteriol* **172**, 94–101 (1990).

39. Pinger, C. W., Heller, A. A. & Spence, D. M. A Printed Equilibrium Dialysis Device with Integrated Membranes for Improved Binding Affinity Measurements. *Anal Chem* **89**, 7302–7306 (2017).

40. Lim, J. *et al.* Ultra-high throughput detection of single cell β-galactosidase activity in droplets using micro-optical lens array. *Appl Phys Lett* **103**, 203704 (2013).

41. Sahin, S., Bliznyuk, O., Rovalino Cordova, A. & Schroën, K. Microfluidic EDGE emulsification: the importance of interface interactions on droplet formation and pressure stability. *Sci Rep* **6**, 26407 (2016).

42. Nelson, W. C. & Kim, C.-J. 'CJ'. Droplet Actuation by Electrowetting-on-Dielectric (EWOD): A Review. *J Adhes Sci Technol* **26**, 1747–1771 (2012).

43. Bremond, N. & Bibette, J. Exploring emulsion science with microfluidics. *Soft Matter* **8**,

10549–10559 (2012).

44. Laborie, B., Rouyer, F., Angelescu, D. E. & Lorenceau, E. Yield-stress fluids foams: flow patterns and controlled production in T-junction and flow-focusing devices. *Soft Matter* **12**, 9355–9363 (2016).

45. Utada, A. S., Fernandez-Nieves, A., Stone, H. A. & Weitz, D. A. Dripping to Jetting Transitions in Coflowing Liquid Streams. *Phys. Rev. Lett.* **99**, 94502 (2007).

46. de Souza, N. Organoids. *Nat Methods* **15**, 23 (2018).

47. Nijak, A. *et al.* Morpho-functional comparison of differentiation protocols to create iPSC-derived cardiomyocytes. *Biol Open* **11**, bio059016 (2022).

48. Lewis-Israeli, Y. R. *et al.* Self-assembling human heart organoids for the modeling of cardiac development and congenital heart disease. *Nat Commun* **12**, 5142 (2021).

49. Lammert, E. *et al.* Role of VEGF-A in Vascularization of Pancreatic Islets. *Current Biology* **13**, 1070–1074 (2003).

50. E. Johnson, B., B. Goodman, M., Brown, A. L., Johnson, B. E. & Goodman, M. B. Making Patch-pipettes and Sharp Electrodes with a Programmable Puller. *JoVE* e939 (2008) doi:doi:10.3791/939.

51. Daneman, D. Type 1 diabetes. *The Lancet* **367**, 847–858 (2006).

52. Weir, G. C. & Bonner-Weir, S. Islets of Langerhans: the puzzle of intraislet interactions and their relevance to diabetes. *J Clin Invest* **85**, 983–987 (1990).

53. Pinger, C. W., Entwistle, K. E., Bell, T. M., Liu, Y. & Spence, D. M. C-Peptide replacement therapy in type 1 diabetes: are we in the trough of disillusionment? *Mol Biosyst* **13**, 1432–1437 (2017).

54. Dima, S. *et al.* [Human pancreas procurement for pancreas and islet transplantation]. *Chirurgia (Bucur)* **102**, 19–26 (2007).

55. Axpe, E. & Oyen, M. L. Applications of Alginate-Based Bioinks in 3D Bioprinting. *International Journal of Molecular Sciences* vol. 17 Preprint at https://doi.org/10.3390/ijms17121976 (2016).

56. Yue, K. *et al.* Synthesis, properties, and biomedical applications of gelatin methacryloyl (GelMA) hydrogels. *Biomaterials* **73**, 254–271 (2015).

57. Kuwabara, R. *et al.* Applying Immunomodulation to Promote Longevity of Immunoisolated Pancreatic Islet Grafts. *Tissue Eng Part B Rev* **28**, 129–140 (2021).

58. Chung, M. T., Kurabayashi, K. & Cai, D. Single-cell RT-LAMP mRNA detection by integrated droplet sorting and merging. *Lab Chip* **19**, 2425–2434 (2019).